BERGISCHE
UNIVERSITÄT
WUPPERTAL

Development of an H_3^+ Driven Chemical Ionization Source for GC-MS

Dissertation

zur Erlangung des akademischen Grades
Doktor der Naturwissenschaften (Dr. rer. nat.)

vorgelegt von
Kai Sven Kroll
geboren in Leverkusen, Deutschland

Bergische Universität Wuppertal
Fakultät für Mathematik und Naturwissenschaften
Physikalische und Theoretische Chemie
Unter der Leitung von Prof. Dr. Thorsten Benter

Wuppertal, Oktober 2021

The PhD thesis can be quoted as follows:

urn:nbn:de:hbz:468-urn:nbn:de:hbz:468-20211115-121441-4
[http://nbn-resolving.de/urn/resolver.pl?urn=urn%3Anbn%3Ade%3Ahbz%3A468-20211115-121441-4

DOI: 10.25926/tb7w-zf55
[https://doi.org/10.25926/tb7w-zf55]

Danksagung

Es gibt viele Menschen, die mich während der Arbeit an dieser Dissertation in vielfältiger Art und Weise unterstützt und ermutigt haben. Jeder von euch kennt seinen Anteil, egal wie groß oder klein dieser war. All jenen möchte ich hiermit meinen tiefsten Dank aussprechen.

Abstract

In this work a novel plasma based chemical ionization (CI) source and its hyphenation with gas chromatography (GC) using a time-of-flight mass spectrometer (TOF MS) is developed. Classical electron beam driven chemical ionization sources often suffer from reduced filament lifetimes and thus require high maintenance efforts. Problems occur especially when using reactive and/or oxidizing reagent gases as well as due to reagent gas degradation product accumulation inside the ion source assembly.

The alternative CI method developed in this work is based on the application of H_3^+ as primary charge-carrying species and its subsequent conversion via selective reaction cascades using reagent gases which then lead to ionization of the compound of interest. The H_3^+ ion is produced with high efficiency in a hydrogen plasma driven with a helical resonator. Since the proton affinity of H_2 is much lower than that of almost all atoms and molecules, H_3^+ acts as a universal proton donor via a proton transfer reactions. The respective reagent ion formation of the three reagent gases nitrogen, methane, and isobutane were studied. In contrast to classical CI source operation, the formation of reagent ions and thus analyte ionization occurred mainly via proton transfer reactions. The quantitative transformation of H_3^+ into various reagent ion species allows to adjust the exothermicity of the analyte protonation reaction, minimizing the extent of fragmentation. The selectivity and sensitivity of the developed CI method is evaluated for various compounds.

The ion source development process is discussed in detail. Four iteratively developed ion source designs were investigated. The performance of each ion source setup is carefully assessed. The final chemical ionization source design exhibits low picogram- to upper femtogram-on-column sensitivity and chromatographic peaks of Gaussian shape with full width at half maximum (FWHM) of < 1 s even for high boiling compounds of a fatty acid methyl ester (FAME) mixture. The customized helical resonator plasma source provides excellent long-term stability and requires low maintenance, while consisting of simple and low-cost hardware.

Contents

1. Introduction

1.1 Chemical Ionization Mass Spectrometry

1.1.1 Historical Background

Chemical ionization mass spectrometry (CIMS) describes a wide range of gas-phase ion-molecule reactions applied for the analysis of diverse gas mixtures. Such reactions were initially observed but not necessarily recognized as such, early in the development of mass spectrometry. At that time collisions between the generated ions in a large excess of neutral molecules could not be avoided as sufficiently low pressures were difficult to maintain.
Products of such ion-molecule reactions were already described in the literature early in the history of mass spectrometry. Thomson discovered the ionic specie H_3^+ in 1911 [1] but first referred to the signal at *m/z* 3 as "X_3" in his early works [2, 3]. It was Dempster who showed in 1916 that the ratio between H^+, H_2^+ and H_3^+ could be changed depending on the system pressure [4]. In particular, at high H_2 pressure, the H_3^+ signal was stronger than the other peaks, which can be regarded as the first direct evidence that H_3^+ is formed via gas-phase reaction by ionization of molecular hydrogen. However, Dempster did not identify the formation process and it was not until the work by Hogness and Lunn that the famous exothermic ion-molecular reaction was formulated: [5]

$$H_2^{+\cdot} + H_2 \rightarrow H_3^+ + H^\cdot \qquad \text{(R 1)}$$

With improvements in instrumentation and techniques, particularly vacuum technology, the interference of secondary ion-molecule processes were largely eliminated, and studies of ion-molecule reactions almost ceased. The main interests in mass spectrometry during the period 1930 to 1950 was focused on the physics of ionization and dissociation, on the determination of isotopic masses and abundances, and in the development of analytical mass spectrometry using primarily electron ionization (EI) [6]. Pressures in these instruments efficiently suppressed molecular collision and the experimental conditions were generally standardized to eliminate ion-molecule reactions as these rendered quantitative analyses and the determination of isotopic abundances difficult.

The studies of gas-phase ion-molecule reactions that led to the development of chemical ionization mass spectrometry began in the early 1950s with the work of Tal'roze [7] followed very shortly by the work of Stevenson and Schissler [8], and Field *et al*. [9].
These authors observed the formation of the CH_5^+ ion in methane as a stable species, and that its formation was much faster than reactions involving only neutral species. The determined rate coefficient correspond to reactions that occur essentially upon every collision, which stimulated much interest. Subsequently, a high-pressure mass spectrometer was developed that operated at source pressures of a few mbar to further investigate these reactions. It was observed that neither CH_5^+ nor $C_2H_5^+$ react with methane at elevated pressure [10]. This non-reactive system enabled the study of ion-molecule reactions for the first time by adding small amounts of other compounds. This concept was further improved by Munson and Field in the mid-1960s and matured to an analytically useful technique [11–14].
Since the introduction of this technique, the basic concept of chemical ionization (CI) has been expanded and applied in many different fields. One obvious application was the hyphenation with chromatographic techniques. Although in principle it should be possible to selectively ionize the component of interest in a matrix by choice of a suitable Cl reaction without any chromatography, this approach has been relatively rarely used. Instead, temporal separation of multiple compounds by chromatographic methods allow selective ionization from complex mixtures and was rapidly incorporated into commercial instruments, e.g. gas chromatography/chemical ionization mass spectrometry (GC/CIMS) [15, 16].
CIMS represents the development of a useful analytical technique from observations of ion-molecule reactions involving impurities and their effects on the detection of compounds of interest [14]. It was further developed over the years and nowadays it has found extensive applications in structural elucidation and quantitative analytical studies in many branches of chemistry, biochemistry, as well as in medical and environmental areas [14, 17].

1.1.2 Chemical Ionization Mechanisms

Chemical ionization, as the name implies, utilizes chemical reactions to achieve ionization of analyte molecules in the gas phase. The neutral analyte molecules interact with ions generated from a reagent gas in ion-molecule reactions. Any ion-molecule reaction charging the analyte is essentially contributing to CIMS mechanisms. This may involve the transfer of an electron, proton and/or other charged species [18]. Since these reactions are naturally bimolecular processes, a sufficiently large number of ion-molecule collisions are required. Such conditions are found in many other mass spectrometric ionization techniques were collisions and thus the

source pressure is sufficiently high, e.g., in fast atom bombardment (FAB), electrospray ionization (ESI), matrix-assisted laser desorption ionization (MALDI), atmospheric pressure chemical ionization (APCI), or dopant assisted atmospheric pressure photoionization (DA-APPI). It is pointed out though that the pivotal role of ion-molecule reactions in these techniques is often not well understood or even recognized [14].

In classical CI, the ion source design is heavily building on EI ion sources. The majority of chemical ionization studies have been carried out using source designs, which are only slightly modified from those used in electron ionization studies. Most current vacuum ion sources can operate in either the electron or chemical ionization mode [18].

Several CI reagent gases for diverse applications have been studied [19]. The most common reagent gases include methane, isobutane and ammonia. The gas is introduced into the ionization volume in a 10^3-10^4 fold excess to the analyte at a local source pressure of about 1 mbar. The CI reagent ions are formed via electron ionization of the reagent gas with electron energies up to 400 eV, followed by ion-molecule reactions of the primarily formed ions and further reagent gas neutrals [6]. These ions subsequently react with analyte molecules to form both positive and negative ions simultaneously. Among the wide range of possible reactions, the main pathways occurring in positive-ion-mode chemical ionization (PICI) are as follows:

$M + [BH]^+ \rightarrow [M+H]^+ + B$	*proton transfer*	(R 2)
$M + X^+ + M \rightarrow [M+X]^+ + M$	*electrophilic addition*	(R 3)
$M + X^+ \rightarrow [M-A]^+ + AX$	*anion abstraction*	(R 4)
$M + X^{+\cdot} \rightarrow M^{+\cdot} + X$	*charge exchange*	(R 5)

Reactions 2 - 4 result in even electron ions, whereas charge exchange (R 5) yields radical ions. Reactions between negative ions or electrons and neutral molecules have not been the objective of this study and will be thus not further discussed. For further reading cf. reference [6].

The most common ionization reaction in (positive mode) CI is *proton transfer* (R 2). The reagent gas ions $[BH]^+$ transfer a proton to the analyte molecules M and form protonated molecule analyte ions $[M+H]^+$. In this case, the reagent gas ions $[BH]^+$ act as a Brønsted acid (proton donor) and the analyte molecules M as a Brønsted base (proton acceptor). This reaction follows the usual rules of acid-base reactions: the stronger base accepts the proton from the conjugate acid of the weaker base. The tendency of a molecule to accept a proton is quantified by its proton affinity (PA), which is by definition the negative enthalpy change of the

(often hypothetical) gas-phase protonation reaction:

$$B + H^+ \rightarrow [BH]^+ \qquad -\Delta H^0 = PA_{(B)} \qquad \text{(R 6)}$$

In the case of an intended protonation, one has to compare the PAs of the neutral analyte molecule M with that of the conjugated base B of the proton-donating reagent gas ion $[BH]^+$. When this reaction is exothermic, i.e., when $PA_{(B)} < PA_{(M)}$, and the difference in proton affinity is such that the reaction is exergonic, the protonation reaction proceeds mostly collisionally controlled. The reaction enthalpy needs to be distributed among the degrees of freedom of the analyte ion $[M+H]^+$. The energy dissipation rate depends also on the local temperature and pressure, i.e., the extent of thermalizing collisions. In general, the more exothermic the protonation reaction, the higher the extent of fragmentation of the analyte ion $[M+H]^+$ will be. The thermochemistry of the proton transfer reaction can thus be controlled by using different reagent gases.

In the *electrophilic addition* step (R 3), i.e., association or clustering reactions, the collision of an ion X^+ with a neutral molecule M results in the formation of a complex $[M+X]^+$, after collisional stabilization. Basically, every formed ion, e.g., molecular ions, protonated molecules, or fragment ions may "cluster" with analyte molecules, reagent gas molecules, and/or fragments. The generated adduct ions are often useful to identify the analyte's molecular mass. For example, in the case of ammonia as reagent gas, an electrophilic addition mainly occurs by attachment of protonated reagent ions to the analyte molecule, yielding $[M+NH_4]^+$ ions.

A representative of *anion abstraction* reactions (R 4) is the hydride abstraction. As an example, this reaction leads to the *t*-$C_4H_9^+$ ion as the main ionic species when using i-butane as reagent gas. Similarly to the proton transfer reaction, thermochemical effects play a significant role. The hydride abstraction may become dominant, when the hydride ion affinity (HIA) of X^+ is greater than the HIA of $[M-A]^+$. The HIA of a gaseous cation X^+ is defined as the negative enthalpy change for the hydride transfer reaction:

$$X^+ + H^- \rightarrow XH \qquad -\Delta H^0 = HIA_{(X^+)} \qquad \text{(R 7)}$$

Charge exchange or *charge transfer* (R 5) occurs, when the ionic charge of an ion $X^{+\cdot}$ is transferred to the neutral molecule M, forming the radical cation $M^{+\cdot}$. The same rational as for proton transfer or hydride abstraction, applies to charge exchange reactions: When the reaction is exothermic, it is likely to be fast; when it is endothermic, it is likely to be slow. The thermochemistry of charge exchange reactions is determined by the ionization energy (IE) of

the neutral molecule M and the recombination energy (RE) of the reagent ion $X^{+\cdot}$. The recombination energy is defined as the negative enthalpy change of the gas-phase reaction:

$$X^{+\cdot} + e^- \rightarrow X \qquad -\Delta H_r = \mathrm{RE}_{(X^{+\cdot})} \qquad \text{(R 8)}$$

For a monoatomic ion, the RE has the same value as the IE of the neutral counterpart, since this process is the inverse of its ionization. This is not necessarily the case for diatomic or polyatomic ions. The neutral molecule may have excess energy stored in internal degrees of freedom (vibrational/rotational) or may be formed in an excited electronic state. However, if the IE of the reagent gas is greater than the ionization energy of the analyte molecule, then the charge transfer reaction may occur. For polyatomic molecules, the exothermicity of the reaction is mainly dissipated in the internal degrees of freedom of the product ions. If this internal energy is sufficiently large and not dissipated, e.g. by collisions, the ion may undergo fragmentation.

1.2 Plasmas

There are diverse methods of igniting and sustaining a controlled plasma discharge. In this work, a helical resonator was used to generate a controlled hydrogen plasma. This plasma resembles a resonant RF-driven inductively coupled plasma (ICP).

In the following chapters, the fundamentals of plasma physics, especially addressing low-pressure RF plasmas, are briefly discussed.

A plasma is a conglomerate of neutrals, electronically excited species, and charged particles moving in random directions. Overall, a plasma is electrically neutral. Plasmas are often referred to as the fourth state of matter.

The fundamental rule of sustaining a plasma discharge is that an electron must recreate itself before being lost. Therefore, the electron must have a collision with a neutral atom, molecule, or ion that results in ionization. The simplest model of igniting a plasma is an electron accelerated by an electrical field. After ignition, the sustained plasma state is characterized by equal densities of electrons and ions, $n_e \approx n_i \approx n$ particles m^{-3} and an equal electron and ion temperature $T_e = T_i = T$ [20].

Low-pressure discharges (10^{-3} mbar – 1 mbar) are rarely in a state of thermal equilibrium. The applied electrical power is mainly affecting the motion of free electrons. Consequently, the temperatures of electrons and ions are decoupled from each other. In the core region of the plasma ("plasma bulk") energy is very inefficiently transferred from the light electrons to the heavy ions as well as neutral particles by "weak" collision processes. In addition to the large

mass difference, which determines the energy transfer efficiency, the dwell time of plasma species in low-pressure gas discharges is often not sufficient to establish equilibrium. Hence, $T_i \ll T_e$ holds true for these plasmas. Typically, low-pressure discharges are characterized by electron temperatures of T_e = 1 – 10 V and electron densities of $n \approx 10^8$ - 10^{13} cm^{-3}. Ions and neutral particles have roughly the same temperature (≈ 0.026 eV) [20].

As mentioned before, sustaining the plasma state electrons must recreate themselves before being lost. For low-pressure discharges, the maximum electron energy is generally below the ionization threshold of neutrals. Nevertheless, dissociation and ionization occur because electrons have a certain energy distribution, e.g. Maxwellian. Hence, the dissociation and ionization of the bulk gas occurs only by the high-energy tail of the distribution. The Maxwellian energy distribution of the electrons can be moved in either direction by electron heating or electron–neutral collision processes.

Lowering the gas pressure leads to a higher mean free path of the electrons resulting in higher kinetic energy and reduced collision numbers with the bulk gas. At higher gas pressures the mean free path decreases and the collision number increases. As a result, the plasma becomes collision-dominated and the electron temperature decreases.

As in all physical systems, the conservation of energy rigidly applies to the description of plasmas. The energy absorbed by the plasma must correspond to the dissipative losses. These losses are mainly caused by collisions between electrons and neutral gas particles, which lead to ionization. However, the loss due to diffusion of charge carriers to wall surfaces is also of importance to the overall energy balance. Plasmas are connected to wall surfaces via thin positively charged layers, so-called *sheaths* [21].

Consider a plasma initially confined between two grounded surfaces. Because the plasma is electrically neutral, the net charge density and thus the electric potential and the electric field are zero everywhere between the boundary surfaces. Since the thermal velocity of an electron is at least 100 times the ion thermal velocity, electrons will be lost on the surfaces. This leads to the formation of “thin” positive ion sheaths near each grounded surface. The net positive charge density within the sheaths leads to a potential profile that is positive within the plasma and falls sharply to zero near both surfaces. Thus, electrons traveling towards the surface are reflected back into the plasma and ions from the plasma that enter the sheaths are accelerated to the surface. This charge separation between bulk plasma and sheath regions is an important model that applies to all discharges. The bulk region is quasi field free. The bulk plasma dynamics is described by diffusive ion loss at high pressures and by free-fall ion loss at low pressures. In the positive space charge sheaths, high field gradients exist, leading to a dynamics that can be described by various ion space-charge sheath models including low-voltage

sheaths and various high-voltage sheath models, such as collisionless and collisional Child laws and their modifications [20].

The absorbed energy by the plasma is mainly dissipated by collision processes between electrons and neutral gas particles. The two main electron heating mechanisms in low-pressure discharges are stochastic heating and Ohmic heating.

Stochastic electron heating (sometimes called collisionless heating) occurs mainly in the low-pressure range and plays a major role in capacitively coupled plasmas [22]. The electrons gain energy by reflection at the oscillating sheath boundary. During a half-period, when the sheath moves towards the bulk plasma, the electrons gain energy. During the other half of the period, when the sheath moves away from the bulk plasma, the electrons lose energy. Since the electric field gradients in the sheath region are much larger than inside the plasma, there is always a net energy gain for the electrons.

The Ohmic heating describes the energy conversion of directional particle motion (kinetic energy) by collision processes into undirected thermal motion. Therefore, it dominates at higher pressures due to the increased collision frequency between the electrons and the neutral gas particles. This type of heating takes place in all gas discharges and plays an important role in inductively coupled plasmas [20].

In the following RF-discharges are discussed in more detail and in particular inductively coupled plasmas (ICPs).

As the name suggests, an inductively coupled plasma uses an inductive electric circuit element to couple energy into the discharge. This inductive circuit element is typically a helical or spiral conductor ("coil"). The plasma is generally maintained by time-dependent magnetic fields generated in the primary coil. In the case of the helical conductor, an axial electric field is generated due to the voltage drop across the coil. The axial magnetic fields are induced by the RF current. It follows from the law of induction (Faraday's law) of Maxwell's equations that a magnetic field that changes over time generates a rotating electric field. This additionally generates an azimuthal electric field. Since the inductively coupling element is operated in an electrical resonance state, high potential differences are not present on the coil structure. Based on these considerations, an inductive discharge can be divided into two modes, the E-Mode (electrostatic mode, capacitive coupling) and the H-mode (electromagnetic mode, inductive coupling) [23].

The E-mode is operative at low power dissipation in the plasma. It is characterized by a low electron density, which is about a factor 100 smaller than in the H-mode. The coupling of the RF power is mainly achieved by the voltage drop between coil and plasma. Since the coupling

is similar to capacitive coupling, higher electron temperatures are expected in E-mode as compared to H-mode.
Because the conductivity of the plasma is small, the discharge is transparent for the H-field, and the alternating magnetic field of the inductor cannot transfer energy to the discharge. However, as soon as the plasma conductivity is increased by the E-field reaching a critical value, the magnetic energy of the inductor begins to be transferred into the plasma. The circuit layout cause the voltage across the coil to drop as the plasma begins to absorb power. When more power is coupled into the system, the discharge may switch from E-mode (capacitive mode) to an H-mode (inductive mode). This is called a mode transition. The exact transition point is not precisely predictable, as it depends on numerous factors such as the discharge gas, the coil geometry, the distance between plasma and coil and the current through the coil.
In the H-mode, the coupled power is in accordance with Faraday's law of induction. The efficiency of the coupling depends on the quality Q of the RF circuit. In the H-mode, the electron temperature is usually lower than in the E-mode due to the elevated collision rate.
Achieving a pure E- or H-mode is nearly impossible, since capacitive effects always occur in an inductive discharge. Inductively coupled plasmas usually ignite in the capacitive E-mode and when the coil current is high enough, the discharge changes to an inductive H-mode.
In low-frequency plasmas (MHz range), the RF fields do not propagate through the plasma as they do, e.g., in a microwave plasma (GHz range), and in addition the penetrating fields are limited to the surface. This is usually referred to as the *skin effect*. In this case, the plasma is subject to the properties of an RF conductor. The skin depth indicates the ability of a material to conduct the current in a given layer. At high frequencies, the current is conducted in thinner layers on the surface of the conducting medium. At lower frequencies, the conducting layer becomes wider until it penetrates the entire medium. The induction of RF currents into the plasma always occur within a skin layer. Accordingly, the coupled power will change depending on the frequency and/or skin depth.

1.2.1 Helical Resonator Plasmas

Without the presence of a plasma, the geometry of the helical resonator is the same as that of a conventional filter resonator acting as passive electrical component. The design of helical resonators was motivated by the growing demand for high Q tuning elements in electronic circuits for the frequency range below the GHz regime, where cavity resonators become unfavorable [24]. Due to their simplicity, helical resonators have found many applications, e.g.,

in atomic frequency standards [25], in precision measurements of dielectric properties [26], or in plasma physics [27–29].

The first adaptation to generating a plasma dates back to 1969, as a source for polarized protons and deuterons in an atomic beam method [30], followed by further molecular and atomic beam source experiments [27, 31, 32]. The demand for novel plasma sources with high plasma densities in the semiconductor industry for etching, sputtering, and deposition processes pushed plasma research in the 1990s [33, 34].

The helical resonator plasma can be classified as member of inductively coupled plasmas [20]. The design has several advantages: It provides a relatively high-density plasma ($1 \cdot 10^{10}$ - $1 \cdot 10^{12}$ cm^{-3}) at relatively low RF input power (10-40 W) while exhibiting high Q (600-1500, without the plasma present), operates at radio frequencies (3-30 MHz), builds on simple inexpensive hardware, is operated without an external matching network, and operates at pressures as low as 10^{-4} mbar [28, 33, 35–37].

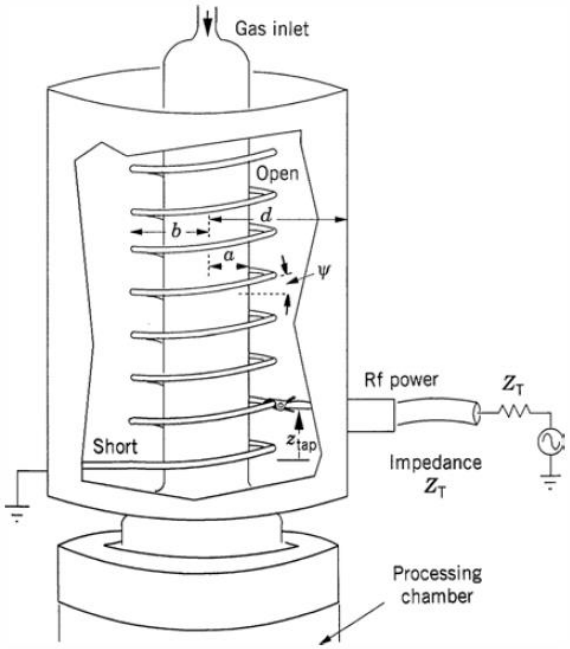

Figure 1: Schematic of a helical resonator plasma source. Reprint from Liebermann M. A. (2005) Principles of Plasma Discharges and Materials Processing, 2nd Edition, with permission from Wiley.

Figure 1 is a schematic of a helical resonator plasma source. It consists of a cylindrical discharge tube within a helical coil of prescribed diameter, pitch and length, which is surrounded by a coaxial grounded cylinder. One terminal of the helical coil is connected directly to the shield and the other is floating. When the coil is designed with an electrical length of $(1 + 2k)\,\lambda/4$,

where λ is the wavelength of the excitation frequency and k is an integer, then the structure becomes a resonant cavity. Basically, it resembles a coaxial quarter-wave resonator, except that the inner conductor has the shape of a helix.
Since the helical coil is operated resonantly, a coupling to the low- and high-voltage ends of the cylindrical coil occurs, which is much more difficult to achieve in a purely inductive regime. Capacitively coupled discharges in inductively coupled plasma sources are frequently observed. It is reported that these discharges are often capacitively driven at low plasma densities (E-Mode), with a transition to an inductive mode of operation at high densities (H-Mode) [38, 39].
To force the operation in the inductive mode, the capacitive mode can be suppressed by placing a conducting material between the plasma column and the coil [39, 40]. This technique was used in helical resonators by adding a metal cylinder positioned along the main coil axis, which allows the inductive field to penetrate into the plasma while shorting out the capacitive electrical fields to reduce the capacitive coupling to a negligible value [41].

However, in the unshielded helical resonator plasma, both modes exist. It can operate either in a capacitive mode where the axial electrical field (E_z) is dominant (E-mode) or in an inductive mode where the azimuthal electrical field (E_θ) is dominant (H-mode). An operation in the capacitive mode is characterized by the discharge extending outside the cavity, possibly to some grounded part. In the inductive mode, the discharge is confined to the cavity volume and has an annular profile across the tube diameter [42].
Measurements of the resonance characteristics over a wide range of frequencies in a pressure range from 0.05 to 10 Torr were investigated by Bletzinger *et al.* [29]. It was shown that a wide range of conditions exist where the operating mode for a particular pressure and RF power level can be selected by changing the frequency. Experimental evidence suggests that an operation in the inductive mode can be achieved by reducing the number of wire turns of the helical coil, in analogy to the enhancement of the inductive mode in an inductive discharge. As the number of turns is increased, the voltage V_{max} at the high-voltage end of the coil is increased and results in large sheath fields. The discharge is then operating mainly in the capacitive mode. Further, the authors found that the inductive mode is enhanced at higher power levels and higher pressures, and that the capacitive resonance frequencies were gas-dependent. When using nitrogen instead of argon, the capacitive resonances are shifted to higher frequencies, whereas the inductive resonance frequencies remain unchanged.

A theoretical model of the unshielded helical resonator plasma was presented by *Lieberman et al.* [35], which was experimentally and theoretically further elaborated [28, 37, 43]. The model allows predictions to understand the basic design parameters. It uses the gas pressure, RF power, source length, plasma, helix and outer cylinder radii, winding pitch angle, and excitation frequency as input parameters.

Wave dispersion and the relation of the field quantities have been determined in the approximation of a uniform, collisionless plasma by using a *developed sheath helix model*, in which the RF current in the helical wires is replaced by a continuous current sheet. This slow-wave mode calculation is necessary to determine the resonant frequency, which also involves the finite helix wire diameter, terminal effects, and the effect of the coupling. Once the resonant frequency for quarter wavelength operation is determined, the fields within all regions inside the helical resonator can be calculated [35].

Without a plasma present, there is only one mode of field propagation. As the plasma and the helix are both found to be at elevated potential in reference to the outer shield, this mode is named *coax* mode. The dominant electric field is the E_θ field.

Upon establishing a plasma, a second mode is observed when the driving frequency is much lower than the plasma frequency ($\omega < \omega_p$). As the helix at elevated potential in reference to the shield and the plasma, this mode is called *helix* mode.

As the plasma frequency is typically much larger than the driving frequency, both modes coexist during operation but resonate at different driving frequencies. The *coax* mode is important during startup when the plasma density (n) is zero. At typical discharge operation ($n > 10^9$ cm^{-3}), the helix mode dominates and it is assumed that (i) the mode structure is quasi-static, (ii) the net axial magnetic flux is approximately zero, and (iii) the radial electric fields are small within the plasma because they are shortened out by the conductivity of the plasma column and because the voltage between the plasma and outer shield is approximately zero. This quasi-stationary assumption in the helix mode together with the magnetic flux assumption applied to a cylindrical structure, including plasma collisions, results in a simpler set of fields and was then used to determine the plasma heating [35]. This has been done in the capacitively coupled mode where both Ohmic and stochastic heating contributes to the absorbed power. It was found that the coupling of energy into the plasma is relatively efficient in the helical resonator both at low pressure (through the process of stochastic heating in the sheath) and at high pressure (through Ohmic heating in the bulk plasma). In relation to the external electric driving field E_r, the stochastic sheath heating is similar to the heating in a capacitive RF discharge. The Ohmic heating in the helical resonator is much stronger than in a capacitive discharge, because it is driven by a larger electric field component E_z. In general, the

two energy transfer mechanisms can be combined to determine the overall heating rate in a discharge.

As an example, with a source of dimensions a = 3 cm, b = 5 cm, d = 10 cm, Ψ = 0.1 rad and argon as discharge gas, the pressure regime for which the stochastic heating dominates is found to be $\leq$ 2.3 mTorr. The Ohmic heating mechanism dominates at pressures $\gg$ 4 mTorr [35].

The analysis described above was further improved by including (i) the stochastic heating at the sheath boundary (ii), Ohmic heating in the bulk plasma, (iii) ohmic heating in the sheath region, and (iv) ionization in the sheath. Ain addition to these effects, a comparison has been made between theory and experiment for the two plasma gases argon and nitrogen in the pressure range 2 - 20 mTorr ([28]). Qualitative agreement between the theoretical model and the experimental results was achieved.

These calculations were not carried out for the inductively coupled mode (with an electrostatic shield), where only E_θ contributes to the absorbed power, but should be similar to that used for conventional inductive sources [20].

The matching characteristics of the helical resonator to an external power source are obtained from transmission line calculations and experiments [37, 43]. Consider the RF generator and its transmission line to have a characteristic impedance Z_T, with is one terminal of the transmission line connected to the helical coil at the tap position z_{tap}, and the other terminal is connected to the grounded shield, as depicted in Figure 1. This leads to an inductive input impedance at the open terminal and a capacitive input impedance at the shorted terminal of the coil. This impedance ratio can be adjusted by the position of the power tap and acts as "internal" matching system, allowing a good match over a wide range of parameters. Since the helix impedance, Z_0, is typically large compared to Z_T and because the RF generator can only be matched with the capacitive load, a favorable match occurs preferentially with a tap close to the shorted terminal of the helical resonator, where the voltage is small and the current is large. The operating frequency provides a second degree of freedom. These two controllable parameters remove the need for an external matching network, which is essential in common parallel-plate RF plasma sources [37]. Once the resonator is connected to an external power source, the fields build up until the internal dissipation equals the supplied power. When this condition is satisfied, there are intense electromagnetic fields present within the helix (because of the high Q), that sustain a plasma with negligible matching loss. Regarding the inductive and capacitive resonance modes, the former preferentially operates at higher impedance (i.e., lower number of turns for the tap), and the latter at lower impedance (lower number of turns for the tap) [29].

2. Aim of this Work

The majority of chemical ionization studies and applications have been carried out using modified electron ionization (EI) sources. Most modern ion sources can operate in both modes alternatively, either with electron ionization or with chemical ionization. As described in detail in chapter 1.1.2, in the chemical ionization mode, a reagent gas is introduced into the ionization volume in large excess and at elevated pressure (~1 mbar). The latter is generally achieved by enclosing the ionization volume (often termed closed ion source), i.e. considerably reducing the local pumping speed. While this is the key point enabling chemical ionization, it also inevitably leads to the greatest disadvantage of such CI sources: the also considerably reduced filament lifetime. Problems occur especially with aggressive or oxidizing reagent gases such as NO, N_2O or O_2. These gases react with the hot filament surface and thus shorten its lifetime even further [6].

However, not only severe filament degradation causes problems, also some reagent gases (e.g., isobutane, benzene, or tetramethylsilane) lead to a decrease in the reagent ion intensity over time. This is likely the result of deposition of decomposition products on the insulators and/or electrodes within the ion source assembly and most pronounced in the ionization volume. Frequent maintenance and cleaning of the source assembly lead to considerable downtimes of the instruments [44, 45]. Typical ion source cleaning procedures require a cool down and venting step, disassembly and mechanical cleaning of the source elements, reassembly, evacuation to base pressure, followed by system equilibration under operating conditions.

Another critical parameter is the distributed heat energy by the filament (~ 5 W) leading to elevated temperatures in the ionization volume. This potentially impacts on the signal distribution in the recorded mass spectra, since higher temperatures are often associated with enhanced fragmentation [46]. Some approaches are known to overcome these issues by completely replacing the filament. A Townsend discharge ion source [47] and a glow discharge ion source [46] were reported to replace the electron ionization filament. However, these modifications have not found acceptance as CI methods.

The aim of this work is to (i) tackle the issues stated above by employing an alternative primary ion generation method and (ii) to develop a sensitive, robust, and stable chemical ionization source for applications in the field of GC/CIMS.

One of the most acidic proton donor is H_3^+. Because the proton affinity of H_2 is much lower than that of almost all atoms and molecules (with the notable exception of He, N, and O_2), H_3^+ generally acts as a universal proton donor (Brönsted acid) via proton transfer reactions [48–50]. It thus represents a most favorable initial reagent for driving various selective reaction cascades generating reagent ions which are then leading to ionization of the compound of interest.

The H_3^+ ion can be produced with high efficiency in the reaction of H_2^+ with hydrogen molecules. The use of a hydrogen plasma is a simple and elegant procedure to generate H_3^+, since it is abundantly generated in hydrogen discharges.

As a hydrogen discharge source, a conventional ballast for photoionization lamps is used. It consists of simple, inexpensive hardware, can be operated without an external impedance matching network, provides a high-density plasma at low RF input power and has already demonstrated its robust and stable operation [51].

Since the molar sensitivities in CIMS are mostly proportional to the rate coefficient of the corresponding ion-molecule reactions, the occurrence of bimolecular reactions requires a sufficiently large number of ion-molecule collisions during the dwell time of the reagents in the ion source. Therefore, the developed ion source is operating in a pressure range of about 1 – 10 mbar. The increased pressure can also have a collisional stabilizing effect on the analyte ions [52].

In a first step, a helical resonator is adapted for the intended scope of application and fundamental knowledge about the parameters affecting the primary ion current is gathered to further improve the discharge source.

To optimize various ion source parameters (e.g., geometry parameters, ion kinetic parameters) nitrogen as reagent gas is used in the initial experiments since it forms mainly N_2H^+ in a rather simple reaction cascade. Then, other reagent gas reaction systems and their application to chemical ionization are investigated.

Finally, the hyphenation of the source with a gas chromatograph is another goal of the experimental work of this thesis. GC/CIMS is a common analytical approach for the analysis of complex samples. Crucial parameters concerning the GC peak shapes and thus the chromatographic performance are carefully taken into consideration during the development process.

3. Experimental

3.1 Chemicals

All gases used were purchased from Messer Industriegase GmbH (Bad Soden, Germany). The hydrogen plasma gas and nitrogen as reagent gas had a stated purity of 99.999 % each and were used, if not otherwise stated, without further purification. The other reagent gases isobutane and methane had purities of 2.5 and 4.5, respectively.
The helium GC carrier gas with a grade of 5.0 was further purified with a HP2 purifier from VICI International (Schenkon, Switzerland) to outlet impurities below 10 ppbV.
The used benzene, toluene and *o*-xylene gas mixtures in nitrogen (5.0) were made in-house and concentrations were confirmed through a calibrated GC-MS analysis. Other reagents that were used in a particular experimental section are discussed in the corresponding chapter of this thesis.

3.2 TOF Data Acquisition and Evaluation

TOF data were acquired with the software package provided by the manufacturer TOFWERK AG (Thun, Switzerland). From the raw data, nominal mass traces or spectral data were exported to a text file and further processed with custom python scripts [53] and Microsoft Excel [54].
Since only nominal mass traces could be exported with the manufacturer's software package, care was taken to ensure that several peaks did not overlap within one nominal mass. Overlapping isotopic signal pattern were corrected manually.

3.3 Computational Modeling

3.3.1 Charged Particle Tracing Simulations

Particle tracing calculations were performed with the SIMION [55] program package, including the Collision Model HS1 user program. This user program implements a hard-sphere collision model, which is useful for simulating non-vacuum conditions. This model is based on the

kinetic gas theory, in which the individual collisions between ions and gas particles are modeled. The expected frequency of the collisions, measured as distance (the mean free path), is predicted by kinetic gas theory as a function of the known pressure, temperature and collision cross-sections of the colliding particles. Collisions between ions and gas particles lead to positive and negative energy transfers as well as to scattering (deflection of the ion velocity vectors) or even absorption (e.g. in electron-gas collisions). The energy transfers can provide both, the kinetic cooling of a fast-moving ion and the kinetic heating of a slow-moving ion. The colliding particles are treated as hard spheres and it is assumed that the collisions are elastic. In general, the background gas is not stationary and has a Maxwell-Boltzmann distribution of velocities, which is a function of temperature [56].

Since SIMION does not have bulk gas flow calculations implemented, these flows were determined with a Computational Fluid Dynamics (CFD) solver. The estimated background gas velocity vector field and the scalar field of pressure were implemented into the SIMION collision model. Detailed information on this hard-sphere approach can be found in the literature [56–58]. For the simulations a complete version of the geometry of the investigated first ion optics elements (SSQ, skimmer) was replicated as a truly scaled SIMION potential array from a CAD drawing.

3.3.2 Fluid Dynamic Simulations

The Autodesk CFD 2019 [59] software package was used for the simulation of three-dimensional stationary computational fluid dynamics (CFD) models of gas flows.
The elementary equations for the flow and heat transfer of fluids are the Navier-Stokes or momentum equations and the first law of thermodynamics or the energy equation. Details on the mathematical principles are available in the Autodesk CFD User's Guide [60].

To reduce computational costs, simplified CAD versions were implemented in the CFD module from Autodesk. All surface details were neglected and approximated to simpler geometries (e.g. round quadrupole rods instead of separate individual quadrupole segments). Otherwise, such details would drastically raise the complexity and make the modeling process rather expensive. Preliminary modeling runs of small detailed sections of the overall setup have shown that under the considered conditions the simplifications made do not significantly affect the results.

The total temperature of 298 K was assumed as a constant value for all calculations without heat transfer, thus the temperature distribution was not included in the simulation runs.
To simulate the mixing of the two considered gases, a diffusion coefficient of 0.76 cm^2 Pa s^{-1} was used [61]. The boundary conditions for the flow simulations were a hydrogen mass flow of $0.75 \cdot 10^{-7}$ kg s^{-1} and a nitrogen mass flow of $1.25 \cdot 10^{-7}$ kg s^{-1} at the inlet boundary and a fixed mass flow through the skimmer of $2.00 \cdot 10^{-7}$ kg s^{-1} at the outlet boundary.
The gas velocity vector results of the CFD simulations were used as input parameters for the background gas velocity in the hard-sphere collision model in SIMION.

3.3.3 Chemical Reaction Simulations

The open-source software package Cantera (Version 2.2.1) [62] was used as differential equation solver for kinetic simulations of the supposed chemical reaction system. Isobar and isothermal conditions in an ideally stirred reactor were assumed in the simulations. All reactions and rate coefficients used in the calculations in this work are listed in Table 14.

3.4 Time-of-Flight Mass Spectrometer

All iterative developed chemical ion source versions were designed and tested on the custom time-of-flight (TOF) mass spectrometer HTOF from TOFWERK AG (Thun, Switzerland). The mass spectrometer has a mass range of 1 – 4000 Da and a resolution of about 3000 at *m/z* 200. A SH-110 scroll pump (Agilent Technologies, Santa Clara, USA) provided the necessary backing pressure of 1 mbar for the turbopump (SplitFlow 310, Pfeiffer Vacuum Technology AG, Wetzlar, Germany). The high vacuum region of the analyzer reached pressures below 10^{-7} mbar.
During the development process, the configuration of the MS with respect to the ion transfer was slightly changed. Figure 2 shows the initial transfer at the beginning of the project. Note, a short-segmented quadrupole (SSQ), located upstream between the skimmer and the ion source, is not shown. Since the distance between this transfer stage and the ion source is a crucial parameter, the SSQ, as well as an alternative quadrupole geometry, are included in the respective sections of the ion source setups (cf. chapter 3.9). The focusing and transfer of the generated ions, considered along the transfer direction, was as follows (cf. Figure 2). The sampled ions entered the second differentially pumped stage through the skimmer into a tube lens ($\sim 10^3$ mbar), followed by a notch with filter orifice ($\sim 10^{-5}$ mbar) and further focusing by an Einzel-lens into the drift region of the analyzer ($\sim 10^{-7}$ mbar). Also, at the expense of transfer

efficiency by a factor of around 2-3, this initial setup was chosen in order to keep a wide compatibility to other TOFWERK MS instruments.
The notch filter allowed a selective ejection of up to four different *m/z* values to prevent the system from overload with bulk gas reagent ions.

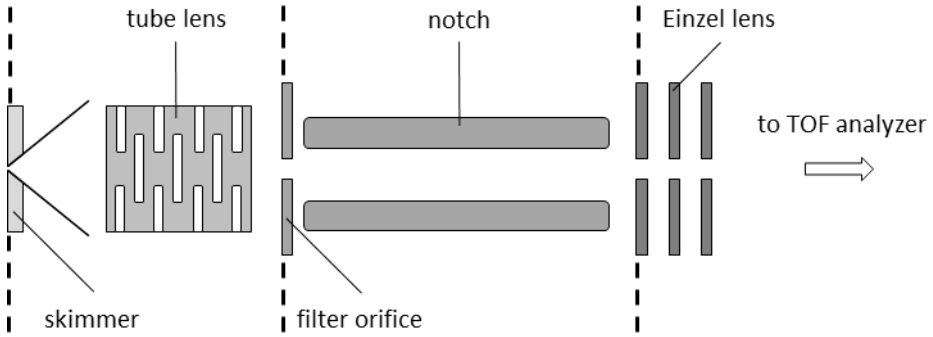

Figure 2: Schematic drawing of the original ion transfer stage configuration of the custom HTOF.

For better ion transmission efficiency, the ion transfer path was slightly changed. The modified version is depicted in Figure 3. The tube lens was replaced by a big segmented quadrupole (BSQ) and the skimmer was exchanged by a standby-valve configuration. The latter allowed for disassembling ion source without venting the entire MS system. Furthermore, the skimmer inner diameter was reduced to 0.7 mm to operate the ion source at a higher pressure without affecting the next differentially pumped stage.

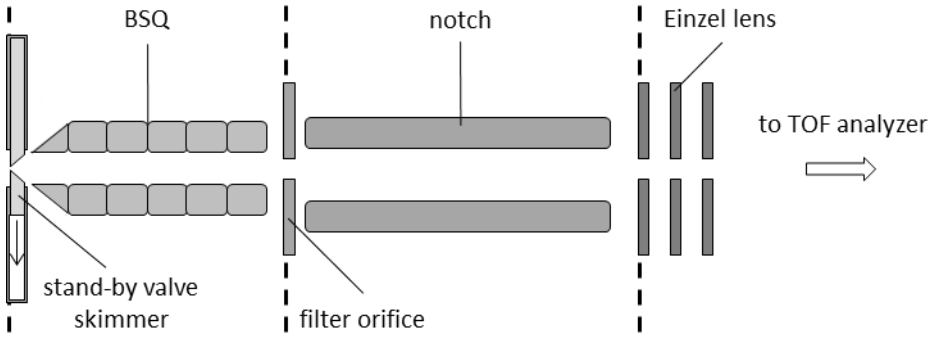

Figure 3: Schematic drawing of the modified ion transfer stage configuration of the custom HTOF.

3.5 Gas Chromatograph

The gas chromatograph (GC) used for all experiments described in this work was a Model 6890A from Agilent (Santa Clara, CA, USA) with a TR-Dioxin 5MS column (30 m, 0.25 mm ID, 0.1 µm film thickness), fed by helium as carrier gas. A custom-built, heated transfer line guided the GC capillary from the GC oven to the ion source and a proportional integral derivative (PID)

controller maintained its temperature at 300 °C, unless otherwise stated. In certain setups also the ion source was heated to approximately 300 °C with a temperature-controlled heating wire (SAF Wärmetechnik GmbH, Mörlenbach, Germany) wrapped around the source. A PID device (Horst GmbH, Lorsch, Germany) in combination with a resistance thermometer (PT100) regulated this temperature.

GC injection was done manually with the full volume a 1 µL syringe and an injector split of 100. The GC temperature program is shown in Table 19 (appendix). All investigated samples contained only one up to three analytes with sufficiently different boiling points, hence the separation efficiency was not crucial.

3.6 Plasma Source

Figure 4 shows the C210 OEM power supply (Heraeus Holding GmbH, Hanau, Germany) to drive the plasma in this work. Typically, it is used for conventional photoionization detectors (PID) with rare gas-filled lamp bodies. The printed circuit board holds a coil of approximately 120 windings and a surrounding, grounded copper cylinder. It nominally operates at 13 MHz with a power input of approximately 0.5 W. This configuration resembles the operational principles of a helical resonator plasma (details see chapter 1.2.1).

Figure 4: C210 OEM power supply.

For regular PID applications a ½ inch diameter, conically shaped PID lamp body is inserted into the coil of the resonator and the emitted UV radiation is utilized. In the following, this original version of the OEM RF power supply is called ***iteration 1***.

However, the present work did not intended to use the emitted VUV radiation for ionization, but instead, the ions produced in the plasma itself. Therefore, the power supply unit was iteratively modified as described in the following.

(***iteration 2.1***) The second iteration involved the replacement of the regular lamp body conically shaped glass by an open glass cylinder. This replacement step significantly improves the commercial applicability. Standard glass tubes become feasible and expensive processing and time-consuming customization (conically shaped glass tubes) is no longer required. For this arrangement, a feedthrough was drilled into the circuit board, which matched the external diameter of the glass tube. All interrupted conductor tracks were carefully rewired. For axial alignment with the helical resonator coil, the glass tube was centered with PVC mountings.
The inserted plasma tube was made of alkaline earth aluminosilicate glass (Glas 8252, Schott AG, Mitterteich, Germany) with a diameter of 12.09 ± 0.15 mm and a wall thickness of 0.94 ± 0.07 mm. Compared to conventional borosilicate glass (DURAN®) the Glas 8252 has an approximate 3 fold lower dielectric loss factor tan δ ($1.1 \cdot 10^{-3}$; 1 MHz, 25 °C) [63]. The dielectric loss factor specifies the amount of electrical energy absorbed and lost in the material, i.e., the energy that is converted into heat and thus not available for plasma generation.

(***iteration 2.2***) The trimming potentiometer on the circuit board was replaced by a 50 kΩ 10-turn precision potentiometer (Vishay Intertechnology Inc., Malvern, PA, USA). This allows accurate adjustment of the operating frequency to optimize the plasma output. In addition, a transistor of the common collector circuit was exchanged by a BD 139 transistor (STMIcroelectronics, Genf, Switzerland), which lead to an increase of the current consumption and a doubling of the produced ion current.

(***iteration 3***) In the last modification, the power supply circuit board was decoupled from the helical resonator coil and the grounded shield. The original coil is an enameled copper wire, fixed on a Tufnol® cylinder and it was replaced by a ceramic wire (KD 500 NPC, Karl Schupp AG, Zollikerberg, Switzerland) directly wounded on the plasma tube. This ceramic coated wire has a high permanent temperature resistance of up to 500 °C. This step enabled the remote operation of the plasma. Regarding the application in a GC ion source, this permits the heating of the entire source including the plasma region without affecting the electronics on the circuit board.

3.7 Plasma Spectroscopy

For optical emission measurements in the ultraviolet (UV) to the visible (VIS) spectral range, a iHR320 spectrometer (HORIBA Ltd., Kyoto, Japan) equipped with a 1800 groves mm^{-1} grating was used. A 220F fiber adaptor (HORIBA Ltd., Kyoto, Japan) was radially positioned on the plasma tube, 5 mm downstream from the helical resonator shielded antenna and transmitted the light to the spectrometer.

The signal was recorded by a photomultiplier tube (DPM-HV, HORIBA Ltd., Kyoto, Japan) and a subsequent acquisition controller (SpectrAcq3, HORIBA Ltd., Kyoto, Japan). The spectrometer was scanned between 300 and 700 nm with 0.05 nm step size. The entrance and exit slits were set to 0.10 mm and the data were obtained in a single accumulation with a 0.1 s integration time.

The wavelength calibration was done by means of known Hg spectral lines from a UVP standard mercury Pen-Ray lamp without absolute calibration of the system.

3.8 Ion Current and Transmission Measurements

3.8.1 Setup on the Vacuum Recipient

Ion current and ion transmission measurements were performed with a custom-built measurement chamber consisting of a vacuum recipient with an ion current measuring electrode system. Due to the electrode arrangement, as shown in Figure 5, this design allowed to measure the primary ion current without interfering photoelectrons.

The vacuum recipient was equipped with a rotary vane pump to establish a minimum pressure of approximately 1×10^{-3} mbar. The pressure was monitored with a 10 mbar full-scale capacitance manometer (622 AX 11 MDE, MKS Instruments, Andover, MA, USA). By restricting the flow with a valve on the connection to the vacuum pump, the pressure within the recipient could be adjusted. The plasma region was fed with a hydrogen gas flow introduced at one end of the glass tube via a mass flow controller (2 L min^{-1}; Mass-Flo-Controller; MKS Instruments, Andover, MA, USA). A modified helical resonator OEM RF power supply (Heraeus C210; Heraeus Holding GmbH, Hanau, Germany) maintained the hydrogen discharge inside the glass tube.

Two electrodes were mounted inside the vacuum chamber electrically isolated through a *polytetrafluoroethene* (PTFE) holder. The measurement of the ion current was done by a sensitive electrometer (Keithley 6430 Sub-Femtoamp remote Source Meter, Keithley

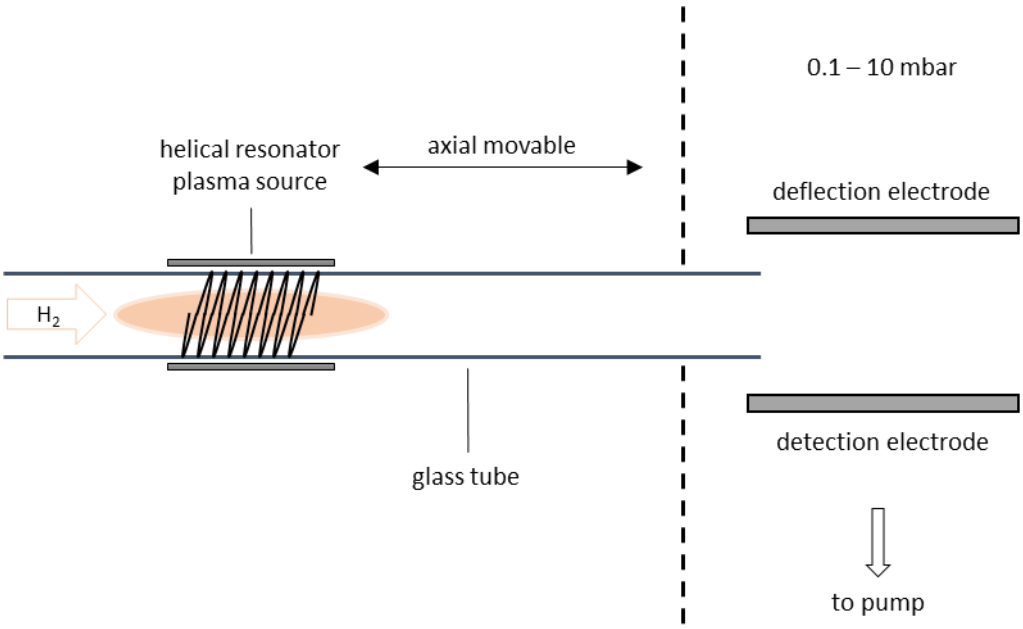

Figure 5: Schematic drawing of the ion current measurement setup.

Instruments Inc., Cleveland, OH, USA). The output of the 6430 Sub-Femtoamp meter was manually recorded by reading the analog scale of the pointer instrument. The measuring electrodes were aligned in parallel to the exit of the glass tube. On one electrode an adjustable deflection voltage of 0 to ± 300 V was applied to direct one ion polarity toward the detection electrode with the connected electrometer, whereas the oppositely charged ions were pulled to the deflection electrode.

All measurements were done with parameters resembling the operational conditions of the chemical ionization source on the time-of-flight mass spectrometer.

3.8.2 Setup on the TOF-MS

Investigation of the ion transfer efficiency of the developed chemical ionization source setup 3 also necessitated current measurements within the time-of-flight mass spectrometer configuration. The custom TOF-MS is described in detail in chapter 3.4 and for a detailed ion source setup description see chapter 3.9.3.
The circuit for measuring the ion current was designed in such a way that the TOF-MS system could simultaneously continue to operate in normal measuring mode. Figure 6 shows the arrangement of the ion transfer electrodes with the corresponding applied voltages. The respective ion currents were measured along the ion transfer on i) the entrance lens at the

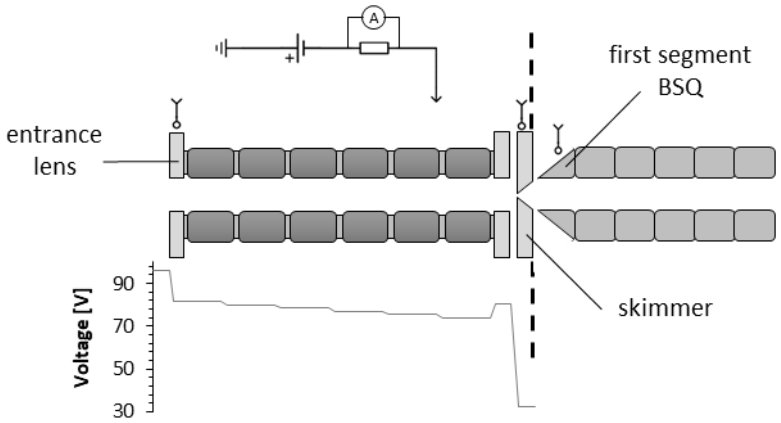

Figure 6: Schematic drawing of the ion transfer electrode arrangement, applied voltages and electronic circuit for ion current measurements.

beginning of the short segmented quadrupole (SSQ), (ii) the skimmer at the end and (iii) the first segment of the big segmented quadrupole (BSQ) in the first differentially pumped stage of the MS.

A digital multimeter (VOLTCRAFT VC870, Conrad Electronic SE, Hirschau, Germany) was connected in series between the ion transfer electrode and its power supply. Ions striking the electrode changed its potential relative to the reference point. The potential difference was measured as a voltage drop across the internal resistance of the multimeter and converted into an ion current. The voltage on the respective measuring electrode was varied in a range of + 135 V to - 135 V.

3.9 Ion Source Development

All measurements during the process of development were done on the custom time-of-flight mass spectrometer described in chapter 3.4. A brief description of the ion source setups of each iteration is given in the following.

A detailed discussion of the process itself, the iterative steps based on results and knowledge gained from other experiments can be found in chapter 4.4.

3.9.1 Ion Source Design 1

For Design 1 the µ-plici 2.2 ion source, previously developed in the work by D. Müller [64], was adapted to the helical resonator RF plasma, as schematically shown in Figure 7. The µ-plici 2.2 is a stacked chamber system, with each compartment separated through an orifice to virtually split the chemistry into different, individual zones. Here, the helical resonator plasma source

iteration 2.1 (cf. chapter 3.6) was directly attached to the first zone, which in total confined the entire ion chemistry into three subsequent chambers.

The first chamber incorporated the RF hydrogen plasma to generate the primary charge carrying species H_3^+. An aperture separated the first reagent gas compartment from the plasma chamber. The second chamber was aligned in a flow tube arrangement with an inner diameter of 1.5 mm and with a length of 5.4 mm. A reagent gas or a reagent gas containing analyte was added perpendicular to the gas flow directly downstream of the aperture.

The geometry of the third compartment was identical to the second and both could be used simultaneously or separately. Each segment was separated by an interchangeable orifice with diameters ranging from 60 to 200 µm.

The effluent from the last chamber was axially introduced into the short segmented quadrupole. Optionally, an analyte containing gas could be introduced coaxially through a 1/16 inch stainless steel capillary, directly between the SSQ entrance lens and the chamber orifice.

To maintain the optimum operating pressure of the SSQ in both measuring modes - monitoring and GC mode - the SSQ chamber was equipped with a high capacity scroll pump Fossa FO 0035 A (Dr. –Ing. K. Busch GmbH, Maulburg, Germany) with a pumping speed of up to 35 $m^3\ h^{-1}$. The pumping speed of the scroll pump was manually adjusted by a valve in order to keep the pressure constant at different total gas flows.

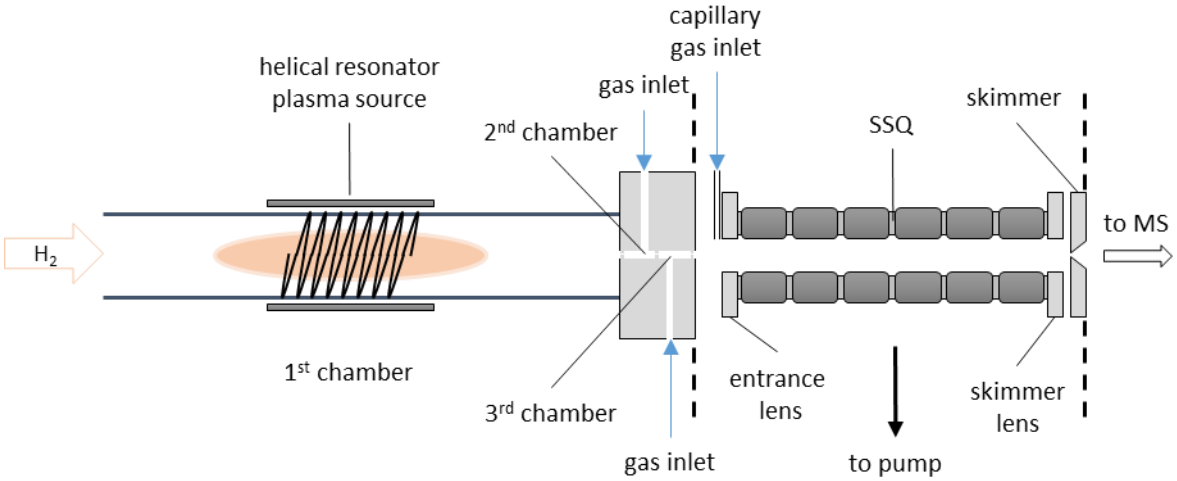

Figure 7: Schematic drawing of the ion source Design 1.

3.9.2 Ion Source Design 2

A schematic drawing of the second ion source design is depicted in Figure 8. This setup was made of a single continuous glass tube (alkaline earth aluminosilicate glass, Glas 8252, Schott AG, Mitterteich, Germany), divided into two regions, the ***plasma region*** and the ***reaction***

region. In the first region, the helical resonator source *iteration 2.1* (cf. chapter 3.6) surrounded the glass tube and maintained an axially confined plasma. Hydrogen was supplied through a mass flow controller (Mass-Flo-Controller, MKS Instruments, Andover, MA, USA) to generate the primary charge carrying species H_3^+. Two consecutive 1/16 inch stainless steel capillary inlets marked the transfer to the reaction region. Both allowed for a precisely centered addition of reagent and analyte gas, respectively. Further downstream a 4.5 cm long RF-only quadrupole followed, to immediately pick up analyte ions and enhance the transfer efficiency. The rods were made of stainless steel and directly attached to the outer surface of the tube. As an RF driver, the TOF internal SSQ RF driver was used. The entire gas - plasma, reagent and analyte - was transported to the skimmer, where a differential pumping stage with a high capacity scroll pump Fossa FO 0035 A (Dr. –Ing. K. Busch GmbH, Maulburg, Germany) kept the required pressure through a manual valve control.

It should be noted that, alternative to the Glass 8252, also resistive glass tubes (~4200 MΩ PHOTONIS Inc., Sturbridge, MA, USA) were tested in order to apply an axial DC bias. This would have allowed an additional accelerating field in flow direction. However, manufacturing tolerances with respect to the roundness caused severe sealing issues. Consequently, no further experiments were conducted in this direction.

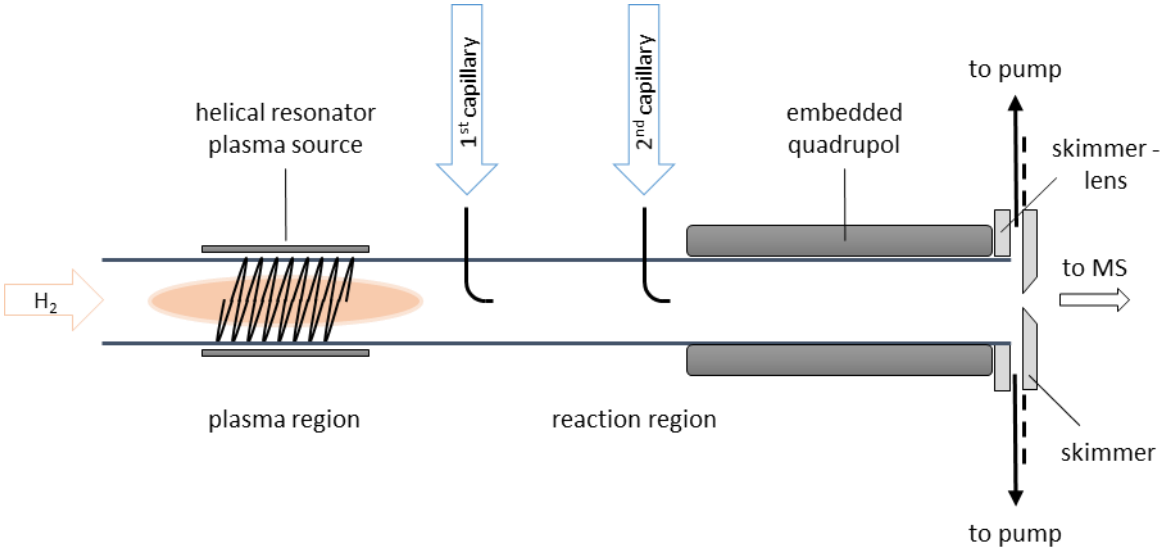

Figure 8: Schematic drawing of the ion source Design 2.

3.9.3 Ion Source Design 3

Figure 9 shows a schematic drawing of the ion source Design. 3. The essential two parts were the plasma tube and the reaction tube, both made of alkaline earth aluminosilicate glass (Glas 8252, Schott AG, Mitterteich, Germany). The plasma tube was equipped with the helical resonator source *iteration 2.1* (cf. chapter 3.6) and supplied with hydrogen through a mass flow controller (Mass-Flo-Controller, MKS Instruments, Andover, MA, USA). The plasma zone was axially confined and produced H_3^+ as the primary charge carrying species. In the subsequent reaction region, efficient ion chemistry formed the protonated analyte ion. Both, the reagent gas and the GC effluent were added perpendicular to the main hydrogen flow in the intermediate section between the plasma and the reaction compartment. The reagent gas inlet was tangentially aligned, whereas the GC column outlet was exactly placed on the center axis of the tube. For an optimized ion transfer, the reaction tube was directly mounted and axially aligned to the SSQ chamber, which is also the first differentially pumped compartment of the TOF instrument. The pressure was maintained at around 6 mbar with a high capacity scroll pump Fossa FO 0035 A (Dr. –Ing. K. Busch GmbH, Maulburg, Germany) and an additional manual valve control.

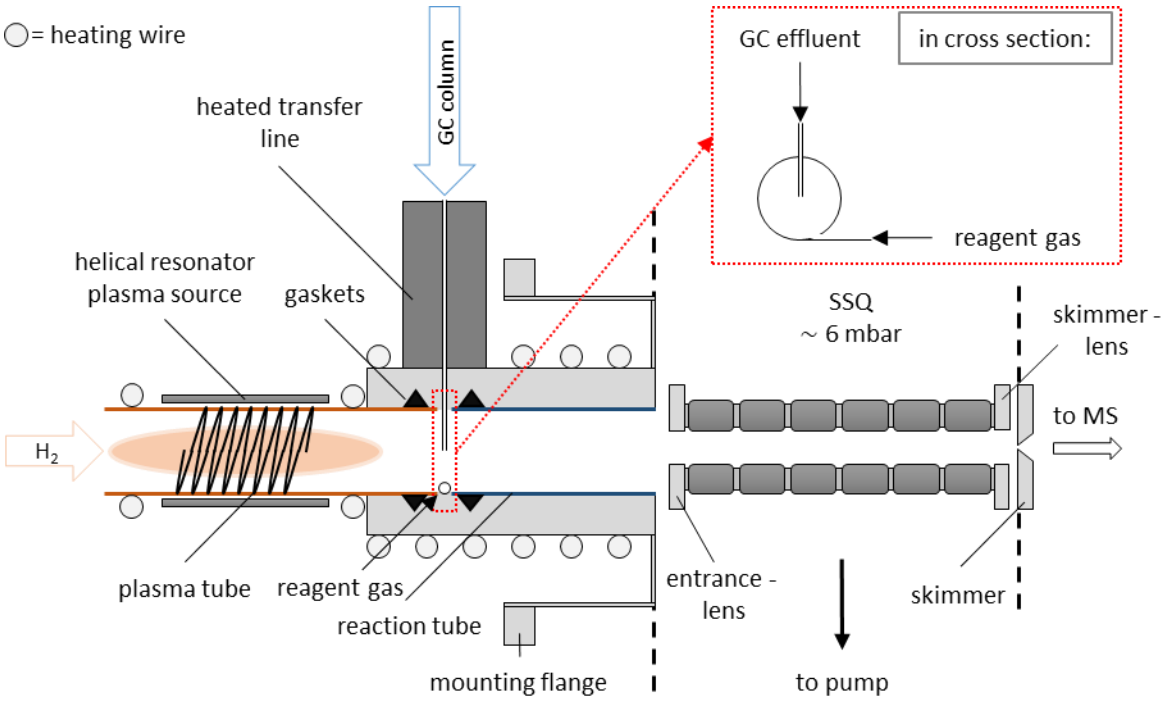

Figure 9: Schematic drawing of the ion source Design 3. *Dashed box:* cross sectional view of GC effluent and reagent gas inlet.

A temperature-controlled heating wire (SAF Wärmetechnik GmbH, Mörlenbach, Germany) was wrapped around the source enclosure and kept the ion source and the plasma tube at up to 300 °C. The control unit consisted of a thermocouple (Type K) and a PID device from Horst GmbH (Lorsch, Germany). Continuous heating of the GC column between the oven and the source inlet was provided with the custom-built linear transfer line as described in chapter 3.5. The necessary heat-resistive and non-outgassing sealing of the two glass tubes were accomplished with rectangular graphite gaskets (Hülsebusch Dichtungstechnik e.K., Wesel, Germany). These gaskets are made of expanded pure graphite foil (> 99.8%), which is pressed into elastic sealing rings without a binder. The tubes were radially sealed by compressing the gasket in a conically shaped groove.

3.9.4 Ion Source Design 4

A schematic drawing of the last ion source iteration Design 4, is depicted in Figure 10. The underlying geometry of the plasma zone, the reagent gas and GC effluent addition and the reaction region have remained essentially the same as in the ion source Design 3.

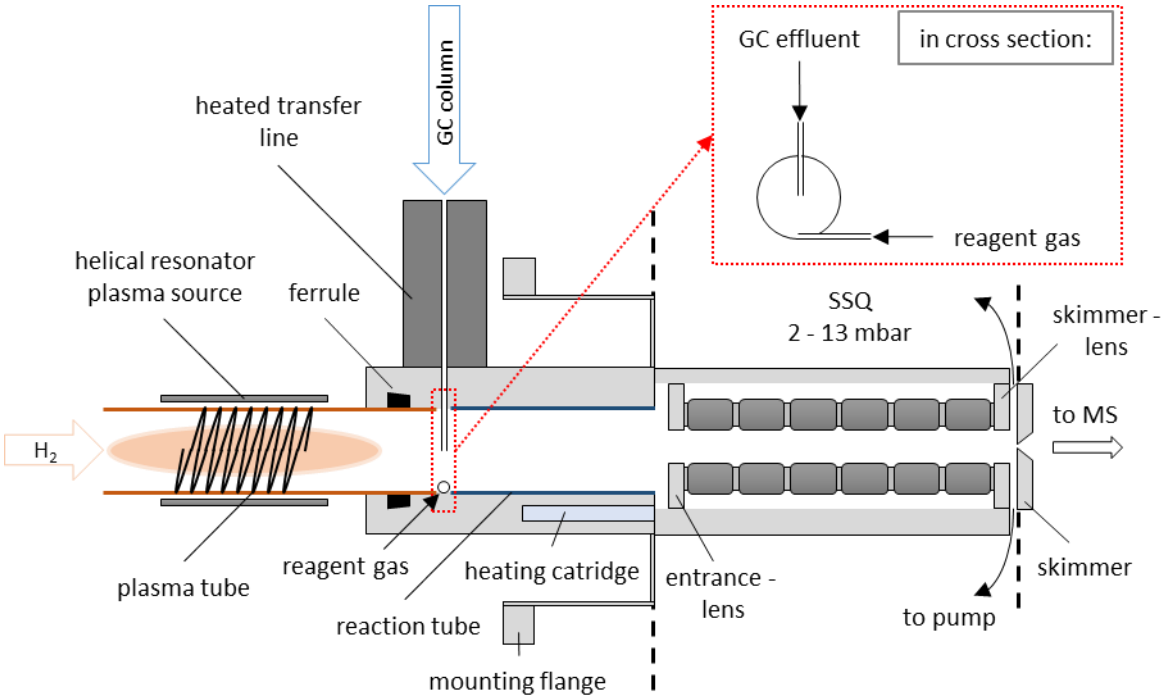

Figure 10: Schematic drawing of the ion source Design 4. *Dashed box:* cross-sectional view of GC effluent and reagent gas inlet.

A aluminosilicate glass, a ½ inch borosilicate glass tube (SIMAX®, Pegasus Industrial Secialities Inc., Cambbride, ON, Canada) was used as the plasma tube. This enabled the use of standard ½ inch graphite/Vespel ferrules (BGB Analytik Vertrieb GmbH, Rheinfelden, Germany) for heat-resistive and non-outgassing sealing of the plasma tube. The plasma tube was equipped with the helical resonator source *iteration 2.1* (cf. chapter 3.6) and supplied with hydrogen through a mass flow controller (GCF mass flow controller, Aalborg Instruments and Controls Inc, Orangeburg, NY, USA.).

The essential difference from the preceding ion source Design 3 is the housing of the SSQ. This directs the entire gas stream towards the skimmer, where the ions are extracted and the neutral gas is pumped away by the differential pumping stage. The ion source including the SSQ housing was heated to up to 300 °C by a temperature-controlled heating cartridge integrated into the ion source enclosure.

4. Results and Discussion

4.1 Modifications of the Plasma Source Power Supply

To characterize the RF power supply and to evaluate its performance after each modification step, various measurements were carried out, starting with ion current measurements. The ion current measurements were performed with the vacuum recipient setup described in detail in chapter 3.8.1. These were followed by measurements on the time-of-flight mass spectrometer with selected setups.

In a first step, the operating frequency of the helical resonator was examined. Previous measurements have shown that the power supply covers a frequency range from 11.7 to 16.8 MHz. The frequency can be adjusted via a trimming potentiometer on the circuit board. With the original coil (*iteration 2.1,* cf. chapter 3.6) a hydrogen plasma can be driven in the range of 11.2 to 13.5 MHz. Figure 11 shows the ion current as a function of the operating frequency. It can be seen that the current is strongly affected by the frequency, with a maximum at about 12.05 MHz.

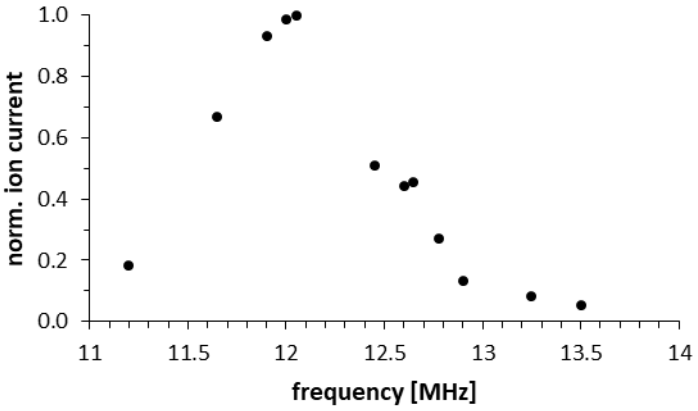

Figure 11: Ion current as a function of the RF power supply (*iteration 2.1*) operating frequency.

Since the helical coil is operated in an electrical resonance state, the observed maximum should reflect the resonance frequency of the helical structure. According to a quarter-wave resonator as described in chapter 1.2.1 and with the present coil geometry (wire length, coil diameter,

number of turns), a theoretical helical resonance of 12.08 MHz is calculated which closely corresponds to the observed maximum.
Attention is drawn to the fact that the current consumption of the RF power supply also varies as a function of the frequency and correlates with the measured ion current. Plotting the measured ion current versus the power consumption of the RF power supply device reveals, that the measured ion current increases proportional with increasing power consumption (cf. Figure 12). The slope is > 1, which suggests that the applied power is coupled into the plasma more effectively to the resonant frequency.

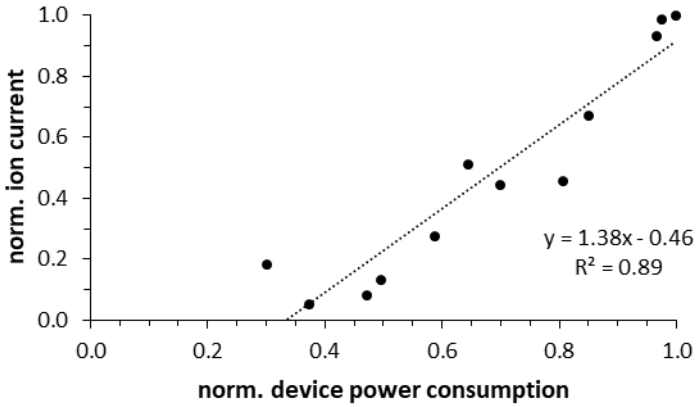

Figure 12: Ion current as function of the RF power supply (*iteration 2.1*) power consumption.

This correlation could be used in the future to further optimize the helical resonator plasma source. As described in section 3.6, the board is equipped with a potentiometer for manual adjustment of the operating frequency. Automatic regulation to the maximum current draw of the RF power supply utilizing an electronic circuit could thus be used to regulate the driving frequency, which also corresponds to maximum ion yield.

As described in detail in chapter 3.6, the original OEM RF power supply was modified in several iterations. The RF power supply modification *iteration 2.1* was compared with the versions *iteration 2.2* and *iteration 3*, the latter with different custom coils (i, ii, iii). For each iteration, the frequency was adjusted to the highest ion current
Figure 13 shows that each iteration step improved the performance. By replacing the transistor on the circuit board with a BD 139 transistor the ion current was doubled (cf. *iteration 2.1* vs. *iteration 2.2*). It is noted that this is also observed in the respective RF Power supply current input. For *iteration 2.1* and *iteration 2.2* the current input was in the range of 0.10 – 0.11 A and 0.21 - 0.22 A, respectively.

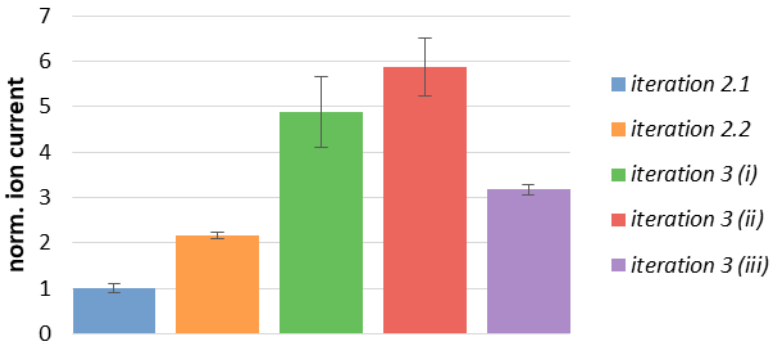

Figure 13: Ion current measurements of different RF power supply modifications. *Iteration 3* with custom coil (i) 12.3 MHz; (ii) 15 MHz; (iii) 16.5 MHz.

Remotely operating the plasma with a self-wound coil directly on the plasma tube enhanced the ion current even further, as shown with *iteration 3* for three different resonator coils. Each coil was tightly wound directly onto the plasma tube and differed only in the number of turns and thus the length. These lengths have been chosen so that the calculated resonance frequencies lies within the adjustment range of the RF power supply. The frequencies of coil (i), coil(ii) and coil (iii) are at 12.3 MHz, 15.0 MHz and 16.5 MHz, respectively. Coil (i) and (ii) generated significantly higher ion currents, however, the standard deviation of successive measurements, represented by the error bars in Figure 13, showed considerably weaker signal stability than coil (iii). The latter obtained comparable signal stability as the original RF power supply *iteration 2.1* but with a threefold higher ion current. With its 118 windings, the coil was of a similar dimension (e.g. coil length) as the original one (120 turns).
The described results successfully demonstrates that a remote operation of the plasma is possible and still leaves significant room for improvement. It enabled heating of the entire source including the plasma region without affecting the electronics on the circuit board.

With the RF power supply *iterations 2.1* and *2.2* measurements were also carried out with the CI ion source Design 3 on the time-of-flight mass spectrometer. Figure 14 compares the mass spectra recorded with both iterations under otherwise identical conditions. A benzene, toluene and xylene mixture of about 10 ppmV (exact composition cf. Table 16, #2; appendix) in N_2 was added for analysis. The spectra show the total ion current (TIC) increases by a factor of two with the modified power supply, while the mass signal ratios remained approximately the same. The signal-to-noise (S/N) ratio was improved by 25 %. These results are fairly consistent with the ion current measurements described earlier (cf. Figure 13).

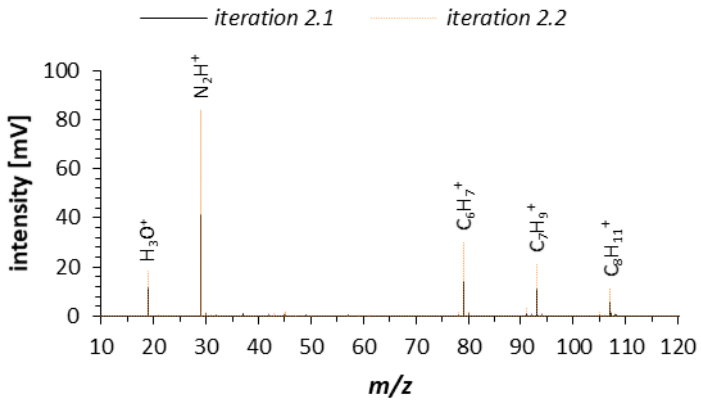

Figure 14: Mass spectra of 1 sccm benzene, toluene and *o*-xylene mixture in N_2 (cf. Table 16, #2, appendix) recorded with two different RF power supply modifications.

4.2 Challenges of Ion Current and Transmission Measurements

Ion current measurements close to a high-density plasma can be challenging. Using only electrostatic methods it can be difficult to measure absolute ion currents, e.g. due to space charge effects. Another difficulty can arise at high deflection voltages, especially in combination with gases that have a low breakdown voltage. Whenever a critical reduced field strength is reached in the presence of free electrons, background gas molecules can be ionized and thus distort the measured ion current. In the presence of highly energetic radiation (VUV/UV), free electrons can be generated by the *photoelectric effect* on the surfaces. Ion current measurements are discussed in the following two subchapters under consideration of these effects.

First, the hydrogen plasma is optimized to obtain the maximum primary ion current for subsequent chemical ionization cascades leading to ionization of the molecules of interest. The measurements are carried out on a carefully designed setup with the measurement electrode and the deflection electrode off-axis to the light emitting plasma to avoid interferences with photoelectrons.
Secondly, to achieve the maximum possible sensitivity, ions created in the chemical ion source region at medium pressure must be transmitted with high efficiency through the differentially pumped transfer stages before reaching the high vacuum region of the TOF mass analyzer. In the instrument's high vacuum regions ions can be guided with electric fields. At elevated pressures, collisions with gas molecules increasingly dominate the behavior of the ion motion and these regions largely determine the overall ion transmission efficiency of the mass

spectrometer. Therefore, ion transmission measurements are also carried out using the TOF in the same operation mode as during standard measurements. This gives an inside into the crucial region from the medium pressure ion source region including the first transfer unit (SSQ) to the next differentially pumped stage of the TOF-MS.

4.2.1 Measurements at the Vacuum Recipient

Pressure dependencies on the primary ion current, and ion transmission efficiencies of the RF power supply *iteration 2.1* (cf. chapter 3.6) were measured with the custom-built chamber assembly described in detail in section 3.8.1.
The blind current of the detection assembly was below 1 fA throughout the measurements. The pressure was varied between 0.2 and 2.6 mbar. Furthermore, the distance of the plasma center to the current detection assembly was altered from 7 to 23 cm, which corresponds to ion dwell times of 0.2 ms up to 9 ms, calculated according to the pressure normalized volume flow rates. This conversion applies in a first approximation and is in good agreement for viscous laminar flow conditions. Note, however, that for the given geometry a fully developed laminar viscous flow can be assumed only for pressures > 1.1 mbar. For the measurement series at 0.18 and 0.5 mbar, the conditions according to the upper limit of the transitional Knudsen flow were not met and the system essentially was between the viscous and the molecular regime. Therefore, a deviation from the true residence time might occur in those cases.

In Figure 15, the logarithmic ion current is plotted in dependence of the dwell time for different pressures. As expected, the longer the ions resided inside the glass tubes, the less current was detected. For pressure conditions of 0.18 mbar this decline is nearly linear on the logarithmic scale and kinetically it essentially follows a first order charge loss mechanism. Since reactions on surfaces often correspond to this order, it is assumed that the positive charge in this pressure regime is primarily lost to the walls. With increasing pressure, however, the curves significantly deviate from a linear trend and the slope falls off with increasing distance, which indicates the presence of secondary charge loss processes. These effects are similar to the ones observed and investigated in the field of flowing afterglows. Here, the overall ion number density decreases with increasing distance along the flow tube, mainly as a result of ambipolar diffusion to the walls. At higher charge densities ($\geq 10^8$ cm^{-3}) also electron-ion recombination, which are often found to be 100 to 1000 times faster than ion-neutral reactions [65], play a significant role in the charge losses.

Ambipolar diffusion results in rapid and mass dependent loss of ions toward the flow tube walls [66]. It is governed by the mobility of the electrons, which is high due to their small size

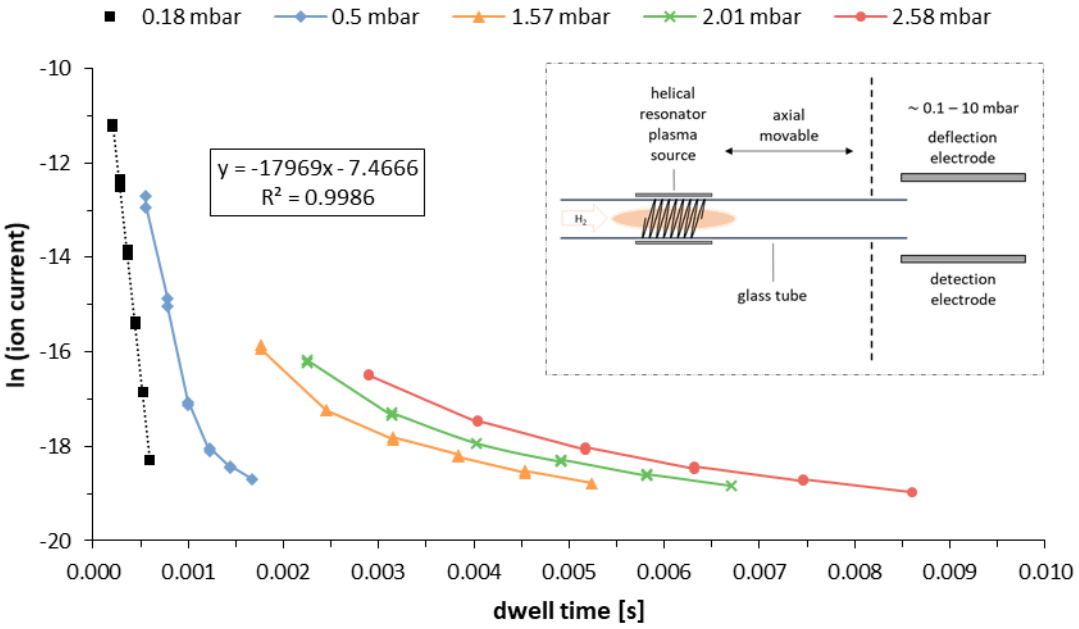

Figure 15: Ion current measurements of the RF power supply *iterations 2.1* for different pressures with varying distances between the plasma core and the detection assembly. The latter were converted to effective ion dwell times inside the glass tubes of the plasma and reaction region. A deflection voltage of 50 V was applied.

and mass. The electrons rapidly diffuse towards the walls and produce a charge imbalance near the axis of the tube. This creates restoring electrical forces driving positive ions outward with enhanced rate.

For predominantly viscous gas flow conditions and the assumption that the ion-velocity radial profile is identical to that of the carrier gas, a continuity equation for ions lost by ambipolar diffusion is given by Bolden *et al.* [67]. This equation can be readily solved analytically, if the axial diffusive contribution and the reactive loss of ions are neglected, resulting in [67, 68]:

$$[A^+]_z = [A^+]_0 \, e^{-\left(\frac{\Delta D_a z}{a^2 v_0}\right)} \tag{1}$$

Where $[A^+]_0$ is the initial ion density and $[A^+]_z$ is the ion density at z cm downstream from creation, D_a is the ambipolar diffusion coefficient, Δ is a pressure dependent factor related to the wall slip coefficient, a is the radius of the plasma tube and v_0 the bulk gas velocity. Plotting the logarithm of the ion density at any given point z as function of the distance will lead to a linear correlation, since all other parameters are constant. The rearrangement of equation 1 to

$\ln[A^+]_0$ can also be used to approximate the initial ion current and consequently the plasma density. By means of the linear regression of the 0.18 mbar measurement series in Figure 15, and assuming the first order ambipolar diffusion as the dominating loss mechanism in this pressure regime, an initial plasma ion current of about 0.6 mA can be approximated, which relates to a plasma density of $1 \cdot 10^{12}$ cm^{-3}. Such numbers are quite realistic for the helical resonator plasma as reported by Liebermann *et al.* [35].

The observed deviation from linearity with increasing pressure indicates the occurrence of secondary effects. As already mentioned, electron-ion recombination is a feasible candidate. In the literature, H_3^+ has been extensively investigated with regard to the kinetics of a binary dissociative recombination [69] and it is expected to be the dominating plasma species (cf. Figure 16).

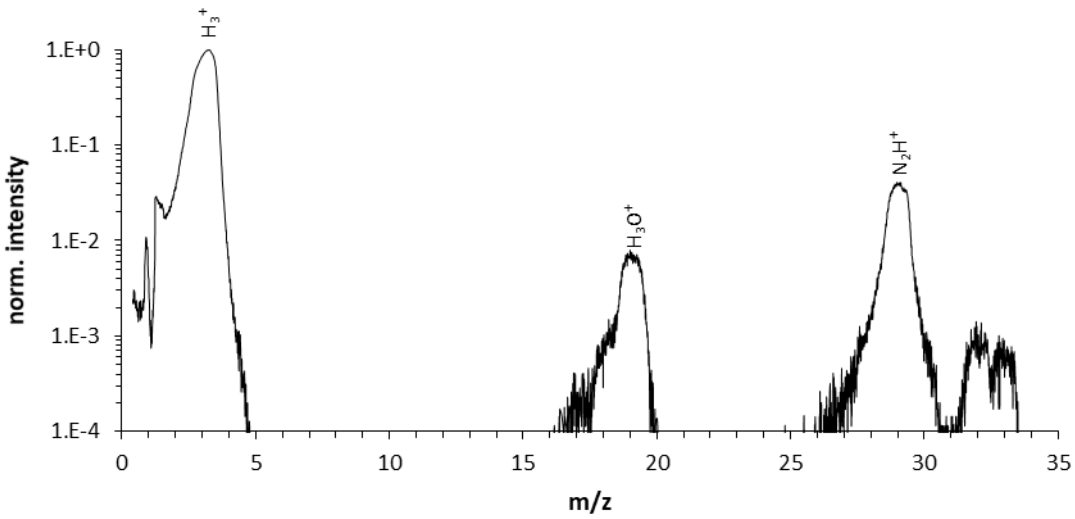

Figure 16: Mass spectrum of a hydrogen plasma ignited by the helical resonator plasma source mounted on a quadrupole MS. Approximately 0.4 ms dwell time at 0.6 mbar.

Among others, the flowing afterglow technique has been used to determine the second order rate coefficient for various conditions. In these experiments, the electron density with varying distance to the plasma plume is determined with a Langmuir probe. The data are analyzed according to a simple second order approach in which the slope directly relates to the rate coefficient and the intercept gives the inverse of the initial electron density. Typical rate coefficient for this process are in the order of 10^{-7} cm^3 s^{-1}. Equally, the ion density can be measured with varying dwell times and analyzed by means of a second order kinetics. Comparison with the literature value might allow to evaluate the presence of dissociative

recombination in the observed ion losses. Assuming a quasi-neutral plasma with $[A^+] \approx [e^-]$ an integrated second order law of the form:

$$\frac{1}{[A]} = \frac{1}{[A]_0} + kt \tag{2}$$

is derived and the same data as in Figure 15 were plotted accordingly. Figure 17 shows rather good fits for the 1.57, 2.01 and 2.58 mbar measurement series. However, the slopes suggest rate coefficient of $2.2 \cdot 10^{-5}$, $1.4 \cdot 10^{-5}$ and $9.4 \cdot 10^{-6}$ $cm^3\ s^{-1}$, respectively, which are approximately two orders of magnitude larger than the reported literature values. Consequently, the recombination process alone cannot account for the observed current-time progression.

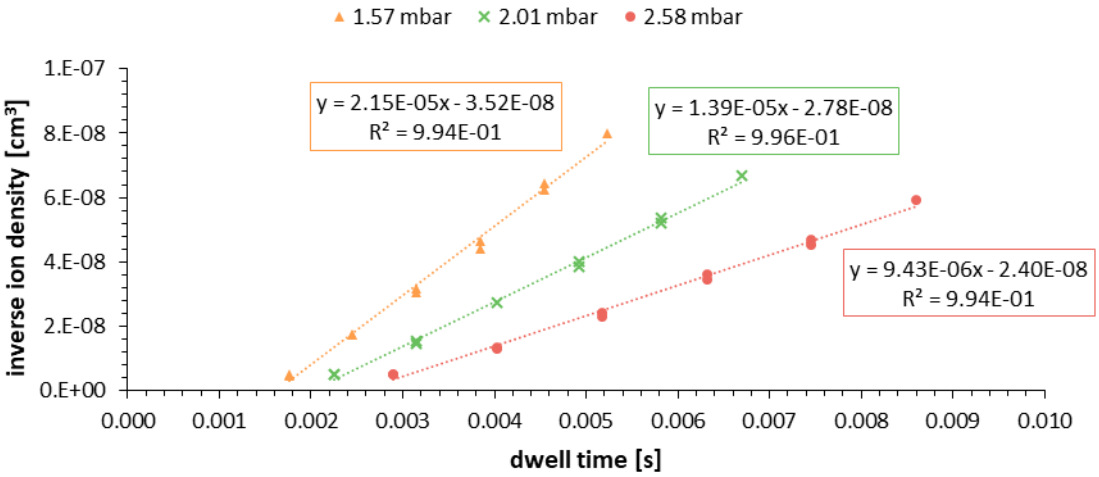

Figure 17: Inverse ion density as function of the ion dwell time for different pressures in the range of 0.2 to 2.6 mbar. A deflection voltage of 50 V was applied.

A third process that should be considered in this context is the ion chemistry. As seen from the mass spectrum depicted in Figure 16 obtained with the same setup on a quadrupole MS (HPR60, Hiden Analytical Limited, Warrington, England), the formation of H_3^+ is relatively fast (µs range), whereas transformations processes with trace impurities are much slower. Under the given conditions – 0.4 ms residence time at 0.6 mbar - the impurity related signals *m/z* 19 (H_3O^+) and *m/z* 29 (N_2H^+) start to increase, however, H_3^+ is still the main charge carrying species. The higher the pressure and the longer this reactive mixture remains in a collisional dominated regime, the more H_3^+ will transfer its proton to those impurities. This goes along with a significant mass change of the charge carrier. Since the ambipolar diffusion loss rate is

proportional to the mobility, and consequently inversely proportional to the square root of its mass, the overall charge drift will be slowed down when H_3^+ is steadily converted to N_2H^+. Thus the ambipolar diffusion coefficients substantially depend on the relative respective ion concentrations [70], which, over time, could also affect the initial first order loss rate.
Whether a reduction in ambipolar diffusion was due to the reduced overall ion density or the transformation of the charge carrying species via ion-molecule reactions is not known, but a general trend is clearly visible: (i) the overall ion number density decreased with distance along the plasma tube, (ii) at short dwell times the rate of ion loss was very high and decreased with increasing pressure and dwell time.

These results demonstrate that the ion loss on the plasma tube was not negligible. The reaction time, and therefore the plasma tube length, should be as short as possible to reduce these loss effects and maximize the ion density of the primary charge carrying species H_3^+. A careful balance has to be found between a maximum ion density of H_3^+ and minimum plasma afterglow effects, as described in detail in chapter 4.5. A closer look at equation 1 suggests that shorter and wider tubes with faster flowing plasma gas produce larger $[A^+]_z/[A^+]_0$ ratios, and consequently increase the primary ion current. Since the diameter of the plasma tube is determined by the helical resonator geometry and the reaction tube is limited by the SSQ geometry, the only variable left from equation 1 is the plasma gas velocity. With regard to the discussed ion chemistry, the addition of a heavier reagent gas can also reduce charge losses by slowing down the ambipolar diffusion to the wall. The same should hold true for an increase of the pressure, since the diffusion is inversely proportional to the gas density.
Regarding the ambipolar diffusion, some negative-ion reaction studies have shown that adding gases with high electron affinity, such as SF_6, significantly reduced the loss rate. Sulphur hexafluoride has a large electron capture cross section and thus rapidly becomes the predominant negative charge carrier, when added in trace amounts to the plasma. This means the electrons do not longer control the rate of diffusion. The addition of an electron attaching gas should also increase positive ion signals by reducing the rate of recombination, which is about two orders of magnitude higher with electrons than with polyatomic negative ions [71].

4.2.2 Measurements at the TOF-MS

To determine the ion transfer efficiency of the developed ion source setup, ion current measurements were directly carried out at the custom time-of-flight mass spectrometer as described in detail in chapter 3.8.2. Pre-optimized ion source parameters were used for all

measurements of this series (cf. Table 18, setting #2, appendix). The hydrogen plasma gas flow was set to 50 sccm and 5 sccm nitrogen was introduced as reagent gas. In addition, a continuous gas flow of 1 sccm of a benzene/toluene/xylene mixture in nitrogen (cf. Table 16, # 3, appendix) was added for analysis. The whole ion source and SSQ chamber were held at a pressure of around 6 mbar. The hydrogen plasma was operated with the RF power supply version *iteration 2.2* at 15 V and with a current consumption of 0.2 A. The respective ion currents were measured (i) at the entrance lens at the beginning of the SSQ, (ii) at the skimmer at the end of the SSQ and (iii) at the big segmented quadrupole (BSQ) in the first differentially pumped stage of the MS. Using the electronic circuit described in chapter 3.8.2, the ion current can be calculated according to Ohm's law:

$$I = \frac{U}{R_I} \tag{3}$$

Where I describes the ion current, U the measured potential difference and R_I the internal resistance of the multimeter (10 MΩ).

Figure 18 shows the results of the ion current measurement at the entrance lens and at the skimmer. The respective electrode potential difference was calculated as the potential between the applied voltage on the measuring electrode and the previous electrode in the ion transfer. Ion currents at positive potential differences were caused by negative ions (grey background) and vice versa.

For the entrance lens, no distinct, prior transfer electrode is present. Results from other measurements suggest an imbalance between charge landing and depletion at the surface of the reaction tube, which eventually leads to a surface potential dissimilar to ground. Thus, the end of the reaction tube forms the counter electrode for the entrance lens with unknown potential. However, with the assumption that the lowest ion current should be measured at a potential difference of 0 V, a potential of about 5 V can roughly be estimated for the reaction tube by simply extrapolating the two data series near zero and determining the intersection.

It is striking that the data series of both electrodes presented in Figure 18 follows a similar trend. Note the logarithmic presentation of the y-axis. In fact, for a simple transmission measurement of a primary beam of charges one would expect an initial linear current increase that eventually levels off at a certain potential, marking the 100 % collection efficiency at this electrode. The measured ion currents, however, show an exponential behavior with an increasing potential difference and the slopes are essentially the same, irrespective of polarity and electrode. This suggests that in all cases (i) more than merely the charges from the plasma

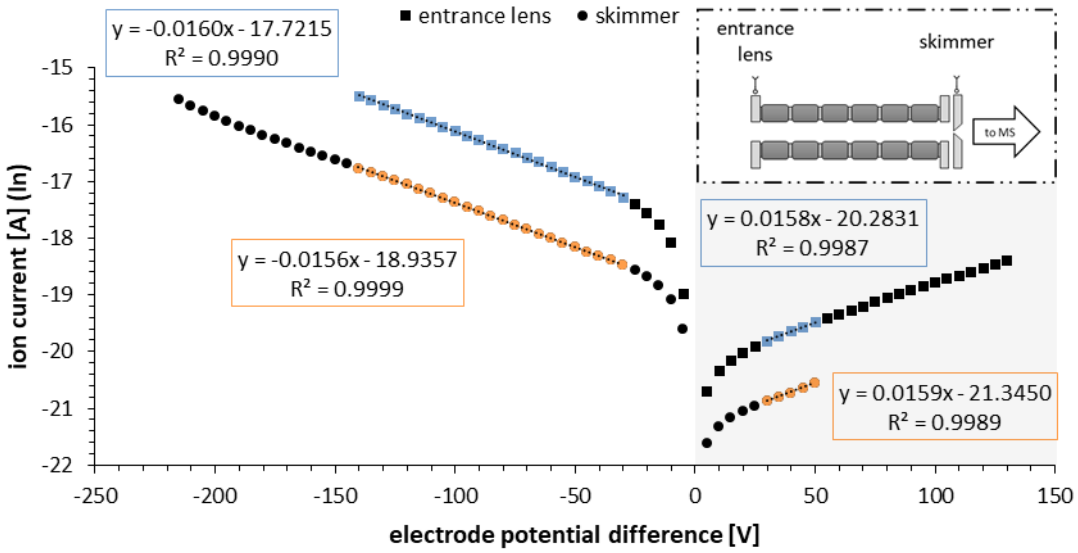

Figure 18: The logarithm of the ion current as a function of the potential difference for a measurement at the entrance lens and at the skimmer. *White background:* ion current caused by positively charged species. *Grey background:* ion current caused by negatively charged species.

effluent were measured and (ii) the same mechanism for this exponential behavior was involved. It implies that one or more of the interferences described in the introduction of this chapter may occur.

One mechanism that could explain this phenomenon is the Townsend discharge (electron avalanche theory [72]). The decisive factor according to this theory is the presence of free electrons. These can be formed, e.g., at an electrode or other surrounding surfaces via the photoelectric effect. A value to describe the occurrence of photoelectrons is the material dependent electron work function Φ, which is a measure for the minimum energy required to extract an electron from the surface of a solid. The energy of the incident photon must be equal to the sum of the metal's work function and the photoelectrons kinetic energy. For stainless steel, the work function can be found to be around 4.5 eV, which corresponds to a wavelength of the incident photons of < 275 nm [73]. Radiation in this wavelength range is conceivabley emitted from the utilized hydrogen plasma. Known photoemission lines are the Lyman series, in the range from 121 – 91 nm [74]. Due to the complexity of the instrumentational setup, the emission spectrum is this wavelength range could not be measured. However, the observed emission lines (cf. chapter 4.3) of the Balmer series and the broad continuum between 300 – 500 nm, assigned to the emission of the H_2 radiative dissociation continuum ($a^3\Sigma_g^+ \rightarrow b^3\Sigma_u^+$ electronic transition [75]), suggest that radiation in the critical range < 275 nm could be present. The observation of M^+ analyte signals also supports this hypothesis. Once

photoelectrons are created, they are accelerated in the electric field towards the anode. If the kinetic energy acquired by the electrons becomes sufficiently high to ionize the background gas through inelastic collisions, new electrons and positive ions are formed.
Since the migration velocity of electrons is larger than that of positive ions by two orders of magnitude, the additional generated new electrons may also acquire sufficient energy to produce further ionization to form a so-called electron avalanche. The current rises exponentially and will depend upon the energy gained by an electron in a mean free path and the distance available for the ionization avalanche development. The first Townsend coefficient α describes the success rate for accelerated electrons to collide and ionize the background gas. When the voltage is further increased, the created positive ions may collide with the cathode to knock out new electrons out of the electrode, so-called secondary electrons, and the current begins to rise even faster. The probability of such a successful event is represented by the second Townsend coefficient γ. The coefficient depends on the cathode material, the state of the surface, the type of the background gas and the reduced electric field. Typical values of γ in electric discharges are 0.01 to 0.1 [76].
As mentioned above, the first Townsend coefficient α describes the number of electron-ion pairs generated by collisions with the background gas per 1 cm. As might be expected from the analogy of cross-sections, the coefficient is a function of the pressure and the accelerating electric field. α can be calculated according to [20]:

$$\alpha = \frac{1}{\lambda_e} \cdot e^{-\frac{E_i}{E \cdot \lambda_e}} \tag{4}$$

where λ_e is the mean free path of an electron, $E \cdot \lambda_e$ is the kinetic energy gain in the electric field, and E_i is the ionization energy of the background gas.
The mean free path of an electron is inversely proportional to the pressure p. The voltage U equals the electric field times the gap distance d. Considering these correlations equation 4 can be written as [20]:

$$\alpha = A \cdot p \cdot e^{-\frac{B \cdot p \cdot d}{U}} \tag{5}$$

where A and B are determined experimentally [77] and found to be roughly constant over a range of voltages and pressures for any given gas [20].
Taking into account the current of primary electrons I_0 and the electron current due to the background gas ionization and secondary electron emission, the total current I is defined by [78]:

$$I = \frac{I_0 . e^{\alpha \cdot d}}{1 - \gamma(e^{\alpha \cdot d} - 1)} \tag{6}$$

In the investigation of a gas discharge phenomenon, the discharge is usually divided into two categories: the non-self-sustaining discharge and the self-sustaining discharge. As mentioned above, Figure 18 indicates an exponential correlation between the potential difference and the measured ion current. This is characteristic for the non-self-sustained discharge regime, where the electrons, for example emitted from the cathode by the photoelectric effect, obtain enough energy in the electric field to ionize the background gas, leading to an exponential electron avalanche. However, the probability for positive ions to liberate electrons from the cathode in order to further the avalanche independently of a primary current is still too low. Under these conditions, it can be safely assumed that the term $\gamma\left(e^{\alpha \cdot d} - 1\right)$ from equation 6 becomes approximate zero and thus the formula can be simplified to:

$$I = I_0 \cdot e^{\alpha \cdot d} \tag{7}$$

Using α from equation 5 and taking their natural logarithms leads to the following dependency:

$$\ln(I) = A \cdot p \cdot d \cdot e^{-\frac{B \cdot p \cdot d}{U}} + \ln(I_0) \tag{8}$$

For an electron avalanche, a basic requirement is that the kinetic energy gain of an electron in the electric field is high enough to overcome the ionization energy of the background gas. This means, that the exponential term has to become ≤ 1 according to equation 4. The latter is used as a starting point for a Taylor series approximation.

The exponential term in equation 8 is approximated with the Taylor series in U up to the first order, since a linear correlation is observed. The series is evaluated at the point $U = B \cdot d \cdot p$. This leads to the following approximation:

$$\ln(I) = \frac{A}{B \cdot e^1} \cdot U + \ln(I_0) \tag{9}$$

This equation could explain the observed linear relationship in Figure 18 between the logarithmic ion current I and the electrode potential difference U, where the term $A/(B \cdot e^1)$ corresponds to the slope of a linear regression. Since the parameter A and B are determined experimentally and can be found in the literature, the slope can be calculated for the different gases (cf. Table 1) in use.

Table 1: Parameters A and B, regions of applicability and the respectively calculated slopes according to equation 9.

Gas	A [cm^{-1} $Torr^{-1}$]	B [V cm^{-1} $Torr^{-1}$]	E p^{-1} [V cm^{-1} $Torr^{-1}$]	Calculated slope [V^{-1}]
H_2	4.8[a]	136[a]	15 – 600	0.0130
H_2	5[b]	130[b]	150 – 600	0.0142
N_2	11.8[a]	325[a]	100 – 600	0.0134
N_2	12[b]	342[b]	100 – 600	0.0129

[a] cf. ref. [20]; [b] cf. ref. [79]

A different representation of the linear regressions in Figure 18 by means of a *residuals vs. predictor plot* is exemplarily shown for the positive ion current on the skimmer electrode in Figure 19. It is obvious that a linear correlation does not apply over the entire measuring range. The straight black line shows the range of the linear regression over which the deviations from the predicted values were calculated. Equally spread residuals around a horizontal line at the residual = 0 line without distinct patterns indicate a good linear correlation.

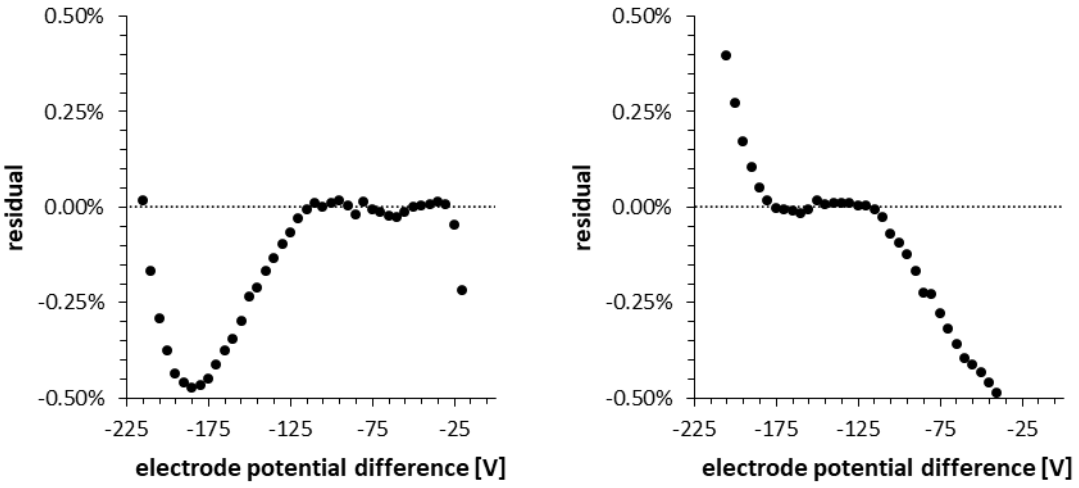

Figure 19: A "residuals vs. predictor plot" for a linear regression model of the measured positive ion current at the skimmer electrode. *Left:* Calculated residuals with the linear equation estimated in the range from -30.3 V to -105.3 V. *Right:* Calculated residuals with the linear equation estimated in the range from -110.3 V to -175.3 V.

The plots reveal approximately two different linear ranges, with a transition between them at a potential difference of about -105 to -110 V. To investigate this phenomenon, numerical simulations of the electric field between the skimmer and the lens skimmer electrode were carried out using SIMION [55].

As mentioned above, a basic requirement for initiating an electron avalanche is that the exponent from equation 8 is ≤ 1. With the help of the relationship $U = E \cdot d$, equation 9 results in:

$$\ln(I) = A \cdot p \cdot d \cdot e^{-\frac{B \cdot p}{E}} + \ln(I_0) \tag{10}$$

Thus, a critical E value can be calculated with the condition $(B \cdot p)/E_c = 1$. This value E_c describes the minimum electric field strength for an electron to acquire enough kinetic energy to ionize the background gas. With the parameter B from Table 1 and a given pressure of 6 mbar this value is determined to be 585 V cm^{-1} for hydrogen and 1462 V cm^{-1} for nitrogen.
The skimmer and the lens skimmer electrode geometry were implemented into a SIMION model and the electric field strengths for the applied voltages were calculated. The results are presented in Figure 20. The red lines indicate the critical value E_c for hydrogen and the blue lines the critical value E_c for nitrogen for different skimmer voltages.

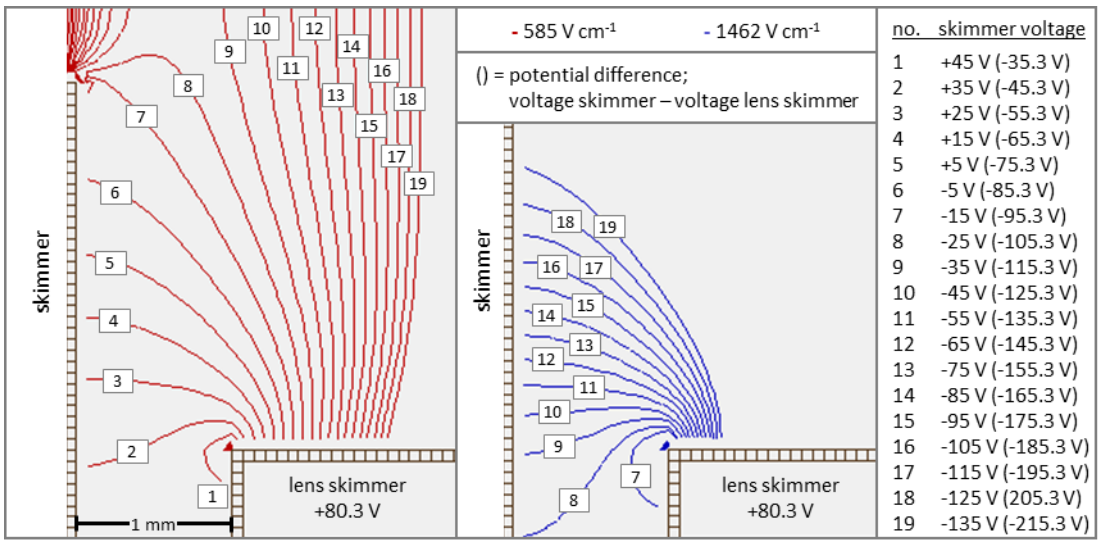

Figure 20: Numerical simulation with SIMION of the electric field strengths between the skimmer and the lens skimmer electrode (half cut, rotationally symmetric) for different skimmer voltages. The value in brackets *Left:* iso-electric field lines (red) for the E_c value of hydrogen. *Right*: iso-electric field lines (blue) for the E_c value of nitrogen.

For hydrogen a potential difference of merely -35.3 V (no. 1) is sufficient to initially cause the critical electric field strength around the lens skimmer edge. With increasing skimmer voltage, the area of feasible avalanches expands until it completely fills out the inside lens skimmer space.
The same applies for nitrogen, but the critical field strength is first attained at a potential difference of -95.3 V (no. 7). This could explain the transition to the second linear range in

Figure 19. In some areas the field strength might become large enough that even nitrogen molecules in the background gas can be ionized and start electron avalanches as well.
Another reasoning for the observed transition can be found in the significant spatial jump between the red E_c field lines no. 8 and no. 9, which exactly mark the experimentally observed transition region of -105.3 V to – 115.3 V in Figure 19, respectively. At this point the critical electric field strength lines for hydrogen start to extend over the entire lens skimmer, instead of just being confined between the lens skimmer and the skimmer electrode. This forms a more homogeneous electric field and the experimentally determined parameters A and B are, strictly speaking, only valid for homogeneous electric fields.
The estimated slopes for the respective linear regressions can be found in Table 2. Since during the electron avalanche process the number of generated positive ions is equal to the produced additional electrons, the slopes for the measurement of a positive or a negative ion current on the skimmer should be roughly the same. This holds true for the ion current measurements at the skimmer (cf. Table 2).

Table 2: Estimated slopes for the respective potential difference ranges and the corresponding I_0 values.

Potential difference section [V]	Slope [V^{-1}]	Correlation coefficient
Entrance lens:		
-65 to -95	-0.0157 ± 0.0004	1.0000
-100 to -140	-0.0152 ± 0.0004	1.0000
50 to 75	0.0146 ± 0.0003	0.9999
80 to 130	0.0132 ± 0.0003	1.0000
Skimmer:		
-30.3 to -105.3	-0.0158 ± 0.0004	0.9999
-110.3 to -175.3	-0.0146 ± 0.0003	1.0000
29.7 to 49.7	0.0159 ± 0.0004	0.9989

The phenomenon of the transition between two linear ranges does not only occur with the ion current measurements at the skimmer electrode, but also with the current data at the entrance lens. Given that some parameters, e.g. the distance of the glass tube to the entrance lens, cannot be determined with sufficient accuracy, no additional SIMION simulations for this part of the ion transfer were made. But since the measurements show similar trends, it can be expected that the same mechanisms are involved as discussed with the investigation at the skimmer.
As seen in Table 2 the occurrence of the linear range at the entrance lens starts at a higher potential difference compared to the ion current measurements at the skimmer. The distance

between the glass tube and the entrance lens is in the range of 1 - 3 mm. Since the electric field strength is a function of the gap distance between the two electrodes, a larger distance requires a higher potential difference to reach the critical field strength values.
Furthermore, as mentioned above and as the results suggest, the inner surface of the glass tube can become electrically charged. Given that glass is an insulator and the surface potential is floating, the applied deflection voltage at the entrance lens could lead to a shift of this potential.

Despite the interfacing avalanches caused by a non-self-sustaining discharge regime, a primary ion current I_0 can still be derived from the respective intercepts of the linear fits of the ion current data according to equation 9. Following the theory and the assumptions made above, I_0 is the ion current before the kinetic energy acquired by the electrons becomes sufficiently high to ionize the background gas. Thus, I_0 should correspond to the primary ion current without secondary ionization processes. The determined I_0 values of the respective first linear ranges in the ion current data are listed in Table 3. Even though these values do not mark an absolute ion current, some conclusions can still be drawn, e.g. under the assumption that in both ion current measurements, at the entrance lens and at the skimmer, respectively, the same mechanisms are involved.

Table 3: Determined ion currents of the corresponding potential difference ranges.

Potential difference section [V]	**I_0 [A]**	**Polarity of measured ions**
Entrance lens:		
-65 to -95	$(2.09 \pm 0.01)\ 10^{-8}$	+
50 to 75	$(1.65 \pm 0.01)\ 10^{-9}$	-
Skimmer:		
-30.3 to -105.3	$(5.99 \pm 0.01)\ 10^{-9}$	+
29.7 to 49.7	$(5.37 \pm 0.07)\ 10^{-10}$	-

A positive potential difference would retain the photoelectrons due to Coulomb attraction and only a negative potential difference would cause the ejection of photoelectrons from the electrode. This would add the resulting photocurrent as a constant offset to the measured positive ion current. Since the hydrogen plasma is ignited in a glass tube with a diameter that is much smaller than the distance to the points of ion current measurement, the plasma can be considered as a point source of light. Thus the intensity of the light hitting the measurement electrode is inversely proportional to the square of the distance from the light source. Taking into account the different sizes of the irradiated electrode surfaces, the photon flux on the

skimmer is only 13 % of the photon flux on the entrance lens, when photon absorption by the matrix gas is not considered. Comparing the measured positive ion currents on the entrance lens and the skimmer the transmission efficiency is about 29 %.
The measured negative ion current is an order of magnitude smaller at both measuring points. Assuming that this current is generated purely by free photoelectrons, their contribution to the total current is very small and it can therefore be assumed that the measured ion currents are at least not caused exclusively by photoelectrons.
Furthermore, the obtained positive ion current measured at the entrance lens is in the expected order of magnitude when extrapolating the received data of the previous measurements on the ion current recipient, excluding photoelectron effects (cf. chapter 4.2.1, Figure 15).

The results of the ion trajectory simulations discussed in detail in chapter 4.8.2 show a transfer efficiency of the SSQ of about 22-23 % for the N_2H^+ ion and the $[M+H]^+$ analyte ion of *o*-xylene, which is very close to ion transfer efficiency determined by the measured ion currents. The simulations consider only the gas flows and no space charge effects. The latter may not be negligible and can potentially lead to additional ion loss. Assuming that all ions reaching the skimmer have previously passed through the entrance lens allows a conservative estimation of the ion density at the entrance lens. With the calculated gas velocity of 1-1.5 m s^{-1} (cf. chapter 4.8.1, Figure 67) and the ion current measured on the skimmer, an ion density of 4 - 6·10^{12} cm^{-3} is determined.
Another ion current measurement point was at the BSQ in the next differentially pumped transfer stage directly after the skimmer. Using the same method as described before, an ion current of about (1.85 ± 0.06)·10^{-9} A was determined. A comparison of the determined I_0 values and the resulting transfer efficiencies is summarized in Table 4.

Table 4: Determined ion currents at different points in the ion transfer stage and estimated transfer efficiency.

Ion transfer position	Ion current [A]	Relative transfer efficiency [%]
Entrance lens	(2.09 ± 0.01)·10^{-8}	
		~ 29
Skimmer	(5.99 ± 0.01)·10^{-9}	
		~ 34
BSQ	(1.85 ± 0.06)·10^{-9}	
		Total: ~ 9

In summary, the theoretical and experimental correlation between the measured current and the applied voltages (cf. slopes in Table 1 and Table 2) support the hypothesis of an initiated non-self-sustaining Townsend discharge in the two investigated regions of the TOF-MS. Nevertheless, a primary ion current I_0 could be determined that is within the expected range. Interferences by photoelectrons cannot be completely excluded, but these processes probably play only a minor role concerning the total ion current. Although these values may do not represent an absolute ion current value, an estimation by comparing these values yields a transfer efficiency of the entire SSQ and CI source assembly into the subsequent differentially pumped stage of about 9%.

4.3 Optical Emission of the Hydrogen Plasma

Generally, a simple and meaningful way to investigate the condition and the dynamics of a plasma is by means of its optical emission. For the characterization of the helical resonator plasma the ultraviolet (UV) to visible (VIS) spectral range was examined. Figure 21 depicts the UV/VIS emission spectrum of the hydrogen plasma region obtained with the ion source version 3. The spectrometers optical fiber adaptor was radially positioned on the plasma tube, 5 mm downstream from the helical resonator shielded. The ion source was operated under usual conditions in connection with the TOF MS. The plasma itself was fed by 50 sccm hydrogen (7.0), 6 sccm nitrogen (5.0) were used as reagent gas and the GC effluent accounted for 2 sccm Helium (< 7.0). The pressure inside the SSQ chamber was maintained at 6.1 mbar. The spectrometer was first calibrated based on the emission lines of a mercury-vapor lamp and frequently readjusted by means of the known H spectral lines (H_α, H_β, H_γ).

Characteristic for the spectrum is the dominant, broad continuum between 300 –500 nm, assigned to the emission of the H_2 radiative dissociation continuum ($a^3\Sigma_g^+ \rightarrow b^3\Sigma_u^+$ electronic transition). Note, that the representation of the lower wavelengths is limited by a sharp decrease of the UV transmission efficiency of the used plasma tube. For example, at 330 nm the transmission is < 58 % (at 1 mm thickness) [63]. Furthermore, the spectrometer and the optical fiber are not corrected for wavelength dependent response. Therefore, it can be assumed, that the observed continuum extends to the far UV range.

The main line emission in the spectrum is part of the Balmer series and corresponds to the first hydrogen line H_α (656.28 nm [80]). Two further lines of this series were identified as the H_β (486.14 nm [80]) and the H_γ line (434.05 [80]). In addition to the atomic transitions of hydrogen also band spectra of the molecular system are observed. Their annotation closely follows the related Balmer line representation with α, β and γ-bands, respectively [81, 82]. The

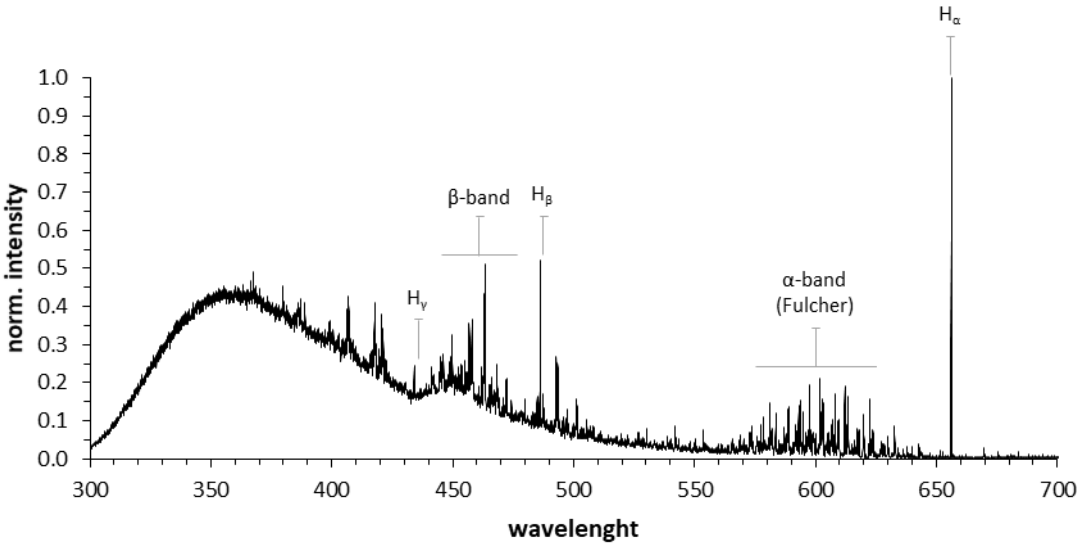

Figure 21: Emission spectrum of the hydrogen plasma with the ion source Design 3 at the TOF MS.

multiline spectrum around 601.83 nm is assigned to the α-band Q-branch (Fulcher spectrum). Due to the small masses involved, the Fulcher spectrum appears as a multiline spectrum and the vibrational bands and rotational lines frequently overlap. However, some transitions of the P and R branch were identified. In the region around 449.17 nm lines of the Q-branch and of the β-band are observed [81, 82]. Other multiline spectra appear from the continuum at wavelength < H_γ, which are assumed to belong to the molecular hydrogen (cf. ref. [83]).
No characteristic emission other than that from hydrogen was found in the spectrum. In particular none that refers to nitrogen (e.g. 2nd positive system 300 – 440 nm). This clearly indicates that (i) the used hydrogen is of sufficient purity, (ii) the ion source is well sealed and (iii) for the given operating conditions, there is no significant back-diffusion into the plasma region either of the further downstream added reagent gas nor the GC carrier gas.

Since the H_α-line (656.28 nm [80]) dominates the emission spectrum, its intensity further served as an indicator for more detailed studies on the plasma dependency with regard to gas pressure and the driving RF-frequency. Figure 22 reveals similar trends for pressures between 0.3 mbar and 6.0 mbar, with a distinct maximum at a frequency of 12.05 MHz. This closely corresponds to the theoretical helical resonance of 12.08 MHz, calculated with the present coil geometry (wire length, coil diameter, number of turns) according to a quarter-wave resonator as described in chapter 1.2.1.

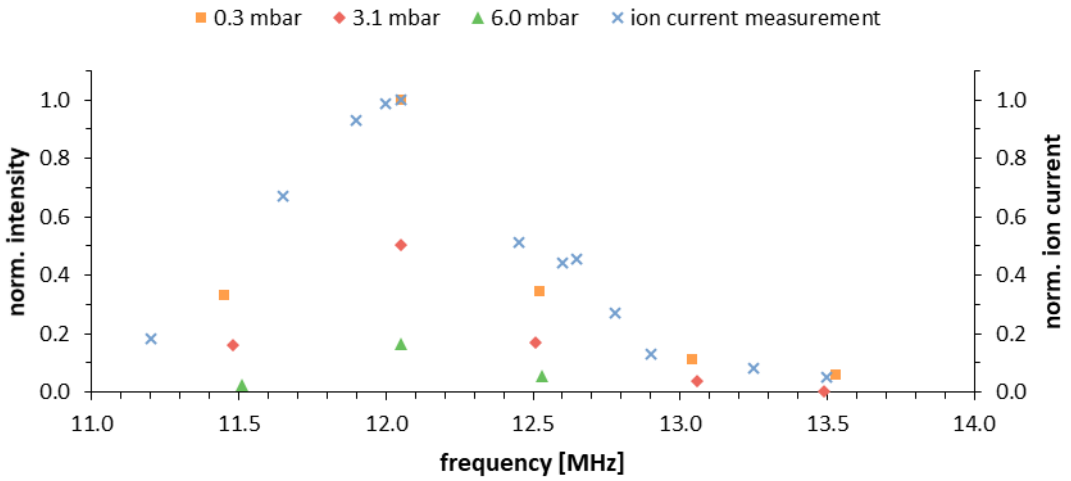

Figure 22: H_α spectral line intensity (656.28 nm) (left vertical axis) and normalized positive ion current (right vertical axis) at 3.5 mbar as function of the frequency.

In addition, the pressure dependency clearly shows an inverse proportionality with the emission intensity. A twentyfold decrease of the gas density causes a radiative increase by a factor 10. It can readily be assumed that at lower pressure the electron temperature in the plasma increases, which causes more hydrogen to be present in a dissociated and electronically excited state [84, 85].

Figure 22 also shows a good correlation between the measured ion current (setup cf. chapter 3.8.1) and the H_α spectral line intensity about the RF-frequency. Consequently, the positive charge density and the light emission develop a maximum at 12.05 MHz. This helpful correlation can readily be used to further optimize the helical resonator plasma source, e.g. using automatic control. As described in chapter 3.6, the circuit board is equipped with a potentiometer to adjust the operating frequency manually. In nearer future, an electronic circuit with a simple photodiode will be developed that automatically regulates the potentiometer and constantly operates the plasma at its radiative maximum, which is also equivalent to a peaking ion yield.

4.4 Ion Source Iteration

In the following chapter, each step of the iterative ion source development is discussed in detail. The continuous progress is be described based on the individual designs and the obtained results.

Although the development of a chemical ionization source for GC-MS applications was the main aim of this work, at the beginning of the development process it was intended that an

application in real time process monitoring should remain feasible without major modifications on the ion source. However, as the development process progressed, the focus on GC-MS applications became more important.

4.4.1 Design 1

In 2020, D. Müller [64] developed a chemical ionization assembly within his PhD work, which was tailored to a particular set of conditions for process monitoring. This *µ-plici 2.2* source was designed to best possibly reflect the neutral molecule distribution from a complex gas sample. With the approach to kinetically control ion-molecule reactions, interfering transformation processes of the initial ion distribution were shown to be significantly reduced. The unique stacked chamber concept offered flexible design capabilities and therefore provided a suitable basis for innovative adaptions to the present MS system. The interchangeable orifices separated the reaction cascade for ion-reagent generation into different chambers, enabling the optimization of each reaction step individually. In this way the chemistry of the plasma effluent was quantitatively driven to a well-defined reagent species, which allowed precise control of the analyte ionization conditions. For more details see ref. [64]. Despite the profound difference in application – process monitoring versus the focus on GC-MS in this work – the µ-plici 2.2 provided the starting point for the development of Design 1, due to its unique capabilities.

Therefore, in the first setup of this work the helical resonator replaced the original DC plasma on the µ-plici 2.2 as shown in Figure 7 in chapter 3.9.1. In particular the overall operating pressure and the pressure drop along the entire assembly dramatically changed. In contrast to the original DC plasma pressure of 100 – 1700 mbar - depending on the helium flow (up to 100 sccm) - the helical resonator operated with hydrogen in the regime of merely 0.1 to 10 mbar. In addition, the short-segmented quadrupole, following the stacked chamber system, showed optimum ion transfer efficiency at 2 mbar. This comparable small pressure difference along the entire assembly, in combination with the original aperture dimension of the stacked chamber, posed some challenges. Foremost, completely different gas flow conditions evolved, and with it the reaction cascade concept of the original µ-plici 2.2 had to be rethought. The flow converts from a choked continuous flow to a slip flow in transitional Knudsen flow. To maintain the necessary plasma pressure with the original tantalum aperture of 100 µm inner diameter, the hydrogen flow through the helical resonator was limited to 1 sccm. Each additional reaction chamber significantly affected the upstream plasma pressure. Compared to other gases, hydrogen has a relatively low viscosity. If a reagent gas (e.g. nitrogen) was introduced

to the first chamber, the total viscosity of the gas mixture increased. The change in viscosity in turn impacted the flow rate through the aperture and thus the pressure in each compartment. Since all chambers in the stack are gas dynamically coupled, also the plasma pressure was very sensitive to downstream fluctuations. However, for proper operation the helical resonator required a virtually constant pressure between 0.1 to 10 mbar. This means that the addition of reagent gases and analytes further downstream must not affect the total pressure gradient from maximum 10 mbar in the plasma region to 2 mbar in the SSQ chamber. First measurements showed, that even wider apertures with up to 200 µm inner diameter for the first compartment did not allow a higher gas throughput. This restriction to low gas velocities prevented the optimal mixing ratio between the primary charge carrier containing plasma effluent and the reagent gas. It also caused tremendously long dwell times within the plasma gas chamber and lead to considerable ion losses on the surfaces, due to the absence of ion focusing electrical fields. In consideration of these complex gas and reaction dynamics, the original µ-plici 2.2 setup had to be carefully modified for appropriate adaption in this work.

In the following, the performance of Design 1 will be presented with three slightly different modifications in terms of aperture dimensions and points of gas supply (cf. Figure 23). For comparison, the same benzene, toluene and *o*-xylene (BTX) mixture in nitrogen (#4, Table 16, appendix) was used for each modification.

Modification #1

The ion source Design 1 with the stacked chamber assembly (modification #1, Figure 23) similar to the configuration of the DC plasma µ-plici 2.2 source developed in the work by D. Müller [64]. In this first modification, however, the aperture between the plasma chamber and the 1st reagent gas compartment was removed, thus no restriction prevailed for the supplied 1 sccm H_2 flow between these two regions. Additionally, the feedthrough to the 1st reagent gas chamber was used to monitor the pressure of the plasma region. A subsequent aperture of 100 µm inner diameter separated the 1st from the 2nd reagent gas chamber, the latter being used for the BTX-mixture supply of 100 sccm. This flow, in combination with the upstream hydrogen addition of 1 sccm, established a pressure of 8.1 mbar in the plasma region. Finally, the original flow restriction between the 2nd chamber and the SSQ was removed as well, in order to maintain optimal pressure conditions of 2.1 mbar for the ion transfer in the SSQ. In this way, the entire gas flow of 101 sccm entered the SSQ axially. The pressure inside the 2nd

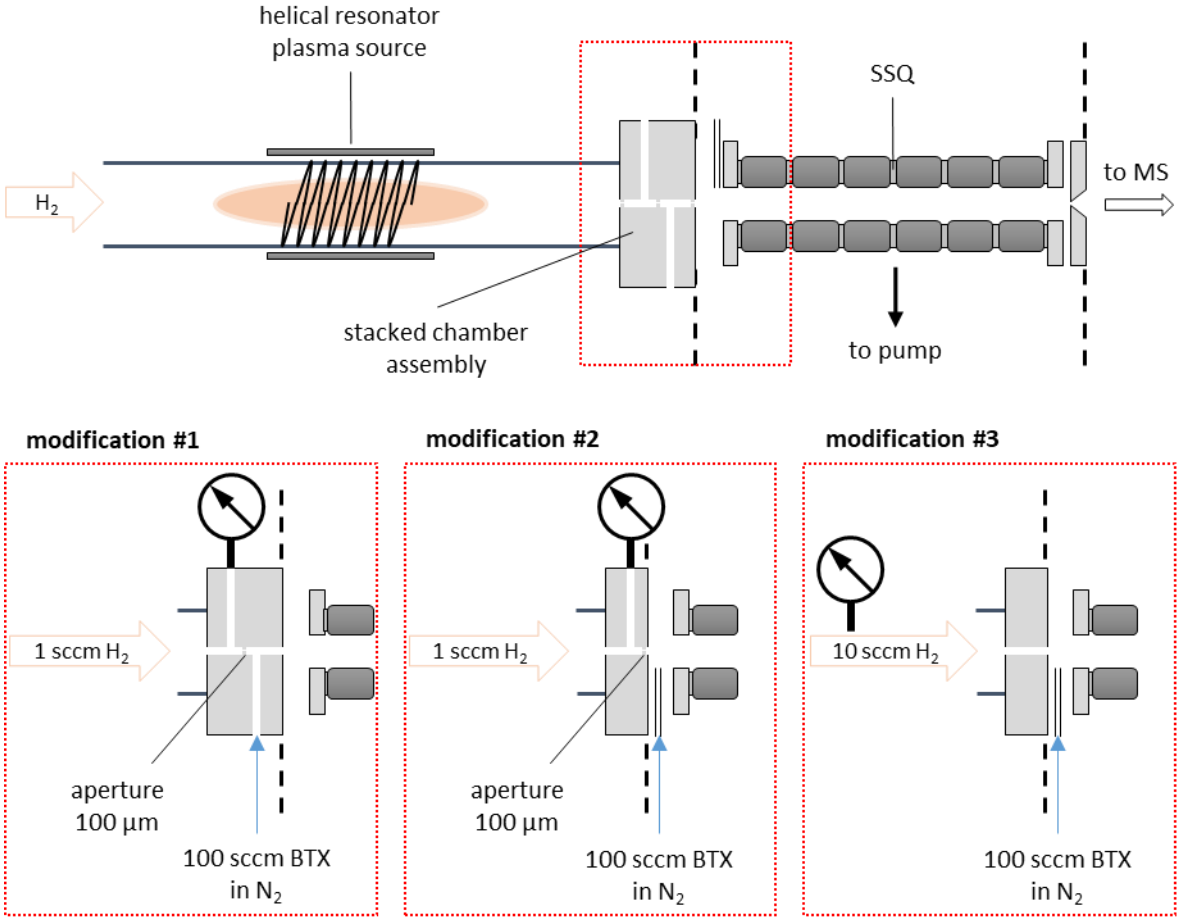

Figure 23: Schematic drawing of the ion source Design 1 and a more detailed view of the three modifications.

reaction chamber was not directly measured but considering the gradient between the plasma region and the SSQ chamber and taking into account the channel dimensions a rough estimate of 4 mbar seemed reasonable. This translates to approximately 26 µs dwell time for the BTX mixture in a collisional dominated region of the mass spectrometer.

In this modification, the first three water species - H_3O^+ to $[(H_2O)_3H]^+$ - essentially dominate the recorded mass spectrum in Figure 24. It should be reminded that the hydrogen gas contained < 5 ppmV water according to the manufacturer's specifications and was used without further purification. With increasing size, this water system becomes a thermodynamic “sink” for protons. As can be seen from Table 7 in chapter 4.6, the proton affinity significantly increases with increasing cluster size, which translates to gradually decreasing reactivity. While H_3O^+ is still an appreciable gas-phase acid for a fairly large range of analytes, one finds a proton affinity of as high as 808.0 kJ mol^{-1} for $[(H_2O)_2H]^+$, which noticeably limits the amenable range of analytes for chemical ionization. The same applies to the observed NH_4^+ ion with a proton

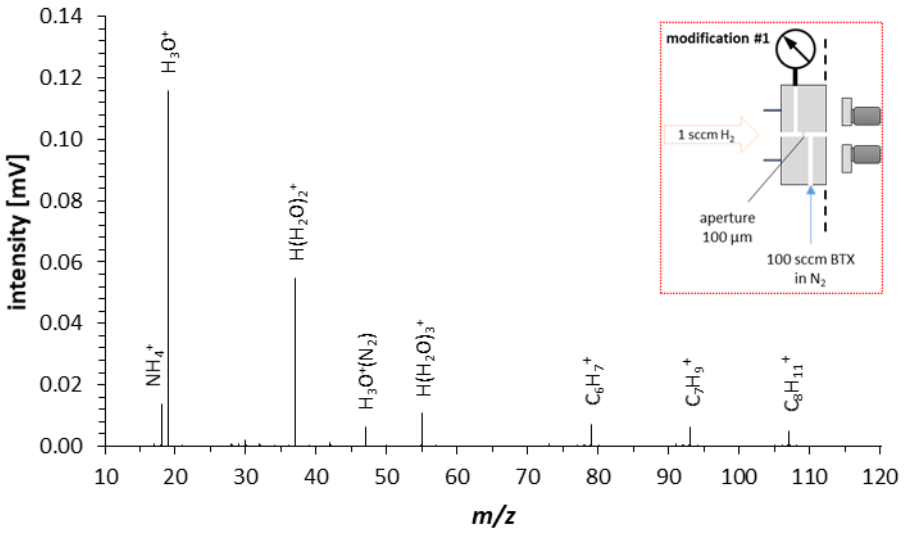

Figure 24: Mass spectrum obtained with chemical ionization source Design 1 (modification #1) with the following configuration. *Plasma chamber:* aperture 100 µm, 1 sccm H_2, 8.1 mbar. *Second reagent gas chamber:* 100 sccm BTX mixture in N_2 (cf. Table 16, #4, appendix) without aperture. *SSQ chamber:* 2.1 mbar.

affinity of 853.6 kJ mol^{-1}. For the design of a rather unselective CI source, particular care should be taken to minimize the formation of these species.

Interestingly, Figure 24 does not show any signal of the expected N_2H^+ species despite the fact that nitrogen constitutes the main part of the total gas flow. This again can readily be explained by the high proton affinity of water, which substantially exceeds that of nitrogen by 166 kJ mol^{-1}. From a kinetic point of view, this spectrum thus demonstrates the extensive consecutive reactions that N_2H^+ was subjected to in this first modification of Design 1. The entire population of N_2H^+ rapidly lost its protons to the background water within these approximated 26 µs dwell time before entering the collision-free region of the mass spectrometer.

Figure 24 also shows that the analytes benzene, toluene and xylene predominantly appear in their protonated form $[M+H]^+$. In this regard, toluene turned out to be a quite useful indicator for the "hardness" of the ionization process. This term expresses a rather qualitative observation of the degree of fragmentation caused by the proton transfer from the reagent to the analyte. In general, the larger the difference of proton affinities between reagent and analyte, the more excess energy is released and the degree of fragmentation increases. In case of toluene, only the low proton affinity of H_3^+ can cause it to fragment into the well-known stable tropylium cation ($C_7H_7^+$) with a branching ratio of 20 % [50]. All other possible reagents (N_2H^+, H_3O^+, etc.), however, form the intact protonated toluene molecule to 100 % [50].

Consequently, the fragmentation ratio of toluene indicates the proportion of H_3^+ still acting on the analytes in the 2nd reaction chamber. In this configuration, toluene showed about 10 % fragmentation. To a lesser extend also the subsequent reaction of $C_7H_9^+$ with residual neutral toluene might have contributed to the $C_7H_7^+$ signal [50]. In addition, high-energy photons entering the 2nd compartment could have as well slightly impacted on the fragmentation chemistry.

As stated before, the water cluster system forms a proton "sink" and reduces the overall sensitivity of the system. To suppress the formation of the cluster system, the reaction time needed to be reduced. Therefore, in the next modification of Design 1 the second reaction chamber was completely removed and the BTX-mixture was directly introduced into the SSQ chamber, between the entrance lens and the plasma chamber aperture. This allowed to reduce the pressure in the plasma region, resulting in a significantly shorter dwell and reaction time. In other words, less collisions between the reagent ion containing plasma effluent and the neutral analyte containing gas flow.

Modification #2

The marked difference of the second modification is caused by basically two slight changes. (i) The 2nd reagent gas chamber was removed and only the 100 µm aperture at the end of the 1st chamber restricted the flow from the plasma region into the SSQ chamber. (ii) The BTX mixture was introduced through a capillary further downstream, immediately behind the aperture and before the entrance lens of the SSQ.
Figure 25 shows a mass spectrum recorded with the second modification of Design 1, however, with the exact same gas composition and flows as used for the spectrum in Figure 24.
This rebuild brought about a notably different ion distribution. In contrast to the mass spectrum in Figure 24, the protonated nitrogen molecule N_2H^+ appeared, even as the main signal. The previously dominant water cluster system could be largely suppressed, despite the same neutral water content in the supplied gases. Merely H_3O^+ was still present. Interestingly, also the proton-bound nitrogen cluster N_4H^+ was observed. Its presence is attributed to the reaction of N_2H^+ with excess molecular nitrogen [86] and it forms a reservoir for the reagent ion N_2H^+. The analytes benzene, toluene and xylene mainly appeared as the protonated species $[M+H]^+$, alike in modification #1. The fragmentation ratio of toluene is slightly increased to about 13 % with this concept.
The differences in the observed ion chemistry between modification #1 and #2 need to be discussed from a kinetical perspective. Removing the 2nd reagent gas chamber and introducing

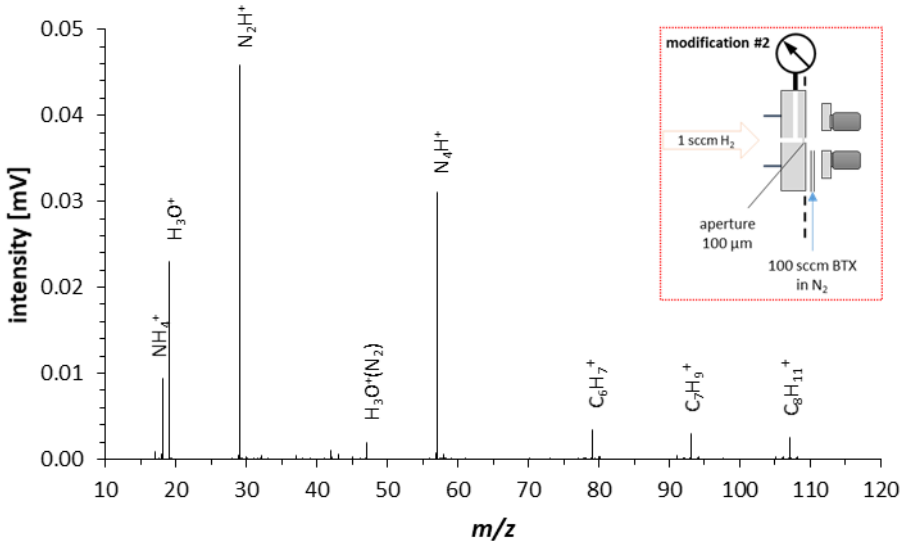

Figure 25: Mass spectrum obtained with chemical ionization source Design 1 (modification #2) with the following configuration. *Plasma chamber:* aperture 100 µm, 1 sccm H_2, 4.3 mbar. *SSQ chamber:* 100 sccm BTX mixture in N_2 (cf. Table 16, #4, appendix). 2.1 mbar.

the main gas flow (BTX mixture) directly into the SSQ chamber altered the gas kinetic conditions as follows: Firstly, the pressure inside the plasma region dropped by nearly one half to 4.3 mbar, whereas the pressure inside the SSQ was constantly kept at its transfer optimum of 2.1 mbar. Consequently, with the same plasma gas flow, also the residence time for the primary ions in the plasma region dropped by a factor of two and the number of collisions for a single ion reduced by a factor of four (determined by simple kinetic gas theory). This might explain the lesser extent of the water-cluster system as compared to modification #1.
Secondly, the time for the BTX mixture to react with the plasma effluent was significantly reduced to approximately 9 µs compared to the 21 µs in modification #1. This was directly reflected by the analyte signal intensity, which was nearly a factor of 2.3 lower as well.

Modification #3

The third modification of Design 1 essentially aimed at an increased primary reagent ion current. Here all apertures between plasma and SSQ were removed and the passage enlarged to a 5.5 mm long and 1.5 mm wide channel. This enabled to increase the hydrogen gas flow by a factor of ten to 10 sccm without significant increase of the plasma pressure. The BTX-mixture was added to the system right in front of the entrance lens in the same way as in modification #2. Also, the flow of 100 sccm was identical. Again, the pressure inside the SSQ

chamber was maintained for optimal transfer conditions at 2.1 mbar, which, in total, established a plasma pressure of 2.2 mbar.

Figure 26 shows the mass spectrum of the third modification of Design 1. The most impressive aspect of this mass spectrum is the tremendous increase of the total ion current by more than three orders of magnitude as compared to the previous two modifications.
The ion signal distribution, however, is similar to the spectrum obtained with modification #2. N_2H^+ contributes the main signal and from the water cluster system only H_3O^+ is observed. Again, the proton-bound nitrogen cluster N_4H^+ is present, however, to a lesser extent relative to the N_2H^+. The NH_4^+ ion and the $H_3O^+(N_2)$ cluster signals are absent in this setup. The analytes benzene, toluene and xylene are still observed mainly in their protonated form but the fragmentation ratio of toluene increased to about 27 %.

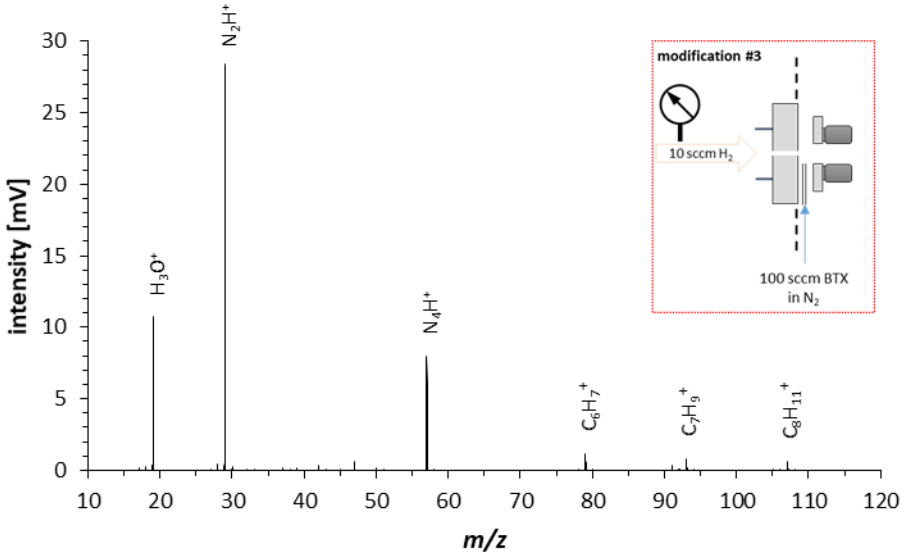

Figure 26: Mass spectrum obtained with chemical ionization source Design 1 (modification 3) with the following configuration. *Plasma chamber:* without aperture, 1.5 mm diameter, 10 sccm H_2, 2.2 mbar. *SSQ chamber:* 100 sccm BTX mixture in N_2 (cf. Table 16, #4). 2.10 mbar.

Both, the considerably increased hydrogen gas flow and the pressure decrease in the plasma region contributed to an enormous reduction of the residence time (by a factor of 40) inside the plasma source. Consequently, it is reasonable to assume that the charge loss, e.g. on the surfaces, was much smaller as compared to modifications #1 and #2 (cf chapter 4.2.1). The massive primary reagent ion current also caused the protonated analyte signal intensities to increase by a factor of 700 with an increased S/N ratio of about 100 as compared to the previous two modifications. The higher fragmentation ratio of toluene indicates that plasma

afterglow species (e.g. photons) or a significant portion of H_3^+ was not intercepted by the reagent gas and directly reacts with the analyte instead.
It can also be observed that the analytes absolute M^+ signals increase considerably by a factor of about 200-300. This indicates that these molecular analyte ions are generated via photoionization from the hydrogen plasma emitted VUV photons. By removing the aperture between the plasma chamber and the SSQ chamber, the illuminated area by the plasma increases by a factor of 225. However, the proportion of the M^+ signals relative to the total analyte signal decreases within each modification step from 6 % in modification #1 to 4 % in modification #3.

The results of the presented three modifications of Design 1 support the assumption that a considerable part of the primary charge is lost through the restriction between the plasma chamber and the SSQ chamber, e.g. due to charge loss on the surfaces. To further investigate this effect, the restriction between the plasma region and the SSQ chamber was gradually enlarged from 1.5 mm up to 10 mm matching the inner diameter of the plasma tube. For quantification the total ion current is compared. The gas flow through the plasma and the pressure inside the SSQ chamber were kept constant and the chamber was additionally purged with a continuous flow of synthetic air. Figure 27 depicts the total ion current as a function of the flow restricting diameter. The experimental data are well represented by a logarithmic fit. Note that with the largest diameter an increase of the total ion current by a tremendous factor of 240 with a signal-to-noise increase of 120 was observed.

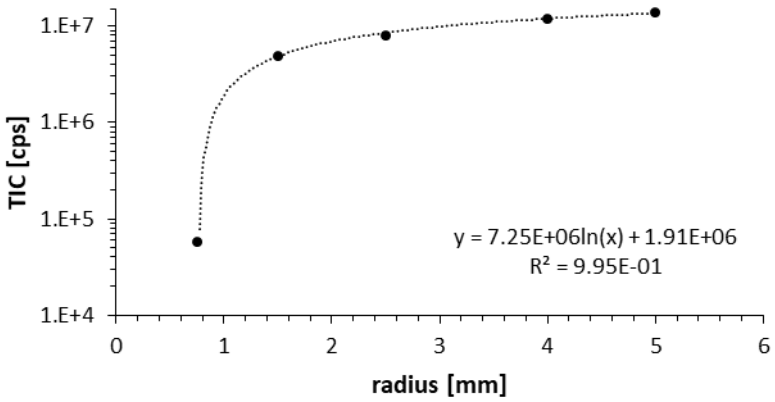

Figure 27: TIC as a function of the radius of the restriction between the plasma region and the SSQ chamber.

The comparison of these modifications of Design 1 underlined the importance for a careful and thought out concept for a chemical ionization source with a well-balanced system between intensity and kinetic control. In particular modification #3 impressively demonstrated how sensitive such a system responds to slight variations in construction. All these results formed the starting point for the next ion source Design 2.

4.4.2 Design 2

The chromatographic separation in GC-MS ideally provides the elution of time resolved neat compound “clouds” of Gaussian concentration profile into the ion source. The usual carrier gas is purified helium or hydrogen, which keeps the matrix rather simple. In contrast to monitoring applications with complex mixtures, these pure “clouds” are not affected by competition with other compounds for the limited primary charge, which makes a source design uncritical to any kinetic control as compared to Design 1. Consequently, for an appreciable analyte ion yield the reaction time between the primary charge and the neutral analyte plume can be greatly extended. However, care should be taken in the source design regarding (i) the spatial extension of this cloud in order to maintain the chromatographic time resolution, (ii) wall losses of neutral as well as charged analyte molecules and (iii) a well-defined primary reagent ion population to keep control over the chemical ionization step. Therefore, the layout of the second ion source design considered an enhanced overlap of the neutral analyte plume with the reagent gas ions and an increase of the reaction time.

As shown in Figure 8 in chapter 3.9.2 the overall gas flow, which included the plasma gas, reagent gas and the analyte containing bulk gas, was guided through a continuous glass tube downstream to the skimmer. This enclosed pathway strongly confined the spatial distribution of neutral analyte into the SSQ chamber of the TOF instrument. In addition, a quadrupolar field was established on the last section of the glass tube with electrodes directly attached to its surface. In this way ion losses by diffusion to the tube surface should be minimized and the overlap with the laminar gas flow containing neutral analyte should be maximized by the circular motion of the reagent gas ions in the quadrupole field. The analyte containing bulk gas was directly introduced in front of the quadrupole. The aim was to inject the neutral analyte directly into the region where the quadrupole field gradually focuses the reagent gas ions on the center axis. This again follows the approach of maximizing the overlap with the neutral analyte density. Moreover, the analyte was injected through the capillary's small inner diameter into a very small locally well-defined area close to the quadrupole to minimize the

diffusional distribution of the neutral analyte. An additional reagent gas could be added by another inlet further upstream. This setup should have provided similar advantages like the stacked chamber system discussed in the previous ion source design, but without the stated ions losses due to any restrictions or orifices.
For the characterization and swift optimization of the respective ion source parameters a continuous analyte sampling method was used instead of discontinuous GC runs. This provided better handling and also an evaluation of optional monitoring operation.

Figure 28 depicts a mass spectrum obtained with the ion source Design 2 and a continuous sampling of 100 sccm of a benzene, toluene and *o*-xylene mixture of approximately 11 ppmV. It should be noted, that the benzene content was about two-third less, as later quantified by calibrated GC-MS (cf. Table 16, #1, appendix). As described previously, the analytes were introduced directly in front of the quadrupole, and, in this case, without the addition of any further reagent gas through the upstream inlet. Instead, the main component of the analyte mixture was nitrogen, which at first clearly dominates the ion transformation cascade to eventually form the main reagent ion species.

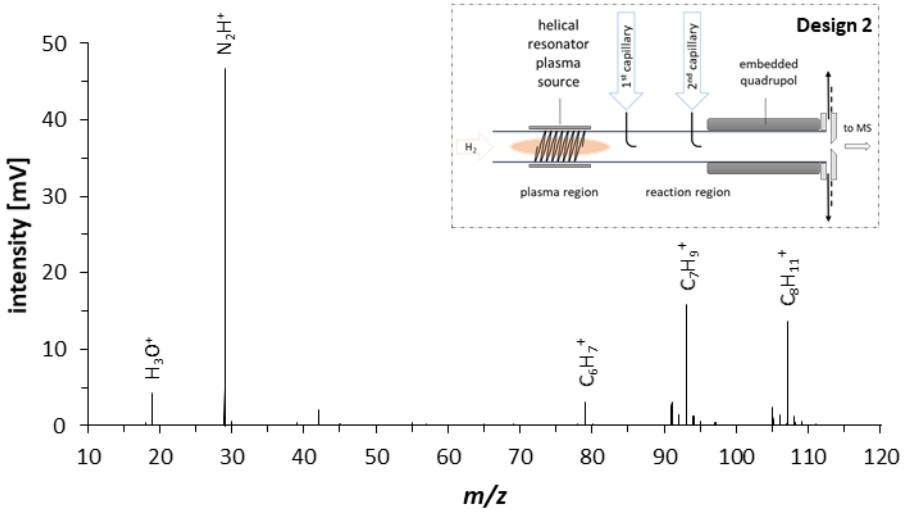

Figure 28: Mass spectrum obtained with the chemical ionization source Design 2. 30 sccm H_2 plasma gas flow, 100 sccm BTX-mixture in N_2 (cf. Table 16, #1, appendix) at 3.3 mbar.

Accordingly, N_2H^+ was the most abundant background ion, however, also some H_3O^+ was observed. Benzene, toluene and *o*-xylene mainly appeared as the protonated molecular ion $[M+H]^+$. In addition, toluene and *o*-xylene also showed significant amounts of the tropylium ($C_7H_8^+$) and the methyl- tropylium ($C_8H_9^+$) fragments with nearly 14 to 15 % relative to the

$[M+H]^+$. This result suggests that the analyte may, at least partly, be ionized via the direct reaction with H_3^+ or due to back diffusion into the plasma region.
Various attempts were made to minimize a potential back diffusion into the plasma region. Since this diffusion depends on the cross-sectional area, glass tubes were customized with different nozzle geometries and diameters, to separate the plasma region. However, with all setups similar results to the stacked chamber system were obtained. Any restriction between the plasma region and the ionization region lead to considerable primary ion loss and thus to a reduced sensitivity.
Regarding the quadrupole section on the glass tube, measurements with this setup showed, that the ion signals are nearly unaffected by the field frequency and amplitude. The variation in the total ion current with and without applied RF frequency was lower than 5 % without any effects on the ion distribution. Apparently, space charge effects occur due to the high plasma current and shield the RF field. Consequently, the concept of the embedded quadrupole was not further pursued and for the next ion source iteration the short segmented quadrupole was reinstalled.

4.4.3 Design 3

The third ion source design explicitly focused on GC-MS application, which required careful attention to a multitude of challenges for optimal peak separation and sensitivity. To prevent the condensation of low volatile analytes on cold surfaces the entire path of the column was consistently heated from the GC all the way down to the column tip in the ion source. This required particular demands on the used materials. For example, different expansion coefficients needed to be considered, especially for the transition of the glass plasma tube to the metal interface of the MS. Also, high-temperature resistant and non-outgassing sealing was required, withstanding numerous heating and cooling cycles [51]. Furthermore, only minimal amounts of gas are added to the analyte as compared to monitoring applications. This offers best possible reduction of unnecessary dilution, however, the design needs to carefully balance the total flow condition to prevent peak-broadening caused by increased dwell times.
The ion source Design 3 served as a *Proof-of-Concept*. The main aim was (i) testing of graphite as non-outgassing, heat resistant sealing material and (ii) a controlled operating temperature of up to 300 °C.

Essentially, the ion source was made of two parts, the plasma tube and the reaction tube (cf. Figure 9, chapter 3.9.3). In the plasma tube the RF hydrogen discharge forms H_3^+ as the

primarily charge carrying species. The reaction tube provides the necessary time, pressure and mixing to convert this primary charge into protonated analyte ions. In this setup the entire reaction cascade is again driven as a "one-pot" reaction. This means that an excess of reagent gas is added together with the analyte. An additional reagent gas inlet would have involved further sealing efforts and glass-to-metal transitions, increasing the risk of leaks. The length of the reaction tube was kept as long as necessary and as short as possible to avoid ion loss on the surfaces. The length was mainly determined by the dimension of the flexible GC transfer line, which had to be mounted directly to the ion source to avoid cold spots. The reagent gas inlet between the plasma and the reaction region was tangentially aligned to the glass tube so that the laminar plasma effluent was radially surrounded. Whereas the exit of the GC column was placed on the center axis of the tube. Due to laminar flow conditions and ion losses by radial diffusion, the highest reagent gas ion concentration is expected to be near the center axis.

To effectively guide the ions into the next differentially pumped transfer stage, some kind of RF focusing was needed for this given pressure range. Although other focusing devices are certainly more appropriate, the short stacked quadrupole was readily available for reuse without much effort or modification.

The entire source body was temperature stabilized with a heating wire Due to the small bending radius of the wire, also the plasma tube could be covered to warm up this region as well. In order to reduce any temperature fluctuations caused by the PID controller, the ion source material should be able to damp these fluctuations through sufficient heat capacity. A further challenge was the thermal insulation between Design 3 and the directly connected SSQ chamber. The operating temperature of the source was laid out for 300 °C, whereas the SSQ chamber including the TOF housing and electronics were to remain close at room temperature. In order to keep both regions in their optimal operating conditions, the thermal conductivity between them was best possibly minimized through a very thin junction and the heat dissipation in the colder region was best possibly maximized through a large surface. The latter was only limited by the SSQ chamber dimension. Eventually, Design 3 managed this challenge and while the source block was homogenously heated to 300 °C, the temperature of the mounting flange on the SSQ chamber did not exceed 36 °C. More results on the ion source heating and sealing are discussed in chapter 4.7.1.

Initially, a continuous analyte addition of a benzene, toluene and *o*-xylene mixture in N_2 was used to determine the optimum operating parameters and to compare the results with the previous source versions. However, with Design 3, the analyte gas flow could be reduced to

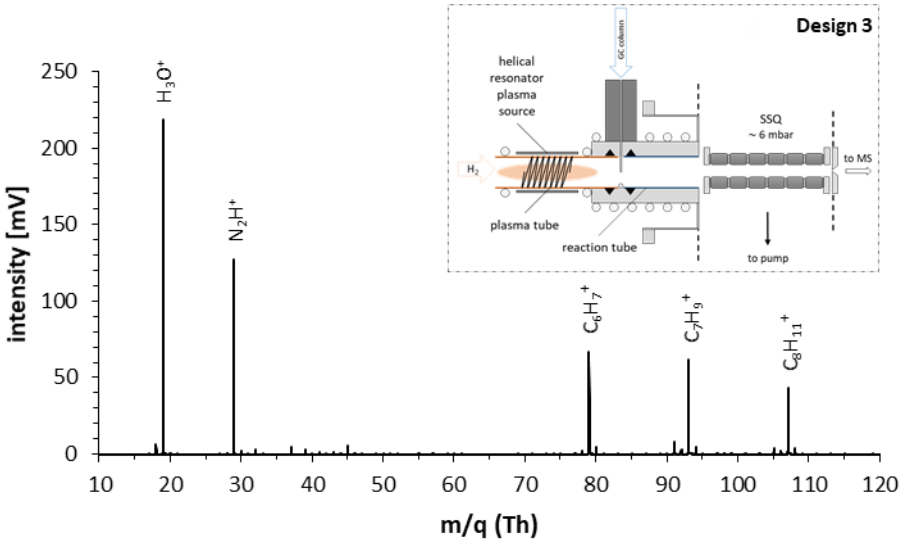

Figure 29: Mass spectrum obtained with the chemical ionization source Design 3. 50 sccm H_2 plasma gas flow, 1 sccm BTX-mixture in N_2 (cf. Table 16, #2, appendix) and 5 sccm N_2 as reagent gas at 5.8 mbar. Ion transfer settings cf. Table 18 #2 (appendix).

1 sccm and thus readily be adapted to GC effluent conditions. The pressure in the plasma and reaction region was slightly increased to around 6 mbar and the reagent gas flow was reduced to around 5 sccm. For these conditions a mass spectrum recorded with the ion source Design 3 is shown in Figure 29.

The obtained mass spectrum is similar to the previous. The observed background ions are, again, N_2H^+ and, more pronounced, H_3O^+. The analytes benzene, toluene and *o*-xylene are predominantly observed in protonated form. Fragments of toluene and *o*-xylene are still present, but with 11 and 7 %, respectively, slightly less compared to the previous designs.

The continuous introduction of the BTX calibration mixture was important for the optimization of all operating parameters and to compare the results with the previous ion source versions. Various analytes and reagent gases were tested by introduction via the gas chromatograph (cf. chapter 4.6) to characterize the analytical performance of this ion source design for GC-MS applications. α-Pinene served as a marker for fragmentation. Strong fragmentation of α-pinene was observed with the ion optics voltages that were previously tuned to the BTX mixture. The voltages in the SSQ region were adapted to minimize fragmentation ("soft" ion transfer settings, cf. Settings Table 18 #1).

Figure 30 shows the background mass spectrum obtained with "soft" ion transfer settings in the SSQ. The water cluster system is noticeably dominated by higher clusters compared to the mass spectrum obtained with the transfer settings #2 from Table 18. The first three water

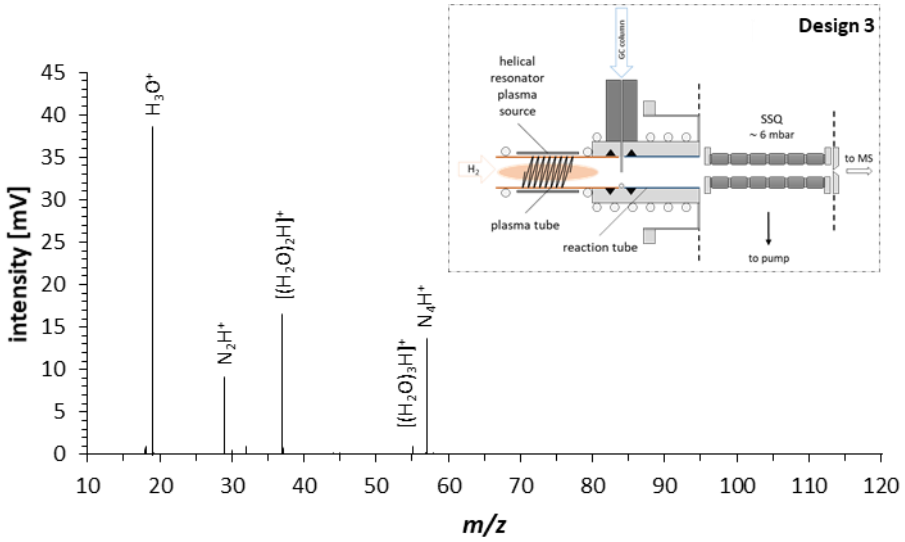

Figure 30: Mass spectrum obtained with the chemical ionization source Design 3. 50 sccm H_2 plasma gas flow, 6 sccm N_2 as reagent gas at 5.8 mbar. "Soft" ion transfer settings (cf. Table 18 #1, appendix).

species - H_3O^+ to $[(H_2O)_3H]^+$ - appeared. Also, the proton-bound nitrogen cluster N_4H^+ is detected. Once formed, cluster ions might not be dissociated due to the "soft" ion optics settings. Moreover, this also might be attributed to the longer dwell time inside the SSQ. Compared to the previous transfer settings (cf. Table 18 #2 vs. #1) there is no DC gradient applied within the SSQ. Thus, the axial transport of the ions is solely driven by the bulk gas flow.

4.4.4 Design 4

With the final ion source iteration, Design 4, the remaining issues concerning peak tailing and ion source heating were solved. The basic design concept of the plasma zone, the reagent gas, GC effluent addition, and the reaction region were retained from the preceding version (Design 3). The key difference is the housing of the SSQ. The entire gas - plasma, reagent and analyte – is guided directly in front of the skimmer, where the ions are extracted and the neutral gas is pumped away by the differential pumping stage. This significantly reduces the dead volume previously represented by the SSQ chamber and prevents the neutral analyte from being scattered across the entire SSQ chamber. The chromatographic performance of this ion source version compared to the preceding version, e.g. concerning peak tailing, is discussed in detail in chapter 4.7.2

The replacement of the plasma tube and the reaction tube by a ½ inch borosilicate glass enabled the use of standard ½ inch graphite/Vespel seals as heat-resistive and non-outgassing sealing of the glass tubes. The ion source including the SSQ housing can now be heated to up to 300 °C by a temperature-controlled heating cartridge that is fully integrated into the ion source enclosure and remains leak-proof even after multiple heating and cooling cycles.
Figure 31 shows the mass spectrum recorded with the final ion source iteration Design 4. The same ionic species as with the ion source Design 3 are observed in the spectrum except of the third water cluster $[(H_2O)_3H]^+$. Also, the ratio between H_3O^+ and $[(H_2O)_2H]^+$ is significantly lower compared to the preceding setup. Note, that the ion source pressure was increased to 13 mbar and the total gas flow was increased to 300 sccm. In combination with the SSQ housing, this results in shorter dwell times compared to the preceding ion source setup.

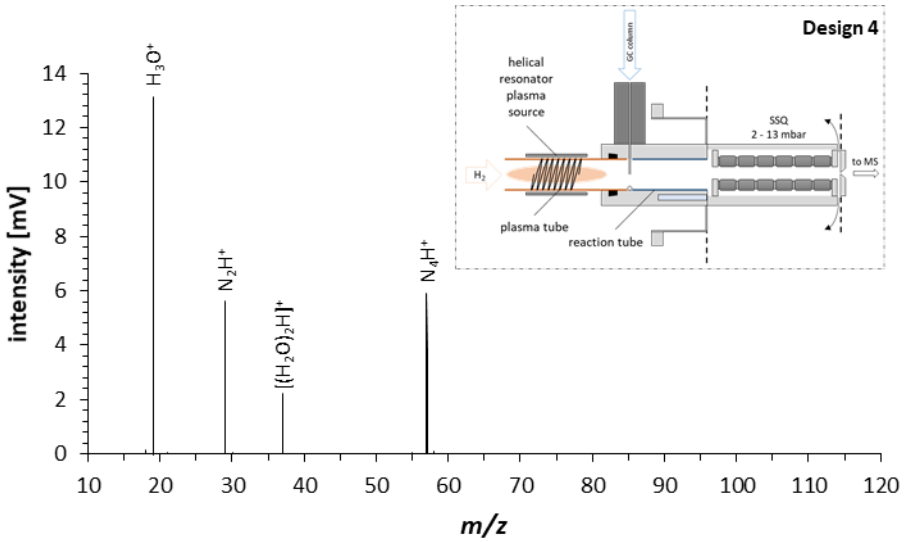

Figure 31: Mass spectrum obtained with the chemical ionization source Design 4. 100 sccm H_2 plasma gas flow, 200 sccm N_2 as reagent gas, 1.2 sccm He as GC carrier gas at 13 mbar. Ion source temperature 250 °C . Ion transfer settings (cf. Table 18 #3, appendix).

4.4.5 Comparison

To get a glimpse of the progression in the ion source development process and to compare the different ion source iterations, the sensitivity was determined for each ion source design. For a better comparison with GC-MS measurements, especially for the ion source Design 3 and Design 4, the sensitivites for the considered analytes were calculated in counts fg^{-1}. In case of continuous analyte addition, the sensitivity was calculated by dividing the obtained signal intensity in cps by the total amount of the added analyte per second, estimated via the mixing ratio in ppmV and the gas flow. For GC-MS measurements, the obtained signal peak area was

Table 5: Sensitivities of the respective chemical ion source designs.

CI source Design	Benzene [counts fg^{-1}]	Toluene [counts fg^{-1}]	*o*-Xylene [counts fg^{-1}]
Design 1[a,b]	0.18 ± 0.02	0.14 ±0.01	0.12 ±0.01
Design 2[b]	0.0059 ± 0.0009	0.011 ± 0.001	0.015 ±0.002
Design 3[b]	1.7 ± 0.2	1.6 ± 0.3	1.0 ± 0.2
Design 3[c]	-	-	0.591 ± 0.002
Design 4[c]	-	-	0.093± 0.002

[a] modification #3; [b] continuous analyte sampling; [c] GC analyte sampling

divided by the amount of the injected analyte. Table 5 depicts the sensitivites of benzene, toluene and *o*-xylene, obtained with the respective ion source iterations.

Comparing ion source Design 1 versus Design 2, it is seen, that the sensitivity decreased by about a factor of 10. As stated in chapter 4.4.2, the ion signal with Design 2 was nearly unaffected by the quadrupole frequency and amplitude, probably due to charging of the glass tube, which results in shielding of the RF field. Thus, no active ion guiding or focusing by the applied RF fields can be expected, resulting in significant charge losses at the tube surfaces, analogous to the losses observed during the ion current measurements in the vacuum recipient (cf. chapter 4.2.1). The sensitivity is further increased by a factor of 10 when the SSQ housing is removed (cf. Design 1 vs. Design 3).

Regarding the analyte introduced via the gas chromatograph compared to a continuous analyte addition, it is seen that the sensitivity for *o*-xylene decreased to approximately 60 %. This is likely due to the pronounced peak tailing observed with ion source Design 3 (cf. chapter 4.7.2). Considering this, the obtained sensitivity can be assumed equal.

Design 4's sensitivity appears to be significantly worse at first glance compared to Design 3. However, it is important to bear in mind that the TOF instrument was also modified. An ion bender system was integrated into the ion transfer stage. This led to a 2-3 fold decrease in sensitivity of the device. Besides, the system was optimized for the best signal-to-noise ratio, leading to an operating pressure of 13 mbar. The signal intensity decreased by about a factor of 2, compared to an operating pressure of 6 mbar. Considering all this, the sensitivity of the last ion source iteration, Design 4, is quite comparable to the preceding iteration (Design 3).

4.5 Plasma Afterglow Effects

According to the conclusions from the subsequent iterations of the ion source Design 1, the formation of the primary charge carrying species H_3^+ in the plasma region was no longer separated from the analyte ionization region. Due to the lack of spatial separation, these two

processes tend to overlap and impair the ionization process of the analyte. This effect, in the following called *plasma afterglow effect,* and its impact on the ionization process is considered in this section. To investigate this effect the formation of ammonia, specifically its ionic derivatives of NH_x^+ ions and their distribution is studied.

Ammonia can be produced by nitrogen-hydrogen low pressure (0.01-10 mbar) RF discharges [87–90] in considerable quantities. Chemical kinetic models, however, revealed that gas-phase reactions alone are not able to produce ammonia in detectable amounts [91, 92]. Thus, it is reasonable to assume that the plasma in combination with heterogeneous wall effects significantly catalyzes its formation. Interestingly, the active surface material is not only limited to metal, since reactions were also observed on quartz surfaces [92].

To generate ammonia in a plasma, the precursor molecules (i.e., N_2 and H_2) must first dissociate, exposing the wall to high fluxes of atomic and molecular radicals. The production of NH_3 is then assumed to take place on the surface by successive hydrogenation of adsorbed H and N atoms, and N-containing radicals [93]. The ionic composition of the plasma is entirely driven by gas-phase processes. At total pressures above ~ 0.04 mbar the ion distributions are dominated by ion-molecule reactions [91, 93]. Only small amount of NH_3 is produced on the surface. Due to the high proton affinity of ammonia compared with H_2 and N_2, virtually any collision of NH_3 with H_3^+ or N_2H^+, respectively, will lead irreversibly to the production of NH_4^+. To explain the formation of ammonia on the surface and in gas-phase reactions at the given pressure range, an efficient dissociation of N_2 in the plasma region must be assumed. There is no known reaction pathway commencing with ionic species primarily formed in the hydrogen plasma that can lead to the formation of either N atoms or N^+ or N_2^+ ions. This means that the reaction can only occur in case the plasma zone or at least the plasma afterglow markedly overlaps with the nitrogen reagent gas addition. When this condition is met, the mentioned nitrogen species can be formed by, e.g., electron ionization, electron dissociation or electron neutralization. Therefore, this ionic species is an excellent indicator for studying *plasma afterglow effects*.

The investigation of NH_4^+ formation in this work is described in the following. A hydrogen plasma was ignited at a pressure of about 4.3 mbar using the ion source Design 2 (cf. chapter 3.9.2) with standard measurement settings. Small amounts of nitrogen were successively added to the plasma gas flow.

Figure 32 shows the NH_4^+ and NH_3^+ ion signal depending on the plasma gas composition. It clearly depicts the linear correlation between the observed NH_x^+ population and the nitrogen mixing ratio. Both ion species, NH_3^+ and NH_4^+, show the same response to the mixing ratio (cf.

slope of linear regression functions). This indicates that the formation of both ions is likely based on the same reaction pathway.

The intercepts of the y-axis deviate from zero. Assuming a linear correlation also for smaller mixing ratios, a background nitrogen mixing ratio of 0.8 % can be estimated based on the standard addition method. This fairly high background level of nitrogen cannot be explained by contaminations alone. Since the ion source operated at standard measurement settings, nitrogen was introduced downstream as the reagent gas at a distance of 72 mm (between the center of the RF power supply and the reagent gas addition). Consequently, it is reasonable to assume considerable back diffusion into the plasma region (compare simulation results from Figure 69, chapter 4.8.1).

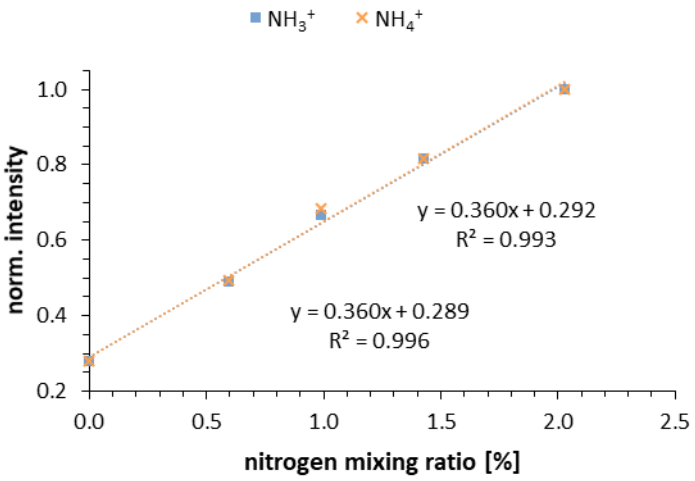

Figure 32: NH_4^+ and NH_3^+ ion signals depending on the plasma gas composition.

To further investigate back diffusion effects of the reagent gas and thus the impact of the plasma afterglow on the analyte ionization process, the crucial parameters (i) pressure and (ii) distance between the plasma region and the analyte addition were examined in detail.

All experimental results under consideration in this chapter were obtained with the ion source Design 2. A brief schematic drawing of the measurement setup is given in Figure 33. For further design details the reader is referred to chapter 3.9.2. The experimental conditions were as follows: A hydrogen plasma gas flow of 30 sccm and 100 sccm of a benzene/toluene/*o*-xylene mixture (cf. Table 16 mixture #1, appendix) in nitrogen were used. The pressure was kept constant at 3.05 mbar and the spacing between the plasma region and the analyte addition was

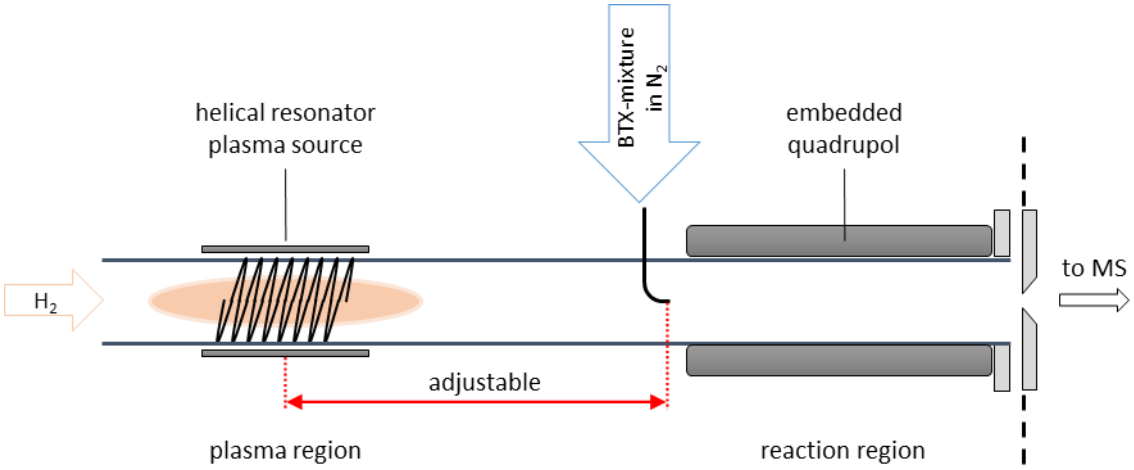

Figure 33: Schematic drawing of the measurement setup for studying plasma afterglow effects.

72 mm, if not otherwise stated. The distance could be exactly adjusted during a measurement by sliding the RF power supply over the plasma glass tube to maintain consistent conditions.

4.5.1 Distance Dependency

Figure 34 shows the marked dependence of the total ion current on the distance between the plasma region and the reagent/analyte gas mixture addition. Initially, the TIC sharply increases with decreasing distance, reaches a maximum at a distance of around 70 mm and then exponentially drops. As ion current measurements have already shown (cf. chapter 4.2.1) a significant amount of ions is lost presumably due to neutralization on the plasma glass tube surface. In this case, an ion loss of 75 % between the maximum at 70 mm and the minimum signal at the furthest measured distance was observed. Therefore, all signals are normalized to the TIC in the following.

The signal drop from the maximum to shorter distances is assumed to be an effect of mass discrimination. The short segmented quadrupole has a mass dependent transmission efficiency under the given pressure regime. The operation mode was set to medium mass range. As will be seen later, shorter distances cause more fragmentation, which shifts the signal distribution in the mass spectrum to smaller masses. Also at shorter distances, more NH_x^+ ion species are formed from the bulk gas (N_2) with a simultaneous decrease in the main background signal (N_2H^+). Due to the mass difference of N_2H^+ compared to NH_x^+ and the mass discrimination effect of the SSQ, the TIC is decreased.

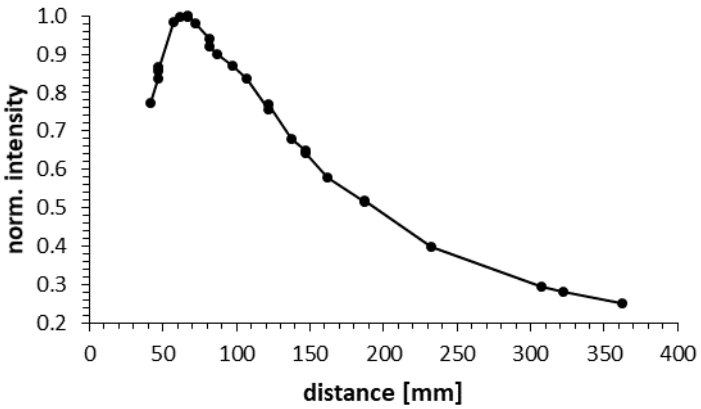

Figure 34: Normalized total ion current in dependency of the distance between the plasma region (center of RF plasma discharge) and the reagent/analyte gas mixture introduction.

Figure 35 depicts the normalized NH_2^+, NH_3^+ and NH_4^+ ion signals as a function of the distance between the plasma region (center of RF plasma discharge) and the reagent/analyte gas mixture introduction.

Initially, by decreasing the distance the NH_x^+ ion signals remain constant over a large range. Starting at about 100 mm, however, the NH_x^+ ion signals sharply increase while the ion distribution remains the same. The main ion signal is NH_4^+, followed by NH_3^+ and then NH_2^+. These increasing NH_x^+ signals with decreasing distance can be interpreted as an overlap of the plasma afterglow with reagent/analyte introduction, according to the previous argumentation.

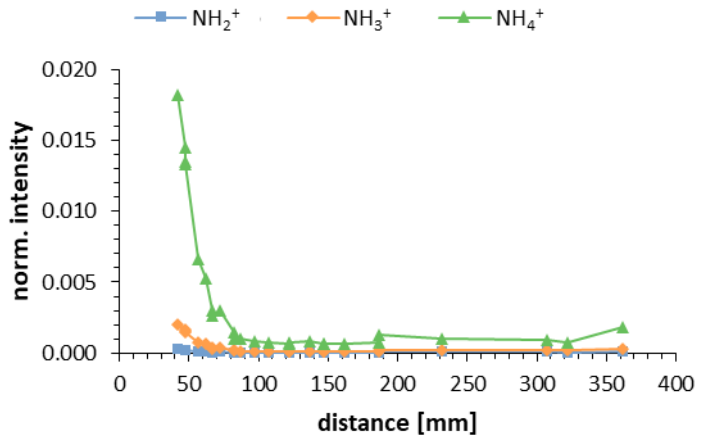

Figure 35: Normalized NH_2^+, NH_3^+ and NH_4^+ ion signals as function of the distance between the plasma region (center of RF plasma discharge) and the reagent/analyte gas mixture introduction.

With reduced distance, the amount of nitrogen increases that reaches the plasma region through either back diffusion or through the direct overlap between the plasma afterglow and the nitrogen introduction. This also enhances the degree of N_2 dissociation, which eventually leads to the formation of NH_x^+.

The direct interaction of the plasma zone with the reagent/analyte gas supply is also accompanied by increasing fragmentation ratios of the analytes. Table 6 gives an overview of all identified analyte related ion signals, including fragments and adducts.

Table 6: Observed ions derived from a benzene/toluene/xylene mixture in N_2.

Nominal mass *m/z*	Molecular formula	Classification
122	$C_8H_9NH_3^+$	$[A]^+$
107	$C_8H_{11}^+$	$[X+H]^+$
106	$C_8H_{10}^+$	$[X]^+$
105	$C_8H_9^+$	$[X-H]^+$
93	$C_7H_9^+$	$[T+H]^+$
92	$C_7H_8^+$	$[T]^+$
91	$C_7H_7^+$	$[T-H]^+$
79	$C_6H_7^+$	$[B+H]^+$
78	$C_6H_6^+$	$[B]^+$
65	$C_5H_5^+$	$[F]^+$
39	$C_3H_3^+$	$[F]^+$

B = benzene; T = toluene; X = xylene; A = adduct; F = fragment; H = hydrogen

Figure 36 gives an overview of different ion ratios as a function of the distance, whereby: (i) the fragmentation ratio is defined as the sum of all observed analyte fragment ion signals divided by the sum of all observed analyte related signals (cf. Table 6), (ii) the protonation ratio is defined as the sum of the $[M+H]^+$ signals of the analytes divided by the sum of all observed analyte related signals and (iii) the molecular ion ratio is defined as the sum of the molecular analyte ion signals divided by the sum of all observed analyte related signals.

Regarding the fragmentation, Figure 36 clearly shows a sharp increase from 90 mm to 40 mm. In contrast, between 100 mm and 360 mm the fragmentation ratio remains nearly constant and falls off by merely 1 %. The observed main analyte fragments with a relative abundance of 4-6 % and 7-9 % are assigned to the $[M-H]^+$ species $C_8H_9^+$ and $C_7H_7^+$, respectively. The two additional fragments $C_5H_5^+$ and $C_3H_3^+$ constitute less than 2 % to the total ion current throughout the entire distance range. Possible fragmentation pathways are dissociative charge transfer reactions of N^+ and N_2^+ from back-diffused nitrogen into the plasma region or direct electron dissociation.

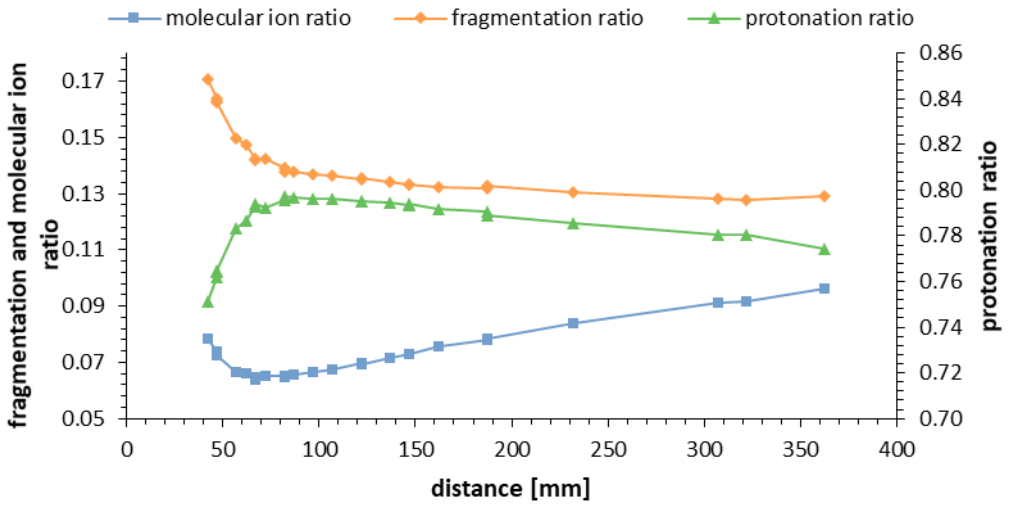

Figure 36: Molecular ion ratio, fragmentation ratio (*left y-axis*) and protonation ratio (*right y-axis*) in dependency of the distance between the plasma zone (center of RF plasma discharge) and the reagent/analyte gas mixture addition.

With respect to the protonation ratio, an inverse progression to the fragmentation trend is found, which is more pronounced at short gaps between the nitrogen inlet and the plasma effluent. Figure 36 shows a steep increase in protonation by 6 % starting at 40 mm and climaxing at 80 mm. Since the product ratio for the protonated analytes, $[M+H]^+$, is unity, the anticipated pathway is via the reagent gas species N_2H^+. This is reasoned by the following: A direct protonation via H_3^+, that is primarily formed in the plasma, would result in considerable fragmentation of at least toluene (20 % $C_7H_7^+$, 5 % $C_6H_5^+$). Xylene would presumably be fragmented as well, since its structure is very similar. Benzene, however, is rather stable and stays intact when a proton from H_3^+ is transferred [94]. Therefore, a significantly different signal distribution would be expected in case of H_3^+ as the primary reagent species. In conclusion, the spectra unambiguously reveal quantitative conversion of H_3^+ into N_2H^+ at every plasma position.

Figure 37 depicts the normalized $[M+H]^+$ signals of the analytes in dependence of the plasma distance. All $[M+H]^+$ ion signals follow the same trend. Again, this strongly supports the previous conclusion that a direct protonation with H_3^+ is virtually absent in this setting.
At small plasma to analyte inlet distances the molecular ion ratio follows a similar trend as the fragmentation ratio, except the characteristic minimum at around 75 mm. Beyond this point the signal increases linearly with increasing distance. This signal progression indicates several

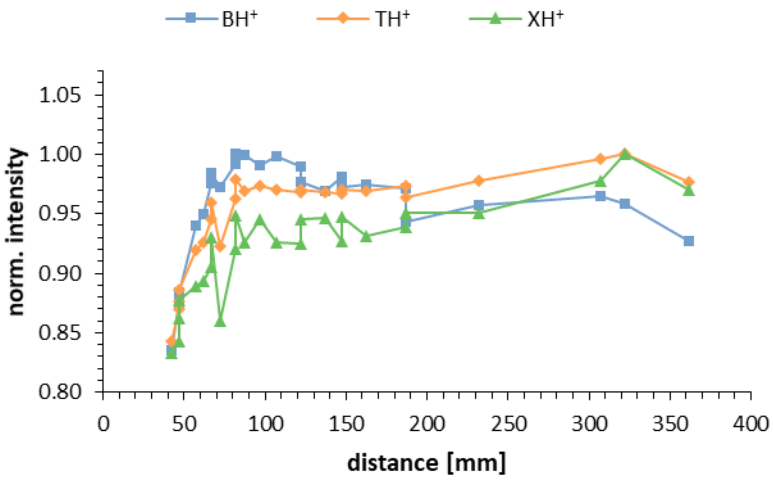

Figure 37: Normalized ion signals of the protonated analytes benzene (BH^+), toluene (TH^+) and *o*-xylene (XH^+) for different distances between the plasma region (center of RF plasma discharge) and the reagent/analyte gas mixture addition.

effects on the molecular ion formation with their distinct dependency on the plasma position. To explain this behavior, two essentially different pathways for the M^+ formation need to be considered: (i) charge transfer and (ii) photoionization. The latter is rationalized, since the hydrogen plasma emits photons of 10.2 eV [74], which is sufficient for the required photoionization energies of 9.24 eV (benzene), 8.82 eV (toluene) and 8.55 eV (*o*-xylene) [95]. At short distances it can be assumed that charge transfer processes or direct electron ionization dominate as a result of the direct overlap with the plasma zone. Consequently, at this point the M^+ fraction is substantial. However, small shifts of the active plasma zone away from the analyte inlet rapidly degrades feasible charge transfer species such as N^+ and N_2^+ and causes the observed drop of the molecular ion ratio down to the minimum. Continuing this shift brings photoionization into the fore. This formation mechanism of M^+ differs substantial from the previous ion molecule reactions. The M^+ formation via photoionization depends solely on the from the hydrogen plasma emitted photon flux and according to the Lambert-Beer law the overall ion population is proportional to the length of the light path. This remains constant for the analytes and the light intensity even decrease with the increasing distance from the plasma. However, the molecular ion ratio is calculated as the sum of the molecular analyte ion signals divided by the sum of all observed analyte related signals. This simply means, that the photoionization process become dominant against ion-molecule reactions, forming the $[M+H]^+$ ions. The ion loss due to neutralization on the plasma glass tube surface overweighs the decrease in photon flux with inceasing distance.

4.5.2 Pressure Dependency

In the following section the implications of pressure variation on the ionization process were studied in a range from 0.7 – 8.0 mbar. First of all, the dimension of the plasma zone is inversely proportional to the gas density, which implies that with decreasing pressure the afterglow extends towards the reagent gas inlet. Further, the back diffusion into the plasma region is more pronounced with decreasing pressure. Eventually, this will allow the afterglow to dominate the ion chemistry, with similar effects on the ion distribution as in the plasma distance variation experiments.

As discussed previously, the formation of NH_x^+ species is an excellent indicator for exactly this impact of the afterglow. These species thus mark a certain interaction with the plasma afterglow and the influence of parameters on the fragmentation and protonation ratios, which are extremely relevant for the evaluation of the ionization process and the ion source performance.
The left plot in Figure 38 shows the normalized NH_2^+, NH_3^+ and NH_4^+ ion signals as a function of the pressure. The exponential decrease of the NH_x^+ ion signals with increasing pressure is apparent and supports the picture of the spatially shrinking afterglow at higher gas densities with less impact on the ion distribution. The same trend was already shown in the previous distance dependency section and it also perfectly correlates with the analyte fragmentation ratio depicted in the right plot in Figure 38. Again, this indicates that with lower pressure the plasma afterglow expands and affects the ionization process in certain ways.

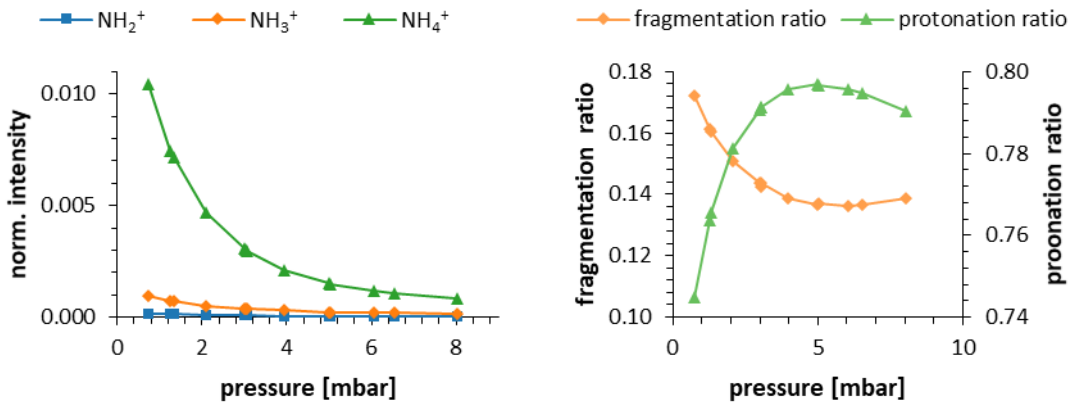

Figure 38: *Left:* Normalized NH_2^+, NH_3^+ and NH_4^+ ion signals as function of the pressure. *Right:* Fragmentation ratio (*left y-axis*) and protonation ratio (*right y-axis*) as a function of the pressure.

One essential parameter accompanied with the gas density in such a flow system is the dwell time of the species primarily formed in the plasma zone. Halving the pressure doubles the gas velocity and consequently halves the dwell time, provided that the distance between the plasma center and the reagent gas inlet is kept constant. A second essential parameter is the total number of collisions per unit time and volume, which is proportional to the pressure as well. As a result, at low pressures both effects prevent the quantitative turnover of all the ionic plasma species into H_3^+ before encountering the reagent gas inlet region. This partially explains the pronounced NH_x formation at reduced pressures in left plot and also the lower protonation and higher fragmentation ratios in the right plot. It should be noted that the observed fragment and adduct ions are exactly identical to the ones listed in Table 6. Interestingly, the slope of the protonation ratio shows a distinct maximum at around 5 mbar. This result is not evident and leaves room for further interpretations.

To summarize, it was shown that the ionic derivatives of NH_x^+ result from the direct interaction with the hydrogen plasma and the introduced reagent gas nitrogen, thus may serve as indicators for the plasma afterglow effect. These signals clearly correlate with the fragmentation ratio of the analyte. Ideally, the analyte should only be ionized by the added reagent gas and a direct interaction with the plasma afterglow should be avoided. Pressure and distance between the plasma region and the reagent gas addition are two crucial parameters that must be carefully considered in such a chemical ionization source design. It is essential to find a good compromise between ion losses on the plasma tube surface, i.e., a high primary ion current of H_3^+ as main ion, and preferably less interaction with the plasma afterglow, which leads to substantial fragmentation of the analyte. Therefore, the crucial parameters pressure and dwell time have to be carefully balanced.

4.6 Different Reagent Gases

The main ionic species present in the RF hydrogen plasma is H_3^+, one of the strongest known gas phase acids. The low proton affinity of H_2 with 422.3 kJ mol^{-1} [49] fortunately allows to unselectively protonate a considerable range of compounds [50, 94, 96] with H_3^+. On the other hand, a reasonable CI scheme also requires precaution of the excess energy accompanied by the charge transfer process. Since H_2 as one of the products cannot store tremendous amounts of vibrational energy, most of the exothermicity eventually remains in the internal degrees of freedom of the charged analyte and potentially induces bond breaking. The degree of fragmentation then depends on the ability of the gas matrix to rapidly dissipate this excess energy into the environment and, of course, on the initial amount of deposited energy into the vibrational modes of the molecular system. The latter expressed as the difference in proton affinities between hydrogen and the neutral analyte. Consequently, a reasonable CI scheme should avoid extensive fragmentation, which implies a well-balanced system of the prevailing pressure and a primary reagent with a tailored proton affinity [97]. Eventually, a balance also involving very basic practical aspects, like maintaining a plasma in common space with a CI stage, providing downstream kinetic control to most possibly reflect the neutral mixing ratios and a balance between selective and unselective ionization. A look at Table 7 to some small- to medium-sized organic molecules shows proton affinities ranging between 650 and 900 kJ mol^{-1}, in some rare cases even exceeding 1000 kJ mol^{-1} [49]. With H_3^+ as the protonating species, this translates to excess energies between 2 and 5 eV.

This chapter addresses practical aspects to downregulate the acidity of the protonating agent by adding an additional gas further downstream of the plasma effluent. The quantitative transformation from H_3^+ into secondary reagent ions allows less exothermic protonation of analyte molecules. This reduces ion fragmentation and essentially simplifies mass spectral interpretation. Furthermore, it can aid in differentiation of two analytes with the same molecular mass but very different proton affinities [98]. In the following, various gases are investigated in the developed ion source for their suitability as secondary CI reagents.

Table 7: Overview of proton affinities (PA), gas phase basicities (GB) and ionization energies sorted by proton affinity values.

Base	Nominal mass	PA [kJ mol^{-1}]	GB [kJ mol^{-1}]	Ionization energy [eV]
Ar	40	369.2[a]	346.3[a]	15.76[g]
H_2	2	422.3[a]	394.7[a]	15.43[g]
N_2	28	493.8[a]	464.5[a]	15.58[g]
CH_4	16	543.5[a]	520.6[a]	12.61[g]
C_2H_6	30	596.3[a]	569.9[a]	11.52[g]
C_2H_2	26	641.4[a]	616.7[a]	11.40[g]
C_6H_{14}	86	672.4[d]	-	10.13[g]
iso-C_4H_{10}	58	677.8[a]	671.3[a]	10.68[g]
C_2H_4	28	680.5[a]	651.5[a]	10.52[g]
$C_{10}H_{22}$	142	690.4[d]	-	9.65[g]
H_2O	18	691[a]	660.0[a]	12.62[g]
(E)-$CH_3CH{=}CHCH_3$	56	747[a]	719.9[a]	-
C_6H_6	78	750.4[a]	725.4[a]	9.24[g]
$CH_3CH{=}CH_2$	42	751.0[b]	718.0[b]	-
c-C_3H_6	42	752.0[b]	720.0	-
$H_2C{=}C{=}CH_2$	40	775.3[a]	745.8[a]	-
CH_3CCH	40	748[a]	723.0[a]	-
$C_6H_5CH_3$	92	784.0[a]	756.3[a]	8.83[g]
o-$C_6H_4(CH_3)_2$	106	796.0[a]	768.3[a]	8.56[g]
$(CH_3)_2C{=}CH_2$	56	802.1[a]	775.6[a]	-
$(H_2O)_2$	36	808.0[e]	-	-
c-C_3H_4	40	828.0[b]	795.0[b]	-
$C_6H_5OCH_3$	108	839.6[a]	807.2[a]	8.20[g]
NH_3	17	853.6[a]	819.0[a]	10.07[g]
α-pinene	136	878.6[c]	-	8.07[g]
$(H_2O)_3$	54	929.2[f]	-	-
$(H_2O)_4$	72	1004.4[f]	-	-

[a] cf. ref. [49]; [b] cf. ref. [99]; [c] cf. ref. [100]; [d] cf. ref. [101]; [e] cf. ref. [102]; [f] cf. ref. [103]; [g] cf. ref. [104]

4.6.1 Chemical Reaction System

The chemical reaction system of the primary charge carrying species, H_3^+, and the secondary reagent is investigated. At first instance the simplest way to do so involves the variation of the reagent gas concentration while keeping all remaining conditions constant. However, this procedure is not as trivial with the present system and under the given circumstances as it might seem.
If we were to consider only the reaction system between H_3^+ and the respective secondary reagent, the background gas would need to be absolutely inert, which is only the case for Helium. But even for this epitome of inertness, a proton transfer reaction is only endothermic for the ground-state H_3^+, while in the excited state it can yet protonate Helium to HeH^+ [94]. Moreover, previous measurements have shown an optimum ion source pressure for analyte protonation at around 6 mbar. The ideal mixing ratio between the hydrogen plasma gas and the reagent gas flow is 50/6 sccm for nitrogen as the secondary reagent. This mixing ratio maintains the optimum pressure with respect to the degree of analyte protonation and with regard to the required downstream pressures in the differentially pumped stages. Consequently, the inert background gas would also need similar physical properties to retain these pressure regions at their optimum. Accordingly, varying the secondary reagent mixing ratio is not a simple approach to investigate its impact on the chemistry.

Another way to gain insight into the reaction system is to alter the reaction time. This can be realized by changing the ion source pressure with a bypass to the fore pump. The dwell time in the ion source is proportional to the pressure. Halving the pressure doubles the gas velocity and with constant traveling distance, it also halves the dwell time within the ion source. For various gases, the ion source pressure was varied within the allowed range of this experimental setup, which corresponded to approximately 0.3 to 6 mbar. The lower range was limited by the total gas flow and the pumping capacity of the vacuum pump, which depends on the gas composition and therefore on the used reagent gas. The upper range was limited by the pumping capacity of the second differentially pumped stage.
The ion source pressure range from 0.3 to 6 mbar corresponds to an ion source dwell time of approximately 2 to 40 ms, estimated according to the mean gas velocity within the reaction tube and the ion transfer time through the SSQ, which was obtained by SIMION simulations. Pressure variation also influences the total number of collisions. Doubling the pressure doubles the collisions per unit time, but the total number of collisions is quadrupled. This dependency

is quadratic, since both, the dwell time in the ion source and the collision number per unit time are linear functions of the pressure.
For all following measurements, field induced fragmentation was set to a minimum by applying very low voltages to all the electrodes down to the skimmer (cf. Table 18 #1, appendix), ensuring "soft" ion transfer conditions. Furthermore, in all measurements discussed in this chapter, the hydrogen plasma gas flow and the reagent gas flow were kept constant during each pressure dependency series, but the total mixing ratio may slightly differ for each reagent gas. Another parameter which was kept constant during all measurements was the distance between the plasma source and the reagent gas inlet. It was assumed, that the plasma chemistry is fast enough, even at the lowest pressure, to quantitatively convert any charge of the plasma into H_3^+ before entering the reagent gas region. However, as discussed in detail in chapter 4.5, the direct interaction between the afterglow and the reagent gas at reduced pressures could not be completely excluded

Reagent gas: Nitrogen

The first reagent gas under consideration was nitrogen. Its proton affinity exceeds the PA of hydrogen by 71.5 kJ mol^{-1} (cf. Table 7) and is expected to exclusively form N_2H^+ via the rapid proton transfer reaction($1.86 \cdot 10^{-9}$ cm^3 s^{-1} [50]):

$$H_3^+ + N_2 \rightarrow N_2H^+ + H_2 \qquad \text{(R 9)}$$

Figure 39 shows the ion signal distribution as a function of the source pressure between 0.3 and 6.1 mbar. In the lower range up to 3 mbar, the protonated nitrogen N_2H^+ clearly is the dominating species, followed by H_3O^+ with nearly an order of magnitude lower intensity.

Starting at 1.5 mbar a signal of *m/z* 57 arises, which is assigned to N_4H^+. This species is formed in an equilibrium reaction of N_2H^+ with excess neutral nitrogen according to:

$$N_2H^+ + N_2 + M \rightleftharpoons N_4H^+ + M \qquad \text{(R 10)}$$

As the N_4H^+ signal increases, the N_2H^+ signal decreases. At a pressure of around 2.5 mbar, the H_3O^+ signal starts to increase. At even higher pressures water clusters are formed step by step, beginning with the lowest water cluster number 2 ($(H_2O)_2H^+$) and up to the highest water cluster number 5 ($[(H_2O)_5H]^+$).
Obviously, neutral trace contaminants, particularly H_2O, could not be completely removed. Because of the rapid reactions between H_3^+ and water ($5.30 \cdot 10^{-9}$ cm^3 s^{-1} [50]) and the similarly

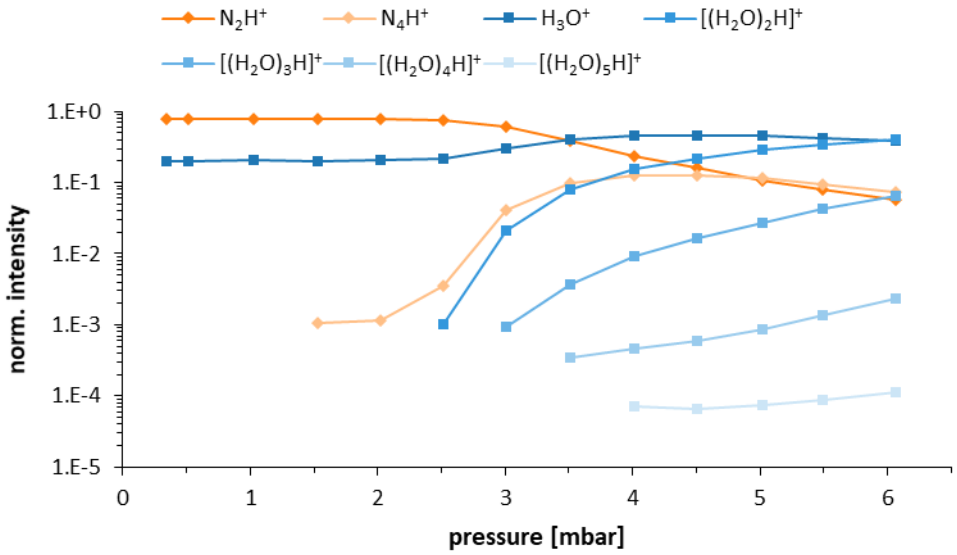

Figure 39: Ion source Design 3 with nitrogen as reagent gas. Ion signal distribution as a function of the ion source pressure in the range of 0.3 – 6.1 mbar. (10.4 % N_2).

fast reaction between N_2H^+ and water (R 12) ($2.60 \cdot 10^{-9}$ $cm^3\,s^{-1}$ [50]), even trace levels of this contaminant significantly contributed to the recorded mass spectrum.

$$H_3^+ + H_2O \rightarrow H_3O^+ + H_2 \qquad \text{(R 11)}$$

$$N_2H^+ + H_2O \rightarrow H_3O^+ + N_2 \qquad \text{(R 12)}$$

The presence of residual water in the ion source inevitably leads to the formation of clusters according to the process:

$$[(H_2O)_{n-1}H]^+ + H_2O + M \rightarrow [(H_2O)_nH]^+ + M \qquad \text{(R 13)}$$

Where M is a third collision body. These clusters possess higher proton affinities than the bare water molecule (691 kJ mol^{-1} [49]). The dimer already shows a proton affinity of 808 kJ mol^{-1} and the proton affinity further increases with additional water molecules [102].

There are two important consequences by the formation of charged water clusters. First, an increase in the proton affinity of the reagent goes along with an increase in selectivity. All compound classes with lower proton affinity will not be amenable to this CI scheme. In the extreme, large clusters form a thermodynamic sink for protons and eventually render the analytical applicability impossible. Secondly, neutral water can also induce the ligand switching mechanism, which causes water adduct formation according to:

$$H_3O^+(H_2O) + A + M \rightarrow H_3O^+(A) + H_2O + M \quad \text{(R 14)}$$

Considering the ion signal distribution of an analyte for the respective ion source pressures the following pattern was obtained. Figure 40 depicts the protonation, fragmentation, adduct and molecular ion ratios of *o*-xylene.

It is clearly seen, that the degree of fragmentation of *o*-xylene is reduced with increasing pressure. The observed fragments are $C_6H_6^+$, $C_6H_7^+$, $C_7H_7^+$ and $C_8H_9^+$. In the pressure range from 3 to 5.5 mbar, a slight water adduct formation is observed. The $[M+H_2O]^+$ is the main adduct signal in this range.

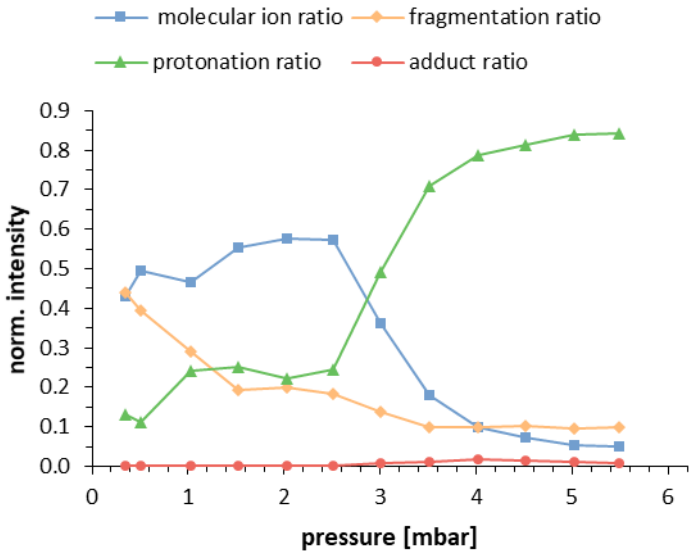

Figure 40: Distribution of protonation, fragmentation, adduct formation and molecular ion ration of *o*-xylene with nitrogen as reagent gas (10.4 %) as a function of the ion source pressure in the range of 0.3 – 5.5 mbar.

The protonation and the molecular ion ratios show opposing trends. Starting at 2.5 mbar the protonation ratio significantly increases with rising pressure, while the molecular ion ratio declines. A look at the characteristic signals of the nitrogen background gas in Figure 39 reveals that 2.5 mbar is the onset of the ion molecule chemistry and the observed ion distribution changes with further increasing pressure. The protonation ratio peaks at the maximum of 5.5 mbar and the signal-to-noise ratio of the protonated *o*-xylene has improved by a factor of 430 compared to the lowest pressure.

Reagent gas: Methane

Classical CI originated from the idea to scale down the degree of fragmentation in electron ionization. In praxis, the same principle of accelerated electrons for primary ionization applies and also the source volume with the heated filament configuration is similar to the ones used in EI, which typically eases the rapid switch between EI and CI. The main difference is the more closed volume in CI. This allows to slightly increase the pressure and initialize an ion chemical cascade starting with electron ionization of an abundant reagent gas, followed by "soft" protonation of the analyte. Methane is by far the most common reagent gas used for classical CI-MS. The positive reagent ions generated upon electron ionization are CH_5^+ and $C_2H_5^+$, which protonate almost all organic molecules. The appearance of methane CI spectra are largely independent of the reagent gas pressures [13, 105].

Clearly, the difference to this work is the mechanism for the reagent ion formation. The expected species formed by the reaction of H_3^+ with methane are protonated methane, CH_5^+, and methyl ions, CH_3^+. It is suggested that the primary proton transfer process leads to the formation of excited $(CH_5^+)^*$, which may either decompose or be stabilized by a third body collision:

$$H_3^+ + CH_4 \rightarrow (CH_5^+)^* + H_2 \quad \text{(R 15)}$$

$$(CH_5^+)^* \rightarrow CH_3^+ + H_2 \quad \text{(R 16)}$$

$$(CH_5^+)^* + M \rightarrow CH_5^+ + M \quad \text{(R 17)}$$

An alternative mechanism is postulated as [106]:

$$H_3^+ + CH_4 \rightarrow CH_3^+ + 2\,H_2 \quad \text{(R 18)}$$

$$CH_3^+ + H_2 \rightarrow CH_5^+ \quad \text{(R 19)}$$

Figure 41 shows a mass spectrum at 0.3 mbar for methane as the reagent gas. As proposed, the expected CH_5^+ (*m/z* 17) and CH_3^+ (*m/z* 15) are present, here with abundances of 49.5 % and 3.2 %, respectively.
These two species, however, contribute only around 50 % to the total spectrum, which already suggests a way more complex chemistry for methane than the one simply sketched in R15 – R19. Additional peaks directly associated with the CH_4 precursor were assigned to $C_2H_5^+$ (*m/z* 29) with 21.7 % abundance, followed by $C_3H_5^+$ (*m/z* 41) (8.4 %), CH_4^+ (*m/z* 16) (6.3 %), $C_2H_3^+$ (*m/z* 27) (3.8 %) and $C_2H_4^+$ (0.4 %). The residual 7 % is basically related to the charged water system.

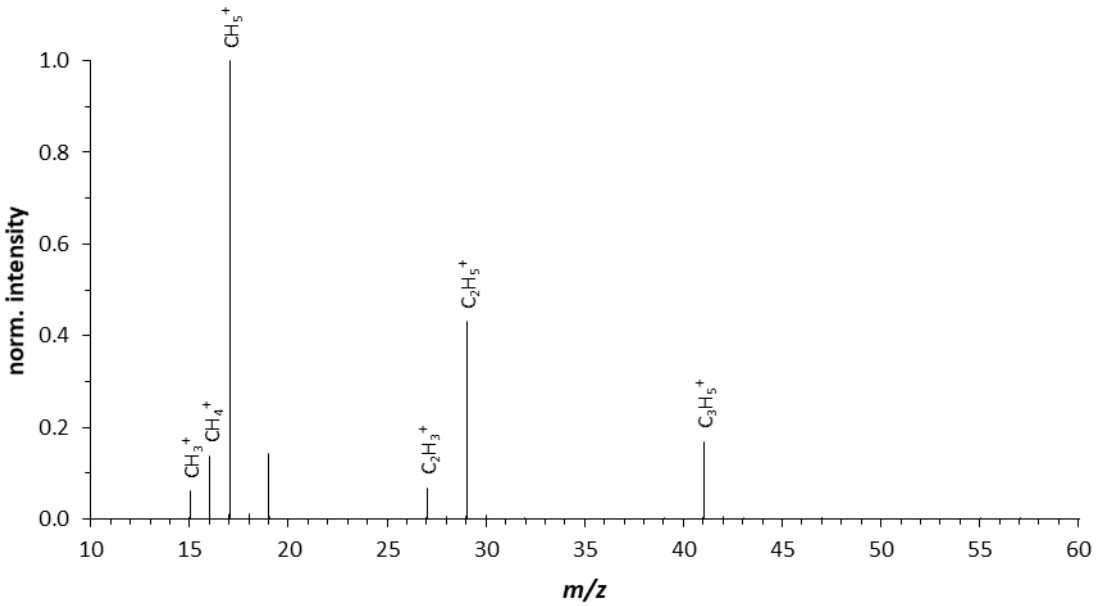

Figure 41: Mass spectrum of 12.8 % methane as reagent gas at 0.3 mbar.

It seems reasonable that $C_2H_5^+$ is the product of a consecutive reaction of CH_3^+ with excess neutral methane [106] according to:

$$CH_3^+ + CH_4 \rightarrow C_2H_5^+ + H_2 \qquad \text{(R 20)}$$

Possible pathways for the other observed species are expressed by the following reactions, which are well-known from classical CI sources:

$$CH_4^+ + CH_4 \rightarrow CH_5^+ + CH_3 \qquad \text{(R 21)}$$

$$CH_2^+ + CH_4 \rightarrow C_2H_4^+ + H_2 \qquad \text{(R 22)}$$

$$CH_2^+ + CH_4 \rightarrow C_2H_3^+ + H_2 + H \qquad \text{(R 23)}$$

$$C_2H_3^+ + CH_4 \rightarrow C_3H_5^+ + H_2 \qquad \text{(R 24)}$$

The main ions CH_5^+ and $C_2H_5^+$ do not further react with methane and the rate coefficient for $C_2H_3^+$ in R 24 is rather low [13]. Following R 22 and R 23 the occurrence of $C_2H_3^+$ (3.8 %) and $C_2H_4^+$ (0.4 %) require CH_2^+. There is no obvious way for its formation based only on the interaction between methane and H_3^+ and it was never observed in any measurements. Instead, it is hypothesized that due to back diffusion at low pressures the rough plasma or plasma afterglow conditions partially interfere in the ion-molecule chemistry. A brief look at the literature shows that the ion distribution in Figure 44 bears close resemblance to a spectrum obtained from a 13.56 MHz discharge directly in methane at pressures from 0.1 to 1 Torr [107].

This supports the assumption that back diffusion effects could lead to the formation of CH_2^+ through, e.g., direct electron ionization. More importantly, Smolinsky *et al*. also found radical and neutral hydrocarbons in their system, in particular acetylene (C_2H_2), ethylene (C_2H_4) and ethane (C_2H_6). This could add an additional rich chemistry with the following reactions to alternatively explain the observations in the present system:

$$H_3^+ + C_2H_2 \rightarrow C_2H_3^+ + H_2 \quad \text{(R 25)}$$
$$H_3^+ + C_2H_4 \rightarrow C_2H_5^+ + H_2 \quad \text{(R 26)}$$
$$H_3^+ + C_2H_4 \rightarrow C_2H_3^+ + 2\ H_2 \quad \text{(R 27)}$$
$$H_3^+ + C_2H_6 \rightarrow C_2H_5^+ + 2\ H_2 \quad \text{(R 28)}$$

Once formed, these ions can follow further known reaction pathways [108]:

$$C_2H_3^+ + CH_4 \rightarrow C_3H_5^+ + H_2 \quad \text{(R 29)}$$
$$C_2H_3^+ + C_2H_6 \rightarrow C_3H_5^+ + CH_4 \quad \text{(R 30)}$$
$$C_2H_4^+ + C_2H_4 \rightarrow C_3H_5^+ + CH_3 \quad \text{(R 31)}$$
$$C_2H_4^+ + C_2H_6 \rightarrow C_3H_7^+ + CH_3 \quad \text{(R 32)}$$

Hence, R25 and R27 provide new ways forming $C_2H_3^+$ without the need of CH_2^+. $C_2H_4^+$ could result from direct photoionization of neutral ethylene. In fact, most of the observed ionic species could be alternatively explained through direct ionization of acetylene (11.4 eV), ethylene (10.5 eV), and ethane (11.5 eV) [109], either via photoionization or charge transfer induced fragmentation processes, or due to reactions with H_3^+ [50, 94].
Figure 42 clearly demonstrates the extended chemistry with methane as the pressure increases to 6 mbar. Compared to the spectrum at 0.3 mbar, higher homologous hydrocarbons show up. These ions are produced through condensation reactions of the type $C_2H_y^+$ with neutral C_2H_y and also $C_3H_y^+$ with CH_y and C_2H_y. The main ions at 6 mbar are $C_4H_9^+$ (*m/z* 57) (26.1 %) followed by $C_3H_5^+$ (*m/z* 41) (14.8 %), $C_3H_3^+$ (*m/z* 39) (9.6 %) and $C_3H_7^+$ (*m/z* 43) (6.6 %). Obviously, even without any analyte present the mass spectrum seems rather complicated. Due to the low purity of the used methane, trace impurities of water even add a level of complexity through hydrocarbon-water adduct and water clusters.

To get more generalized conclusions with regard to the prevailing ion-molecule chemistry, all observed ionic hydrocarbons of the form $C_xH_y^+$ and all water adducts of the form $[C_xH_y+(H_2O)_z]^+$ can be grouped according to the total number of carbon (x) or oxygen (z) atoms.

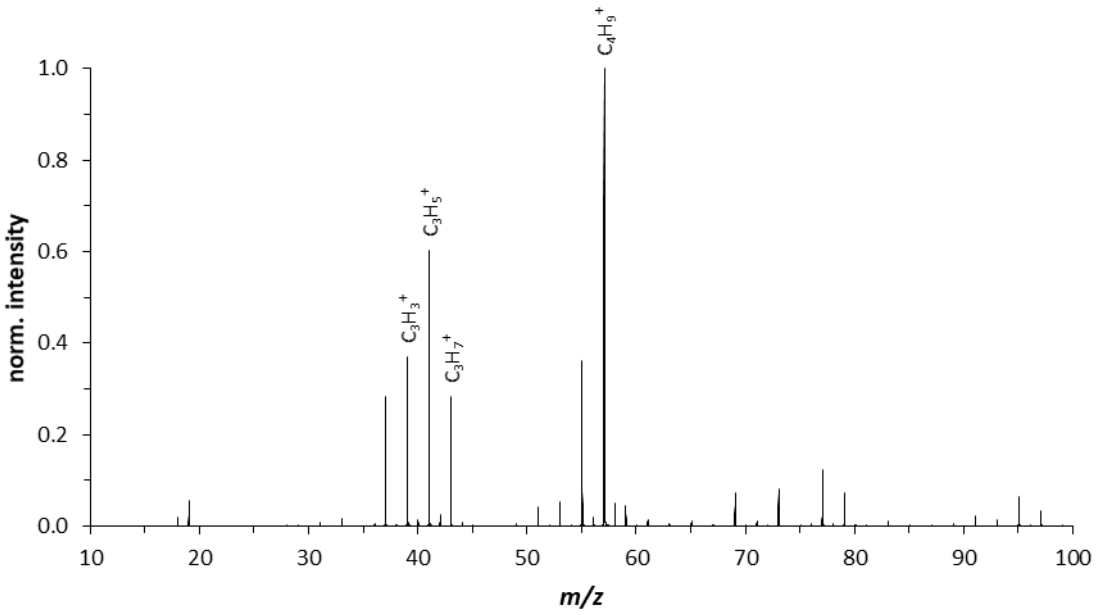

Figure 42: Mass spectrum of 12.8 % methane as reagent gas at 6.0 mbar.

Figure 43 shows these different class distributions as a function of the pressure. For the simplest carbon group $C_1H_y^+$ the exponential decay along with increasing pressure is apparent. The same behavior is indicated by the $C_2H_y^+$ fraction, but the decrease is slightly delayed and sets in at 0.6 mbar. Obviously, the concentration of the lower carbon groups decreases in favor of condensation to higher carbon species, as the probability for bimolecular chemistry is increased. Therefore, the $C_3H_y^+$ and $C_4H_y^+$ fractions steeply rise along with the pressure. The slope of the $C_3H_y^+$ group shows a maximum at around 2 mbar and subsequently falls off, which strongly indicates even further condensation. The other carbon groups with C > 3 steadily increase with pressure. The C_5Hy^+ fraction is an order of magnitude smaller than the $C_4H_y^+$ fraction and the next higher homologous, C_6Hy^+, is proportionately less. Again, these data properly reveal the extensive carbon condensation chemistry with methane as the reagent gas. The picture is similar for the water adduct classes. As the pressure is raised, a consecutive addition of H_2O is observed, starting with the lowest water adduct at 0.3 mbar. At around 4.5 mbar the $[C_xH_y+H_2O]^+$ fraction reaches its maximum, whereas the higher adduct groups show a continuous increase in signal intensity.

To investigate the analytical implications of such a spectrum of potential precursor ions, 2.9 pg *o*-xylene in hexane was injected via the GC. Figure 44 shows the resulting protonation, fragmentation, adduct and molecular ion ratios in relation to the respective source pressure.

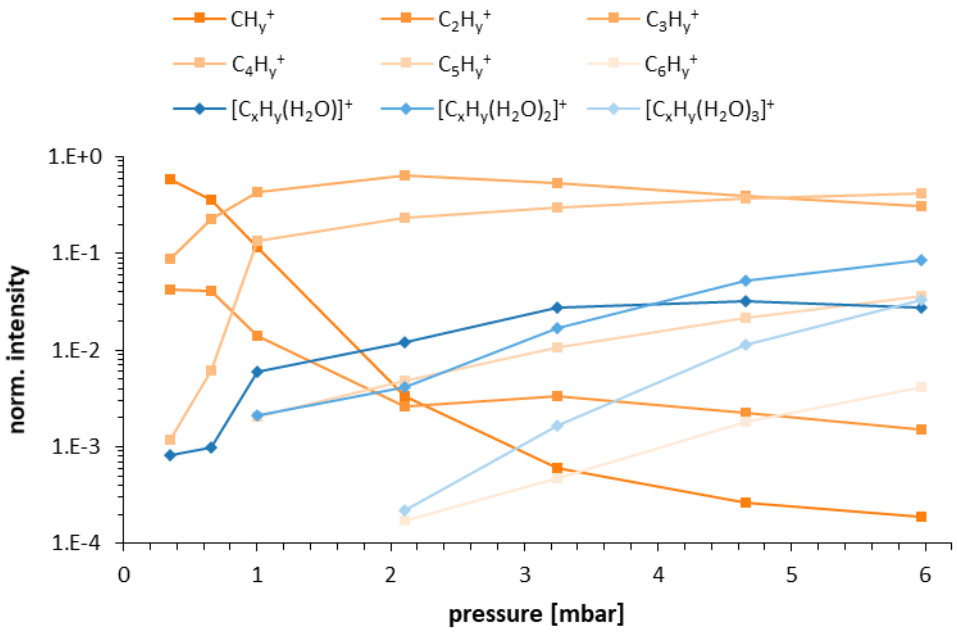

Figure 43: Methane ion signals are grouped according to the number of carbon atoms and water molecules. The graph illustrates their intensity distribution as a function of the source pressure.

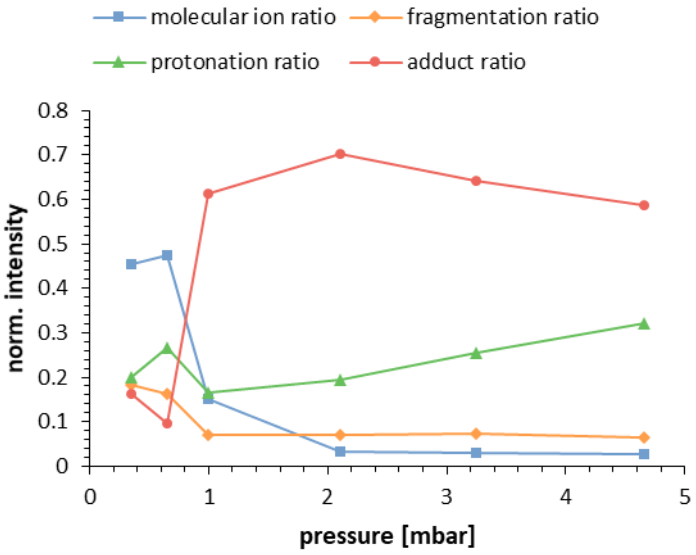

Figure 44: Protonation, fragmentation, adduct and molecular ion ratio of *o*-xylene with methane as reagent gas (12.8 %) as a function of the ion source pressure in the range of 0.3 – 4.6 mbar.

The degree of fragmentation of *o*-xylene initially decreases from 0.3 to 1 mbar sharply and remains constant over the entire pressure range. In contrast to nitrogen as the reagent gas, only the fragments $C_7H_7^+$ and $C_8H_9^+$ were detected. This strongly indicates significantly smoother ionization conditions. The proportion of protonated *o*-xylene steadily increases between 1 to 4.6 mbar. However, the adduct ion signals associated with the higher carbons dominate over almost the entire pressure range. In particular $[M+C_3H_5]^+$, $[M+C_3H_7]^+$, $[M+C_4H_7]^+$ and $[M+C_4H_9]^+$ are amply present, whereas $[M+C_2H_5]^+$ and $[M+C_3H_3]^+$ contribute only negligibly. Figure 45 demonstrates excellent agreement between these pressures related *o*-xylene adducts and the distributions of the corresponding reagent gas ions.

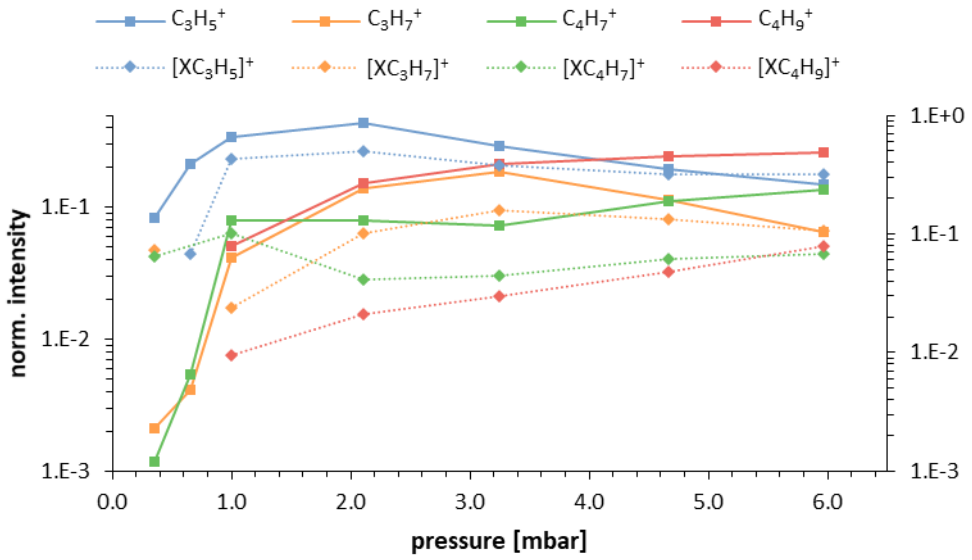

Figure 45: Reagent gas ion signals (left y-axis) and corresponding *o*-xylene (X) adduct signals (right y-axis) as a function of the pressure.

In summary, the ion chemistry in the present source design with pure methane as the reagent gas closely follows the mechanisms known from classical CI. A slight increase of the source pressure significantly alters the resulting mass spectrum, since the rate of secondary ion-molecule reactions substantially go up due to higher collision frequencies as well as longer dwell times. The rather complex mass spectra are a result of many competing and consecutive reactions. The CH_5^+ ion almost vanishes with increasing pressure and new species become more prominent, particularly the stepwise shift to higher carbon species is noticeable. As a consequence of trace water impurities also hydrocarbon-water adducts are present.

Most interestingly, all these potential reagent ions cover a very broad spectrum of proton affinities, ranging from around 550 to 800 kJ mol^{-1} (cf. Table 7) with regard to the main species

CH_5^+, $C_2H_5^+$, $C_3H_5^+$, $C_4H_9^+$. Therefore, the accurate control of this reaction system could provide a promising way for a soft ionization scheme of analytes with similar proton affinities in this range. Certainly, a major drawback of methane is that in its own right it inherently imparts a base intricacy to the mass analysis.

Reagent gas: Isobutane

Isobutane is frequently used as an alternative to methane as a reagent gas in classical CI-MS. The mean proton affinity of generated ions is higher than with methane, which reduces or even eliminates analyte fragmentation upon proton transfer and increases the abundance of intact adduct ions. Isobutane has been used to maximize the sensitivity for certain applications and in cases with identification issues of the protonated analyte molecule [110, 111].
Following the literature, the reaction of H_3^+ and isobutane is expected to primarily form $C_3H_7^+$ and $C_4H_9^+$ [50]. Deuterium-isobutane experiments, however, indicated a direct proton transfer process between H_3^+ and isobutane [106] at first instance.

$$H_3^+ + \textit{iso}\text{-}C_4H_{10} \rightarrow C_4H_{11}^+ + H_2 \qquad \text{(R 33)}$$

Since this reaction is highly exothermic (cf. Table 7) the lifetime of the protonated isobutane is very short and has only a transitory existence, at least under the present experimental conditions. Consequently, $C_4H_{11}^+$ rapidly decomposes to the expected butyl or propyl ions via elimination of hydrogen (R 34) or methane (R 35) [106].

$$C_4H_{11}^+ \rightarrow C_4H_9^+ + H_2 \qquad \text{(R 34)}$$
$$C_4H_{11}^+ \rightarrow C_3H_7^+ + H_2 + CH_4 \qquad \text{(R 35)}$$

Another reported product ion from protonation of isobutane with excited H_3^+ is $C_3H_5^+$ [94].

Figure 46 depicts that the expected $C_4H_9^+$ (*m/z* 57) and $C_3H_7^+$ (*m/z* 43) ions are clearly observed under the present experimental conditions with abundances of 56 % and 13 %, respectively. In addition, two mass peaks with *m/z* 42 and *m/z* 56 substantially contribute to the spectrum with approximately 9 % and 12 % abundance. These masses can be assigned to the radical ions $C_3H_6^+$ and $C_4H_8^+$. Conceivable pathways for their formation are the following fragmentation reactions:

$$\textit{iso}\text{-}C_4H_{10}^+ \rightarrow C_4H_8^+ + H_2 \qquad \text{(R 36)}$$
$$\textit{iso}\text{-}C_4H_{10}^+ \rightarrow C_3H_6^+ + CH_4 \qquad \text{(R 37)}$$

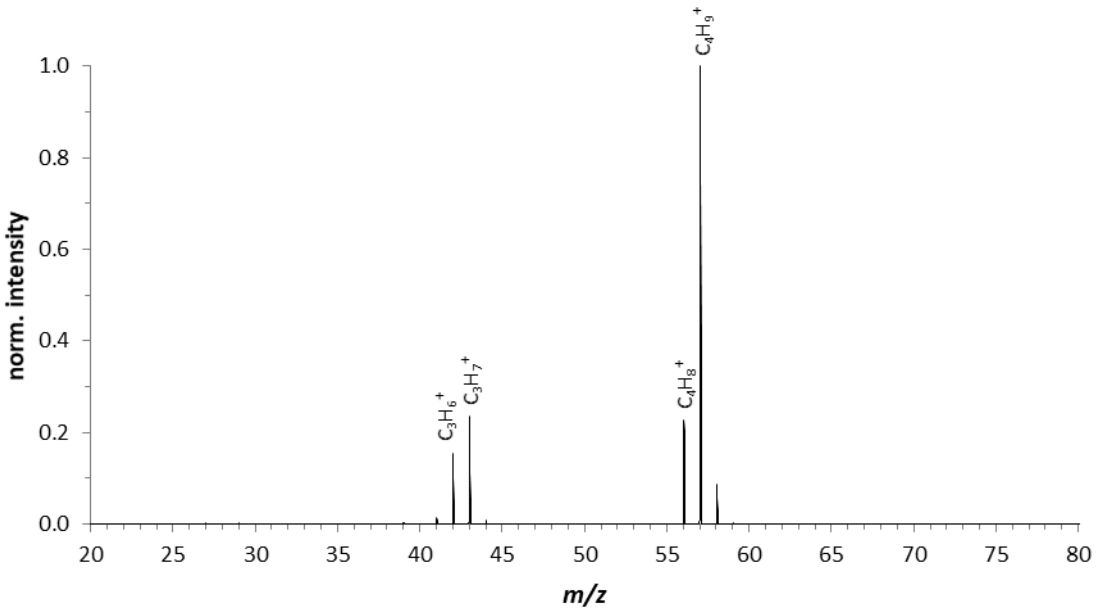

Figure 46: Mass spectrum of 4.9 % isobutane as reagent gas at 0.3 mbar.

These are analogous to R 34 and R 35 describing elimination of hydrogen or methane, but taking the molecular isobutane ion as starting point instead of the protonated. Certainly, this also requires a way for $C_4H_{10}^+$ to be formed. In fact, this ion accounts for up to 3.5 % of the entire mass spectrum, which must result from charge transfer or photoionization.
Several further dissociation pathways from $C_4H_{10}^+$ are known and summarized in Table 8 along with their associated enthalpies of reaction. Interestingly, also the two fragments from the protonated precursor in R 34 and 35 are listed.
Figure 47 provides an overview of all the ionic species from isobutane and their relative distribution as a function of the pressure between 0.3 and 5.5 mbar. The most persistent are $C_3H_6^+$ (*m/z* 42), $C_3H_7^+$ (*m/z* 43), $C_4H_8^+$ (*m/z* 56) and $C_4H_9^+$ (*m/z* 57). From a thermodynamic point of view rather low positive reaction enthalpies relative to the molecular ion of isobutane – all below 0.84 eV - is common to them (cf. solid lines). Other observed minor product ions are $C_2H_3^+$ (*m/z* 27), $C_2H_5^+$ (*m/z* 29), $C_3H_3^+$ (*m/z* 39) and $C_3H_5^+$ (*m/z* 41), with substantially higher reaction enthalpies between 2.56 and 6.18 eV relative to $C_4H_{10}^+$ (cf. dotted lines). These energetic properties are clearly reflected by their intensities. Nevertheless, the appearance of these smaller hydrocarbon homologous again indicates that the reagent gas interacts with the plasma afterglow at lower pressures and is partially ionized under rather harsh conditions. In this context it is also reasonable to assume the formation of neutral hydrocarbons with altered

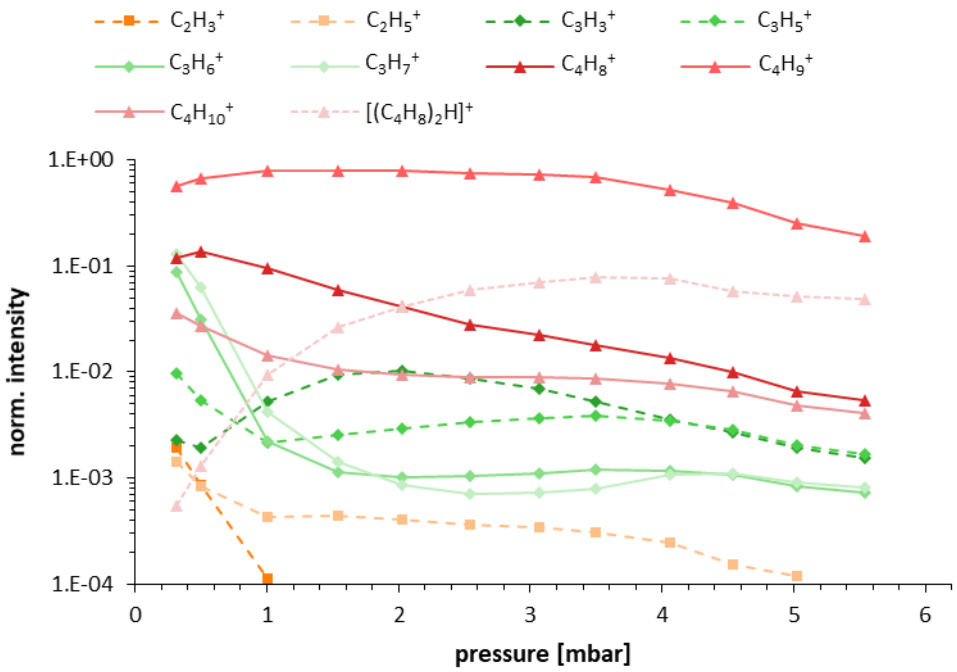

Figure 47: Ion signal distribution as a function of the ion source pressure in the range of 0.3 – 5.5 mbar. (4.8 % isobutane).

carbon number and their subsequent ionization, similar to the processes with methane discussed earlier.

Furthermore, photolysis of isobutane can also contribute to this altered neutral hydrocarbon population. Following a list of some well-known decomposition ways of electronically excited isobutane molecules [112]:

$$iso\text{-}C_4H_{10}^* \rightarrow C_3H_6 + CH_4 \quad \text{(R 38)}$$

$$iso\text{-}C_4H_{10}^* \rightarrow C_3H_8 + CH_2 \quad \text{(R 39)}$$

$$iso\text{-}C_4H_{10}^* \rightarrow sec\text{-}C_3H_7 + CH_3 \quad \text{(R 40)}$$

$$iso\text{-}C_4H_{10}^* \rightarrow C_4H_8 + H_2 \quad \text{(R 41)}$$

Consequently, these processes are likely to occur and could also account for the observed small hydrocarbon $C_2H_y^+$ series and some of the $C_3H_y^+$ ions. Again, these ions do not make an appreciable contribution to the total ion count, though.

It is remarkable how sensitive the propyl ion signals, $C_3H_6^+$ and $C_3H_7^+$, are to changes in the gas density. From 0.3 to 1.5 mbar those collapse by nearly two orders of magnitude. In contrast, the slope indicating the $C_4H_8^+$ population continuously falls off by only one order of magnitude

over the entire pressure range, which is similar to the progression of the molecular isobutane ion (*iso*-$C_4H_{10}^+$) population. Also note that with declining $C_4H_8^+$ inetnsity, the proton bonded dimer $[(C_4H_8)_2H]^+$ population is enhanced. The butyl ion $C_4H_9^+$ shows an opposing trend. First, the signal slightly increases until 2.5 mbar and then slowly decreases. Partially responsible for those observations are probably the secondary reactions of $C_3H_7^+$ or $C_3H_6^+$ with excess neutral isobutane in form of H^- or H_2^- transfer reactions [112]:

$$C_3H_7^+ + \textit{iso}\text{-}C_4H_{10} \rightarrow C_4H_9^+ + C_3H_8 \quad \text{(R 42)}$$

$$C_3H_6^+ + \textit{iso}\text{-}C_4H_{10} \rightarrow C_4H_8^+ + C_3H_8 \quad \text{(R 43)}$$

$$C_3H_6^+ + \textit{iso}\text{-}C_4H_{10} \rightarrow C_4H_9^+ + C_3H_7 \quad \text{(R 44)}$$

These provide a reasonable explanation for the dramatic drop of the $C_3H_7^+$ and $C_3H_6^+$ populations and the initially slight increase in $C_4H_9^+$.

Similar to the methane experiments, the low purity of the used isobutane induced water adduct formation, more pronounced with rising pressure. In particular the $C_3H_5^+$ population seemed to be strongly affected, as illustrated in Figure 48.
Additional species with oxygen were identified, such as $C_4H_9O^+$, $C_7H_{15}O^+$, $C_6H_{13}O_2^+$ and $C_8H_{18}O_2^+$. It seems reasonable to suppose that those are of the hydrocarbon-water cluster type as well. However, they were not unambiguously assigned since the corresponding unclustered ions were not observed, accordingly the simple molecular notation was chosen.
Moreover, reactions of neutral alkanes formed during fragmentation processes (cf. Table 8 and R 30 - 32) with protonated water cannot be excluded.
Whatever way the water finds to participate in the ion chemistry, its impact drastically increases with the gas density, as illustrated by the exponential progression of nearly all slopes in Figure 48.

Table 8: Possible decomposition reactions of isobutane and their enthalpies.

Decomposition	**Enthalpy [eV]**		
iso-$C_4H_{10}^+$	Observed[a]	Calculated[a]	Calculated[b]
→ t-$C_4H_9^+$ + H	0.5	0.7	0.84
→ $C_4H_8^+$ + H_2			0.18
→ $C_4H_8^+$ + 2 H			4.96
→ $C_3H_7^+$ + CH_3	0.4	0.5	0.84
→ $C_3H_6^+$ + CH_3 + H			4.85
→ $C_3H_6^+$ + CH_4			
→ *c*-$C_3H_5^+$ + CH_3 + H_2	2.5	2.6	2.56
→ $C_3H_3^+$ + CH_3 + H_2 + 2 H	6.8	7.8	
→ $C_3H_3^+$ + CH_3 + 4 H	11.2	12.3	
→ $C_3H_3^+$ + CH_3 + 2 H_2			5.34
→ $C_2H_6^+$ + C_2H_4			2.18
→ $C_2H_5^+$ + C_2H_4 + H	3.0	3.1	
→ $C_2H_5^+$ + C_2H_5			1.69
→ $C_2H_5^+$ + CH_3 + CH_2	6.0	5.8	6.18
→ $C_2H_5^+$ + C_2H_3 + 2 H	8.8	7.7	
→ $C_2H_5^+$ + 2 CH_2 + H	12.8	10.7	
→ $C_2H_3^+$ + CH_4 + CH_3	3.5	3.1	
→ $C_2H_3^+$ +2 CH_3 + H	6.5	7.6	8.46
→ $C_2H_3^+$ + 2 CH_2 + H_2 + H	12.8	12.9	
→ $C_2H_3^+$ + C_2H_5 + H_2			4.29
→ $C_2H_3^+$ + C_2H_4 + CH_3			3.62

[a] Ref. [113]; [b] Ref. [114]

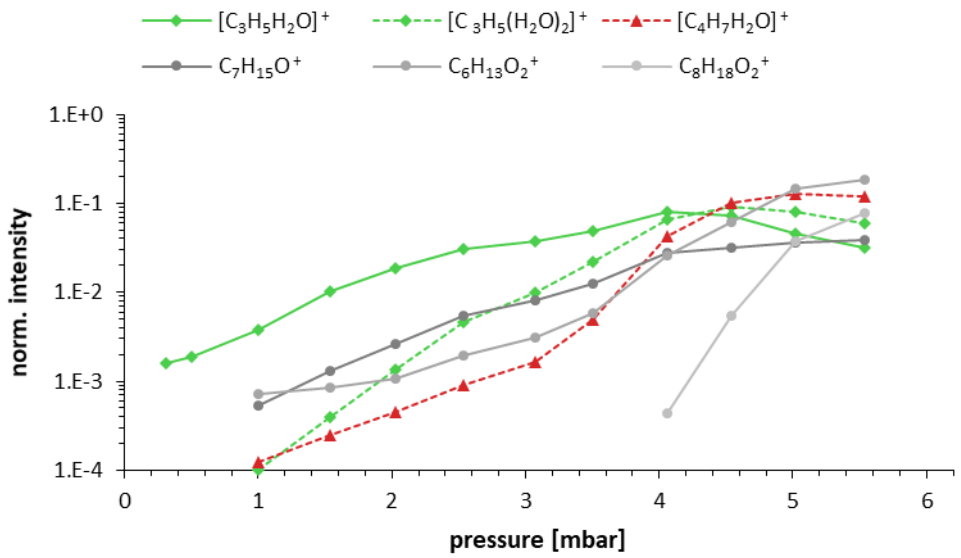

Figure 48: Water adduct ion signal distribution as a function of the ion source pressure in the range of 0.3 – 5.5 mbar with isobutane as reagent gas (4.8 %).

Compared to the plots of *o*-xylene with nitrogen and methane as reagent gas (cf. Figure 40 and Figure 44), it is noticeable that in this case the protonated α-pinene dominates the spectrum over the entire pressure range. The signal-to-noise ratio of the $[M+H]^+$ even increases along with the gas density and is improved by at least a factor of 20. Interestingly, the protonation and fragmentation curves each show two distinct maxima, with an apparent inverse progression. Starting from 0.3 mbar the protonation ratio rises, reaches its first maximum at about 2 mbar and subsequently decreases. At 4 mbar the second positive incline sets in and levels off at the same intensity as the previous maximum. As mentioned, the progression of the fragmentation curve is exactly inverse. The reason for this behavior remains open to speculation, as does the overall pronounced fragmentation ratio. In the reagent gas spectrum no ion species was identified that essentially correlates (cf. Figure 47) with the described protonation and fragmentation trends to explain these results.

As seen, the entire reaction system with isobutane is rather complex and not all reaction channels of each individual ion were clarified. Too many parameters changed depending on the pressure. Nevertheless, some general trends were observed. Over the whole pressure

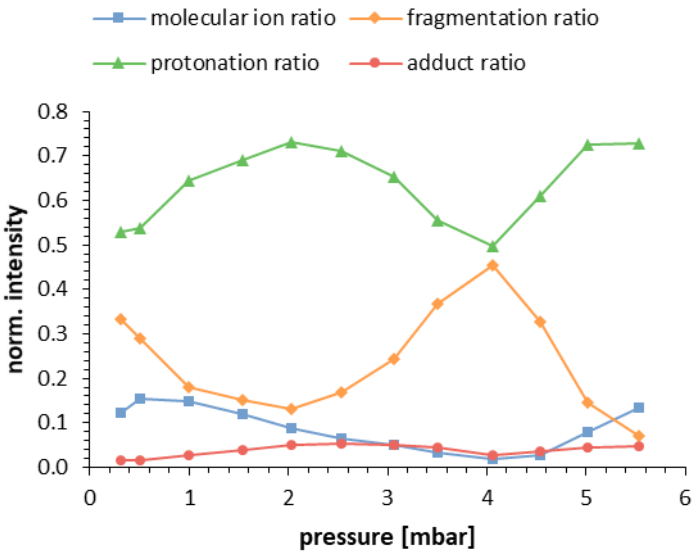

Figure 49: Protonation, fragmentation, adduct , and molecular ion ratios of α-pinene with isobutane as reagent gas (4.8 %) in dependency of the ion source pressure in a range from 0.3 – 5.5 mbar.

range $C_4H_9^+$ dominates the spectrum by nearly an order of magnitude. With increasing gas density and reaction time, proton bonded dimers and water adducts form in growing amount. In this context, it should be noted that with higher pressure not only the total collision number increases, but also the required termolecular event for water attachment will be more likely.

All three reagent gases under investigation showed water cluster or water adduct related ion signals. With increasing ion source pressure, longer dwell times and reaction times these signals were shifted to larger water containing clusters or adducts. The larger the cluster, the lower the ability to protonate and the analytical performance will be reduced. The water content can partly be attributed to the low purity of the used reagent gases (methane, isobutane). This clearly illustrates that great attention should be paid to their cleanliness.
Comparing the three reagent gases, nitrogen showed by far the least complex reaction system. As expected, mainly N_2H^+ was observed. With its relatively low proton affinity of 493.8 kJ mol^{-1} it enables proton transfer ionization for a wide range of analytes.
In contrast, the studied ion chemistry of methane and isobutane proved to be much more complicated. While isobutane primarily formed *t*-$C_4H_9^+$ and only minor other ionic hydrocarbon species, methane showed a quite different picture. Here the ion distribution substantially changed with increasing gas density. Initially, mainly CH_5^+ and $C_2H_5^+$ were present, however, extensive ion-molecule reactions promote the population of $C_2H_y^+$ and $C_3H_y^+$ species. Even higher homologous were found and attributed to condensation reactions

between $C_2H_y^+$ ions and C_2H_y neutrals, and between $C_3H_y^+$ ions and C_1H_y and C_2H_y neutrals. The major higher homologous ions were $C_3H_5^+$ and $C_4H_9^+$. Considering the whole pressure range, the respective observed main ions span proton affinities from approximately 500 – 800 kJ mol^{-1}.

Concerning the capability of the various reaction systems to ionize a given substance, exemplary tests with one analyte yielded similar results for each reaction system. The protonation ratio increased along with the pressure. The fragmentation ratio of the respective analytes showed an opposing trend, which indicates growing effects of the plasma afterglow at lower gas densities.
In terms of sensitivity the most efficient operating point of the studied ion source setup seemed to be at elevated pressure of around 5 – 6 mbar. The signal-to-noise ratios of the respective protonated analyte signals increased with higher pressure for all three reagent gases. With nitrogen the S/N ratio could be increased by a factor of 430, with methane by a factor of 105 and with isobutane as reagent gas by a factor of 20.
The observed analyte-adduct ion signals correlated with the respective reagent ion background spectra, indicating that the species are accessible to reactions with the neutral analyte during their dwell time in the reaction tube and that these reactions are sufficiently fast. The whole analyte ionization process is very dynamic and proceeds during the entire dwell time. By decoupling the reagent ion formation from the analyte ionization and precise adjustment, e.g. for the methane reagent gas system, it could bear the potential to cover a wide range of reagent ion proton affinities with only one reagent gas. This could be achieved by physically separating the reagent gas addition from the analyte introduction into the ion source. By adding only a certain amount of methane, for example, the reaction system could be driven in such a way that the preferred main reagent ion species is present when the analyte is added further downstream.

4.6.2 Analyte Ionization

This section focuses on the qualitative characterization of the ion source Design 3 (cf. Figure 9) in terms of fragmentation, adduct formation and selectivity for various analytes in combination with different reagent gases. For this purpose, *n*-decane, *o*-xylene, anisole and α-pinene were chosen as analytes. They cover a range of proton affinities from 690.4 to 878.6 kJ mol^{-1} (cf. Table 7). In particular *n*-decane, representing the analytical class of alkanes, and α-pinene are valuable indicators for pronounced fragmentation conditions. As reagent gases nitrogen, methane and isobutane were used. Those systems were studied in detail in the previous chapters and it was shown that the multitude of ionic species provides a large spectrum of proton affinities. To a certain extent, hands-on control of this chemistry might allow to promote a particular ion population for a tailored protonation event with the analyte. Essentially, a way to adjust the degree of fragmentation, selectivity and sensitivity. A parameter for this control, besides the much-discussed pressure regulation in the previous chapter, is the dilution of the reagent gas prior to the introduction into the ion source. In the following experiments the reagent gases methane and isobutane were diluted with nitrogen or argon at a pressure of approximately 6 mbar. Besides helium and neon, argon is one of the few gases with a lower proton affinity than H_2, which renders Ar almost inert towards reactions with H_3^+. Exceptions are the following two pathways described in [94, 96]

$$H_3^+ + Ar + H_2 \rightarrow ArH_3^+ + H_2 \qquad \text{(R 45)}$$

$$H_3^+{}_{(\upsilon > 1)} + Ar \rightarrow ArH^+ + H_2 \qquad \text{(R 46)}$$

R 45 is a relatively slow third-order reaction with a rate coefficient of $1 \cdot 10^{-31}$ cm^6 $molecule^{-2}$ s^{-1} and R 46 may only occur with vibrationally excited H_3^+. Moreover, whether ArH^+, ArH_3^+, nor any other Ar_xH_y corresponding ion signals were noticed throughout these experiments. Consequently, both reactions are rather unlikely to occur, which allows the observation of the direct interaction between the reagent gas ion species and the analytes, despite the presence of argon. Another reason for choosing argon is its physical properties (e.g. viscosity), which maintain the pressure of around 6 mbar, without significantly affecting the pressures in the downstream differentially pumped stages of the mass spectrometer.

Three mass spectra of different isobutane mixtures are shown in Figure 50 to illustrate the dilution effect of the reagent gases. The upper spectrum depicts pure isobutane and is characterized by a multitude of species, along with a broad distribution of gas phase acidities. For a detailed discussion the reader is referred to the respective section of chapter 4.6.1. Remarkably, the addition of > 75 % nitrogen or argon to the reagent gas caused a substantial

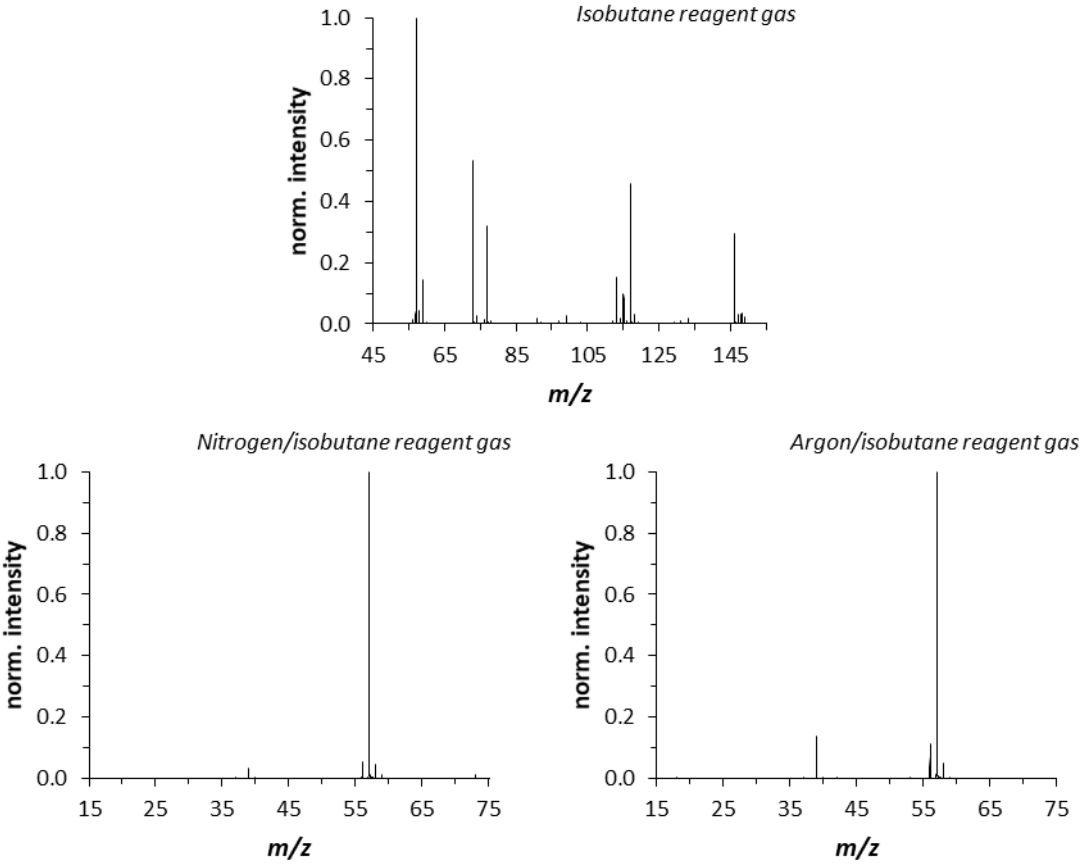

Figure 50: Mass spectrum of different reagent gas mixtures. *Upper spectrum:* pure isobutane at 5.4 mbar. *Lower left spectrum:* nitrogen and isobutane (5.6/0.4) at 6.22 mbar. *Lower right spectrum:* argon and isobutane (3/1) at 6.0 mbar.

shift towards one single species, the *t*-$C_4H_9^+$ (*m/z* 57) ion, which contributed 92 % to the total ion current (cf. lower left and right spectra). In this way the overall acidity of the protonating gas was reduced from a broad range to virtually a single value of 802.1 kJ mol^{-1} [49].

Similar clearing effects and shifts upon dilution were observed with methane. In pure condition $C_4H_9^+$ was the main ion with 22 % and the residual signals were apportioned among 14 other relevant species (cf. Table 20, appendix). Addition of 91 % argon apparently shifted the distribution to lower carbon homologous and also less water adducts were formed. Here, the main species corresponded to $C_3H_5^+$ with 32 % relative intensity and the residual ion current was assigned to only nine different species.

It should be noted, however, that in the present CI-design the GC effluent and the reagent gas addition share the same inlet port. This means that the protonating agents observed in the mass spectrum might significantly differ from the distribution effectively interacting with the

neutral analyte. As seen from the pressure variation measurements in chapter 4.6.1 this is a highly dynamic system with strongly changing ion distributions along the way to the MS.

For a general overview, all major ions and their fractional abundances for different reagent gases and gas mixtures are listed in Table 20 in the appendix
In the following only the analytes α-pinene and *n*-decane will be discussed in more detail.

n-Decane

As expected, *n*-Decane was ionized only by nitrogen and methane reagent gas mixtures. Protonation with isobutane and its main ion *t*-$C_4H_9^+$ is endothermic by around 112 kJ mol^{-1} and was not observed, accordingly. Figure 51 depicts mass spectra of *n*-decane using nitrogen, methane and argon/methane mixtures as reagent gases. The relative intensities of all assigned *n*-decane signals are listed in Table 9. It is clearly seen that with nitrogen (upper spectrum) pronounced fragmentation occured (72 %) in comparison to the methane mixtures (lower left and right spectrum). The latter is characterized by an abundant $[M-H]^+$ ion population, which accounts for 65 - 90 % of the total analyte signal. The $[M-H]^+$ species originates from nominal hydride ion abstraction.
The mass spectrum with argon/methane also shows lower mass alkyl ions, which most likely originate from both fragmentation of the $[M-H]^+$ ion and nominal alkyl ion abstraction reactions [6]. Adduct ions appeared only to a minor extend. However, it is noticeable that with the argon/methane mixture significantly more fragmentation was observed than with pure methane. This is readily explained by the fact that in pure methane the reaction system forms higher homologous alkyl ions with larger proton affinities relatively fast. In contrast, diluting the reagent gas with argon the reaction system is shifted to smaller homologous alkyl ions with lower proton affinities at the point of analyte introduction. This experimental finding generally supports the idea of a more or less in-situ adjustable proton affinity of the reagent by careful regulation of its concentration.

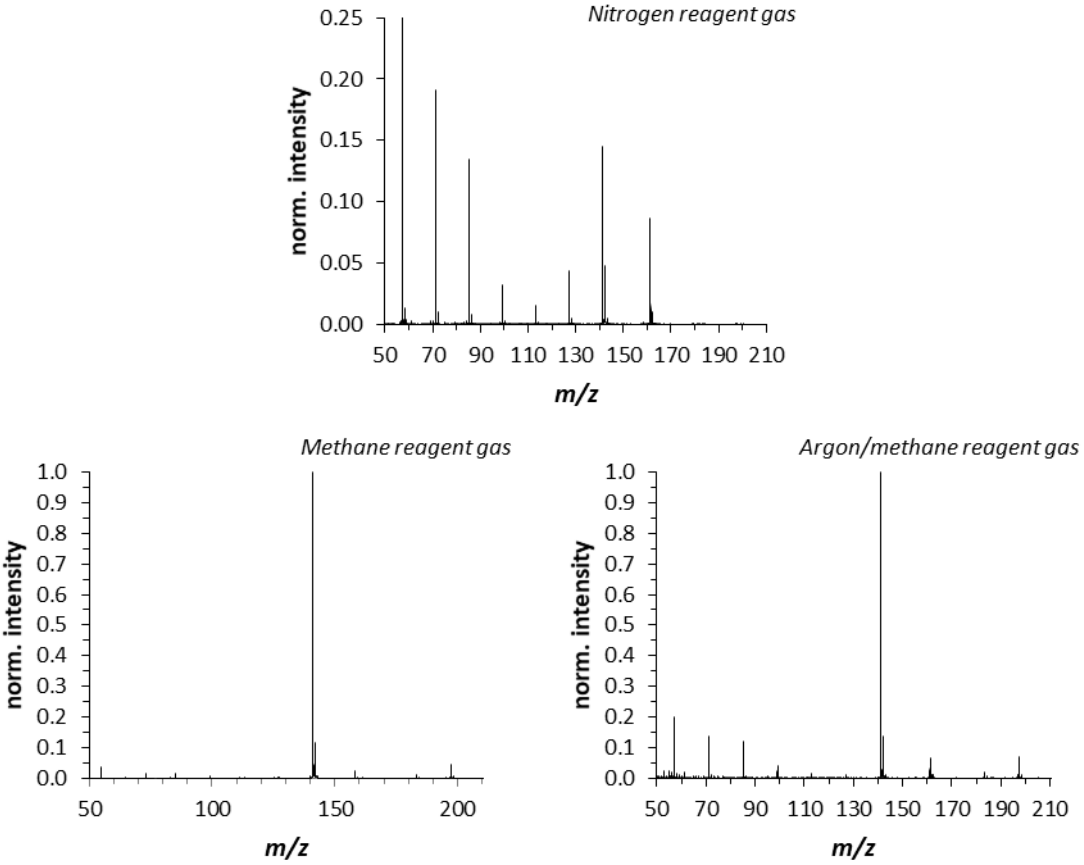

Figure 51: Mass spectra of *n*-decane, using different reagent gas mixtures. *Upper spectrum:* nitrogen. *Lower left spectrum:* pure methane. *Lower right spectrum:* Argon/methane mixture (4/0.4).

Table 9: Fractional abundance of *n*-decane corresponding ion signals for different reagent gas mixtures.

Ionic species	***m/z***	**Fractional abundance**		
Reagent gas:		*Nitrogen*	*Methane*	*Argon/Methane*
$C_4H_9^+$	57	34.6	-	7.0
$C_5H_{11}^+$	71	16.1	-	6.2
$C_6H_{13}^+$	85	11.8	1.3	6.0
$C_7H_{15}^+$	99	3.3	-	2.4
$C_8H_{17}^+$	113	1.7	-	1.0
$C_9H_{19}^+$	127	4.5	-	0.8
$[M-H]^+$	141	1.7	89.6	65.2
$[M+CH_4]^+$	158	-	2.5	-
$[M+H_3O]^+$	161	11.0	-	4.8
$[M+C_3H_5]^+$	183	-	1.7	1.6
$[M+C_4H_7]^+$	197	-	4.9	5.0

α-Pinene

α-Pinene was ionized by all three reagent gases and mixtures under investigation. The obtained mass spectra are shown in Figure 52. As expected, the degree of fragmentation decreases significantly from nitrogen (55.8 %), methane (38.1 %) to isobutane (6.7 %). This correlates with the excess energy calculated according to the difference in proton affinities of the respective reagent ion and the analyte. Once again, lower excess energy implies less fragmentation.

Regarding the reagent gas dilution experiments of methane with nitrogen or argon, the same trend as for *n*-decane was observed. Higher dilution leads to a lower extent of self-reactions of the reagent gas and consequently a lower mean proton affinity at the point of the analyte inlet. This causes the fragmentation ratio of α-Pinene to significantly increase (cf. Table 10). Moreover, fragmentation is more pronounced by diluting with argon than with nitrogen. This result is not quite clear and leaves room for speculation, such as charged intermediate Ar/N_2 species, directly involved in the analyte ionization process. However, no mass spectrometric proof of such intermediates was possible with the present setup.

It should be noted that similar observations were made with other analytes, e.g. *o*-xylene in combination with isobutane as the reagent gas, as well. Since the proton affinity of *t*-$C_4H_9^+$ is only slightly higher compared to that of *o*-xylene, the adduct ion is expected to predominantly be formed. This applies to pure isobutane as reagent gas, however, with an argon or nitrogen dilution a small amount of the protonated o-xylene specie is seen.

To compare and evaluate the used reagent gases, Table 10 gives an overview of the fragmentation, adduct formation, protonation and molecular ion ratios for each analyte and reagent gas combination. It was shown that by the proper choice of a reagent gas the ratio of fragmentation can be reduced and a selective ionization can be obtained. This is beneficial for non-target analyses, as it limits the number of potential compounds and gives the molecular mass information.

Using methane as reagent gas a large number of charged hydrocarbon species are formed due to ion transformation processes with methane itself. Those cover a broad range of proton affinities. It was demonstrated, at least as a preliminary result that due to dilution of the reagent gas the dynamic reaction system can partly be shifted. This provides certain control of the formed reagent gas species and thus the active mean proton affinity at the point of the analyte inlet. In this way the proton affinity becomes an adjustable parameter by simply regulating the concentration of just one reagent gas. Furthermore, this could be done in-situ, e.g. in one GC run to precisely adjust the ionization conditions for each eluting compound separately.

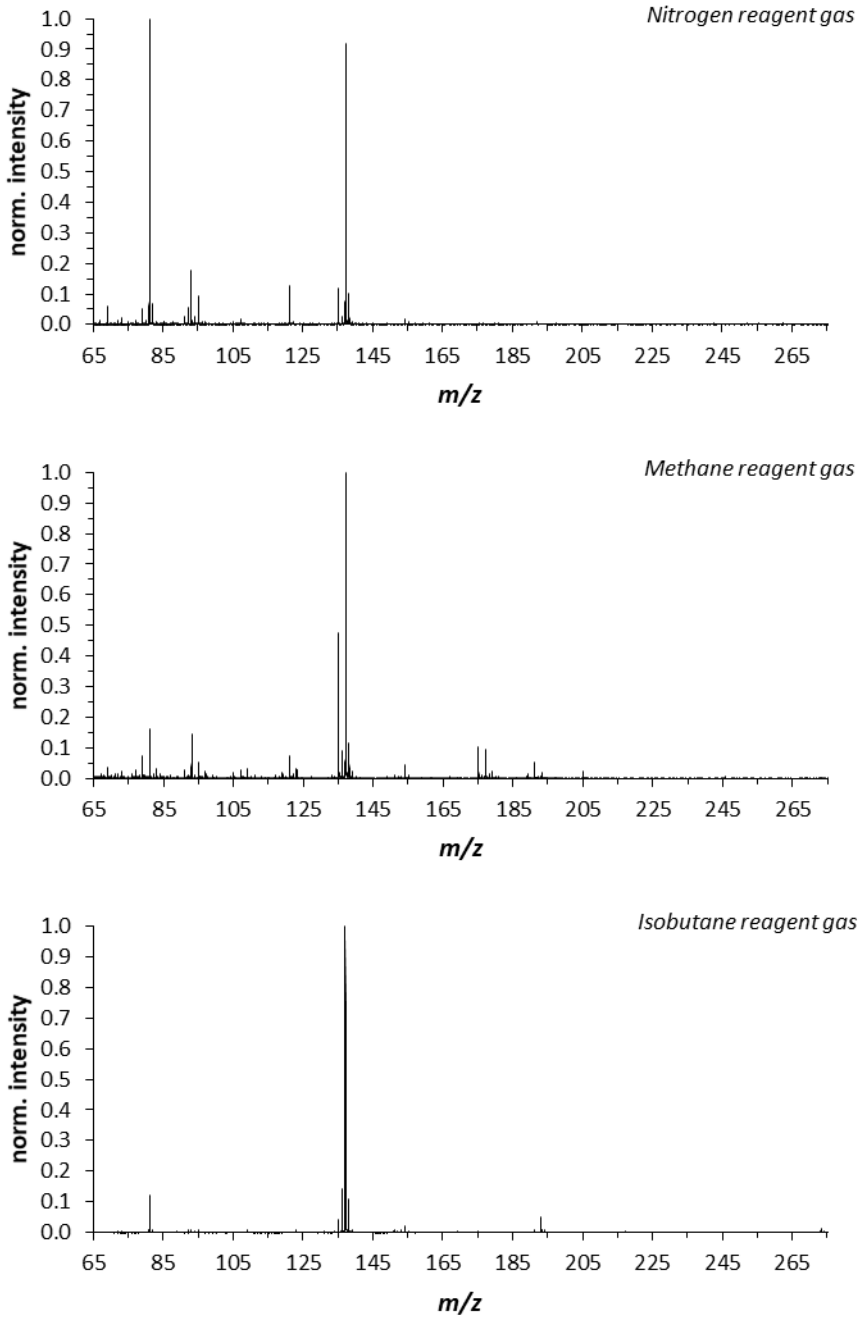

Figure 52: Mass spectra of α-pinene using different reagent gas mixtures. *Upper spectrum:* nitrogen. *Middle spectrum:* pure methane. *Lower spectrum:* pure isobutane.

Table 10: Overview of different reagent gases with some selected analytes.

Analyte	Protonation ratio [%]	Fragmentation ratio [%]	Adduct ratio [%]	Ratio of M^+ [%]	S/N = 3** [pg on column]
Reagent gas:		*Nitrogen*			
α-pinene	37.2	55.8	0.7	2.9	0.85
anisole	86.1	8.6	-	5.3	0.11
o-xylene	81.5	14.1	-	4.4	0.30
n-decane	17.0	72.0	11.0	-	3.12
Reagent gas:		*Methane*			
α-pinene	40.0	38.1	19.0	2.9	0.66
anisole	30.3	-	66.9	2.9	1.69
o-xylene	34.0	3.8	59.8	2.5	1.79
n-decane	89.6*	1.3	9.1	-	0.84
Reagent gas:		*Argon + Methane*			
α-pinene	20.3	64.5	12.7	2.5	4.70
anisole	37.1	-	55.6	7.3	4.24
o-xylene	39.5	12.6	44.0	3.9	1.89
n-decane	65.2*	23.5	11.4	-	2.72
Reagent gas:		*Isobutane*			
α-pinene	71.3	6.7	8.8	9.9	2.51
anisole	30.7	-	38.1	31.1	37.37
o-xylene	-	-	92.6	7.4	23.73
n-decane	-	-	-	-	-
Reagent gas:		*Nitrogen + Isobutane*			
α-pinene	46.1	26.4	12.9	9.5	6.41
anisole	37.7	-	39.0	23.3	3.89
o-xylene	-	-	71.1	28.9	4.51
n-decane	-	-	-	-	-
Reagent gas:		*Argon + Isobutane*			
α-pinene	45.7	37.9	7.2	4.1	5.97
anisole	53.3	-	37.3	9.4	6.30
o-xylene	6.9	-	76.8	16.3	5.93
n-decane	-	-	-	-	-

*ratio of $[M-H]^+$; ** regarding the observed main ion species

However, this still requires further research. In a next ion source iteration the reagent gas inlet should be explicitly separated from the analyte addition. This could more precisely enable the chemistry of the reagent system to be driven to a certain main ionic species with a defined proton affinity at the analyte inlet.

4.7 Analytical Performance

In the following chapters, the analytical performance of the developed ion sources Designs 3 and 4 will be discussed. Especially the chromatographic performance in terms of peak shape, peak broadening and chromatographic time resolution is characterized and compared.
Analytical parameters, e.g. linear dynamic range and limit of detection (LOD) are preliminarily investigated with only a small set of selected analytes and nitrogen as reagent gas. In future work, the analytical capability of the developed ion source will be investigated in more detail with regard to various compound classes and reagent gases. This work focused on the ion source development from scratch.

4.7.1 Heating

To keep the high chromatographic time resolution of a GC system, an ideal ion source should provide an uniform temperature profile. This prevents the condensation of low volatile analytes on the ion source surface and avoids cold spots, which cause peak-tailing and subsequent loss of chromatographic resolution. This requires source temperatures of up to 300 °C whilst maintaining appreciable vacuum conditions even after numerous cooling and heating cycles. At these temperatures special care should also be taken of feasible outgassing from any built-in component and sealing material to keep the matrix as clean as possible. For this purpose, graphite as sealing material is tested with the ion source setup 3. The ion source was heated up to 300 °C and baked out for 48 h under standard operating conditions using nitrogen as reagent gas.
In Figure 53 the background mass spectrum at an operating temperature of 300 °C using graphite gaskets is compared to the mass spectrum operating at room temperature using o-ring sealings. Comparing these two mass spectra, it can be seen that at elevated temperature, in addition to the main signals corresponding to protonated water (H_3O^+, *m/z* 19) and protonated nitrogen (N_2H^+, *m/z* 29) other impurities appear. These signals can be assigned to carbon compounds. Also, an O_2^+ (*m/z* 32) signal is present which indicates a leakage of the source.

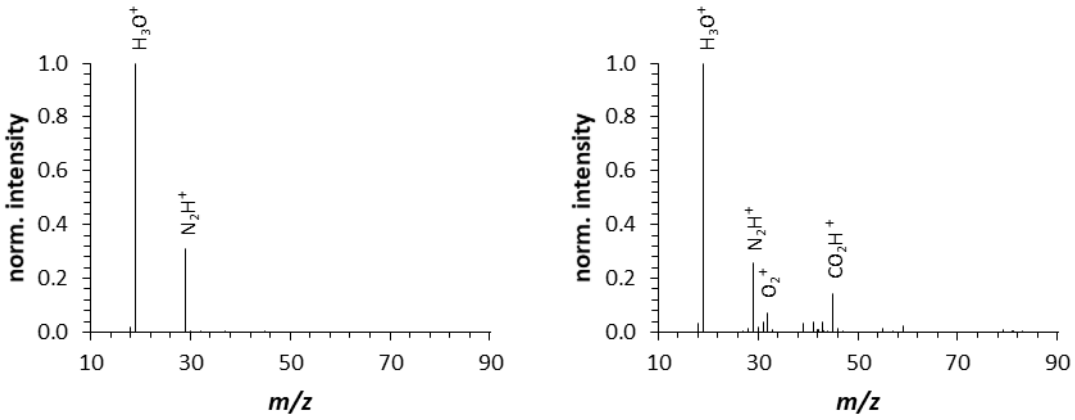

Figure 53: Comparison of the background mass spectra of ion source setup version 3 using nitrogen as reagent gas heated up to 300 °C using graphite sealing (*right spectrum*) and at room temperature using o-ring sealing (*left spectrum*).

Figure 54 depicts the respective logarithmic scaled background mass spectra. Those clearly show that at elevated temperature the background significantly increases. GC measurements with different analytes indicate a decrease of the corresponding signal-to-noise ratios by a factor of 50 with the heated source version. Regarding analyte fragmentation, the ratio of the fragment ion (*m/z* 91) to the protonated molecular ion (*m/z* 93) of toluene is tripled. This points to an increase in other ionization pathways, e.g. charge transfer via O_2^+.

After several heating and cooling cycles the background remained the same and the O_2^+ signal remained constant. This suggests that the leakage was not further affected by these cycles and does not contribute to the different thermal expansion coefficients of the combined materials, but is attributed to the porosity of the graphite. Hence, in the next iteration graphitized Vespel is used, which demands more precise tolerances [115] due to the limited compressibility of these composite materials.

However, if not otherwise stated, measurements discussed in this thesis obtained with the ion source Design 3, the source was sealed with o-rings instead of graphite gaskets, and not heated. As mentioned above, with the ion source Design 4 graphite/Vespel sealings were used. These ferrules exhibit considerably better sealing performance. The obtained background mass spectrum revealed no significant amounts of ionic species, which would indicate a leakage (cf. Figure 31). These sealings remained leak-proof even after multiple heating and cooling cycles.

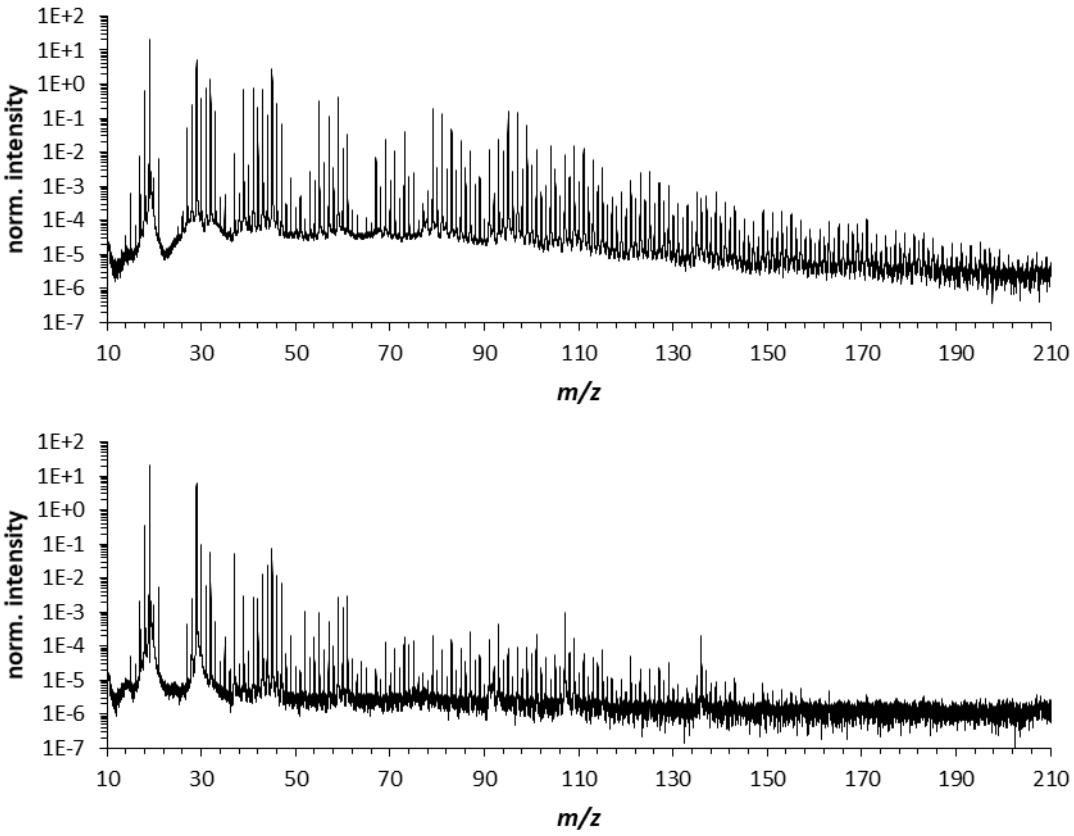

Figure 54: Comparison of the background mass spectra of ion source setup version 3 with graphite sealings using nitrogen as reagent gas and heated up to 300 °C (*upper spectrum*), and at room temperature using o-ring sealing (*lower spectrum*).

The logarithmic scaled background mass spectrum obtained with this ion source is shown in Figure 55. The operating ion source temperature was kept at 250 °C. Note that this spectrum was obtained with different ion transfer and operating parameters compared to the previous spectra, leading to different main background ion species. These are (i) the first three water species - H_3O^+ to $[(H_2O)_3H]^+$ (ii) the proton-bound nitrogen cluster N_4H^+ and the protonated nitrogen species N_2H^+.

Beside these main signals, other impurities appeared, again assigned to carbon compounds according to their characteristic signal pattern. Compared to the previous ion source version, the SSQ was passively heated by the emitted heat from the SSQ enclosure. This could lead to outgassing of the solder or PEEK material inside the SSQ and needs to be investigated in future studies. Nevertheless, an enhancement of the source design was clearly obtained with this iteration regarding lower leakage and an improved control of the reagent gas reaction system.

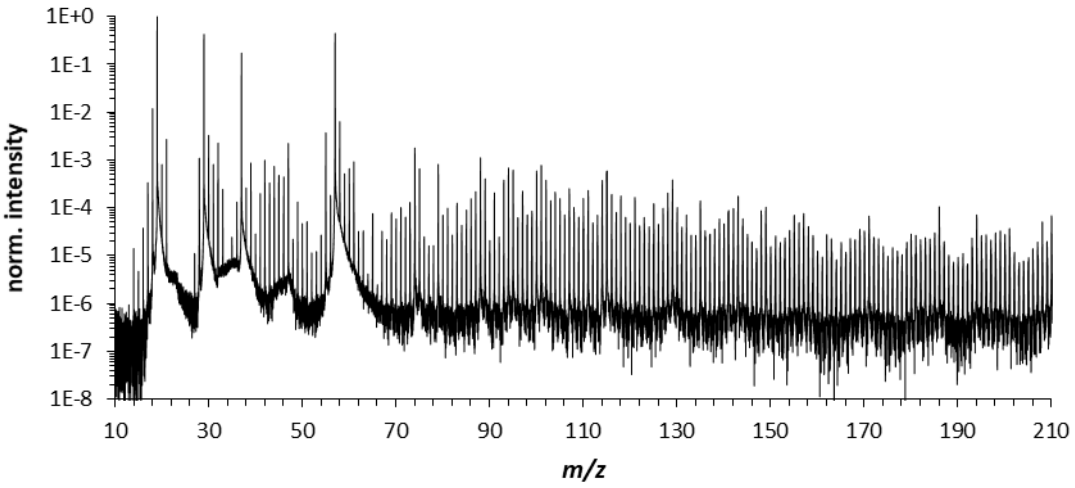

Figure 55: Background mass spectrum obtained with the chemical ionization source Design 4, with 100 sccm H_2 plasma gas flow, 200 sccm N_2 as reagent gas and 1.2 sccm He as GC carrier gas at 13 mbar. Ion source temperature 250 °C. Ion transfer settings cf. Table 18 #3 (appendix).

4.7.2 Chromatographic Performance

A crucial parameter in assessing the performance of an analytical GC system is the peak shape. This essentially contributes to the efficiency of the chromatography and should not be affected by the coupled ion source. Ideally, the peak shape can be described using the Gaussian function. Symmetrical peaks ensure high chromatographic time resolution. Reduced peak overlap minimizes the complexity of raw data and simplifies subsequent data analysis through post-processing, e.g. deconvolution.

α-Pinene is exemplarily used to evaluate the general peak shape obtained with the ion source Design 3. Previous measurements with constant analyte introduction, the optimum gas flows for maximal sensitivity were found with 50 sccm hydrogen and 6 sccm nitrogen as reagent gas. The GC carrier gas helium was held at 2 sccm, which is a common GC effluent flow rate. The measurements were carried out with the ion source setup described in chapter 3.9.3. The settings of the gas chromatograph are listed in Table 19 #1(appendix).

Figure 56 depicts a normalized extracted ion chromatogram of 100 pg α-pinene on column (*m/z* 137; $[M+H]^+$). In practice, a significant deviation of the peak shape from the optimal 'Gauss peak' is found. The dot-dashed line indicates a Gaussian function ($\sigma = 0.2$) and clearly illustrates the deviation of the experimentally obtained peak form.

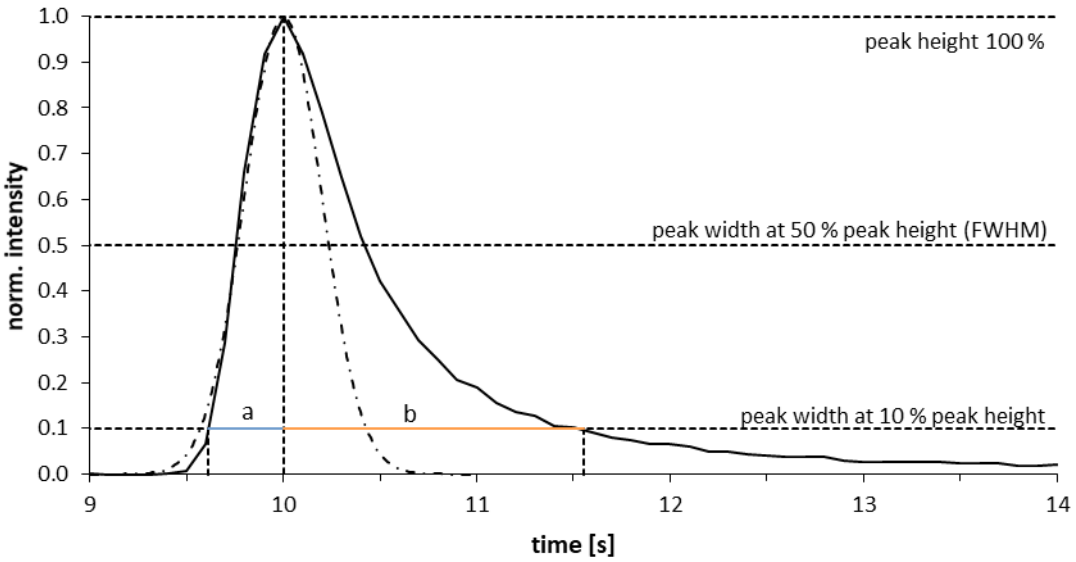

Figure 56: *Black line:* Normalized extracted ion chromatogram of α-pinene (mass trace 137, $[M+H]^+$-ion). *Black dot-dashed line:* Gaussian function (σ = 0.2).

To describe the peak shape, certain parameters can be calculated. The peak height is the intensity of the peak, from the peak top to the intersection with the baseline (measured perpendicular to the time axis). The base peak width is measured between the intersection points of the ascending and descending turning tangents with the baseline. For ideal chromatographic peaks (Gaussian peaks), the base peak width is at 13.4 % of the peak height and is four times the standard deviation of the normal distribution. Since in practice it is not always easy to determine the base peak width, often the peak width at half height is calculated instead (full width at half maximum, FWHM) [116].

The obtained α-pinene peak in Figure 56 is broadened to the right as compared to the left side. This asymmetrical tailing can be evaluated by the tailing factor (T), which is a direct measure for the shape match with the Gaussian curve. Several different equations are in use. In europe, the tailing factor is usually defined as [116]:

$$T = \frac{b}{a} \tag{11}$$

With (a) and (b) as the distance to the peak maximum at 10 % height, measured from the peak front and the peak tail, respectively. A unity tailing factor describes a symmetric peak, $T < 1$ indicates peak fronting and $T > 1$ indicates peak tailing.

Most GC column manufacturers consider tailing factors of 0.9 – 1.2 acceptable for test compounds. Many used methods generate peaks with *T*-values of 1.5. When peak symmetry has degraded to a tailing factor of 2.0 the efficiency of the separation is significantly compromised. The calculated tailing factor of the depicted α-pinene peak is 4.0, which clearly indicates peak tailing and is out of the acceptable range.

Asymmetries can have various reasons, ranging from instrumental problems to sampling deficiencies. However, instrumental problems from GC side, like dead volumes caused by a poorly installed column, liner or union, poorly cut column end, an insufficient split ratio and an overload of the column could be excluded in this case.

Different measurements with the coupled GC instrument and a variation in the ion source pressure leads to an optimized pressure of around 6 mbar with regard to best S/N ratios. Although the S/N ratio improves with higher pressure, the peak shape significantly suffers as shown in Figure 57. In this measurement, the increase in pressure was realized by reducing the amount of the differentially pumped gas, while the total ion source gas flow was kept constant. At the maximum pressure of 5.54 mbar the region of the SSQ was not further differentially pumped. Under these conditions, the entire gas flow that reaches the SSQ chamber has to pass the skimmer to be transported into the next stage. This means, that the

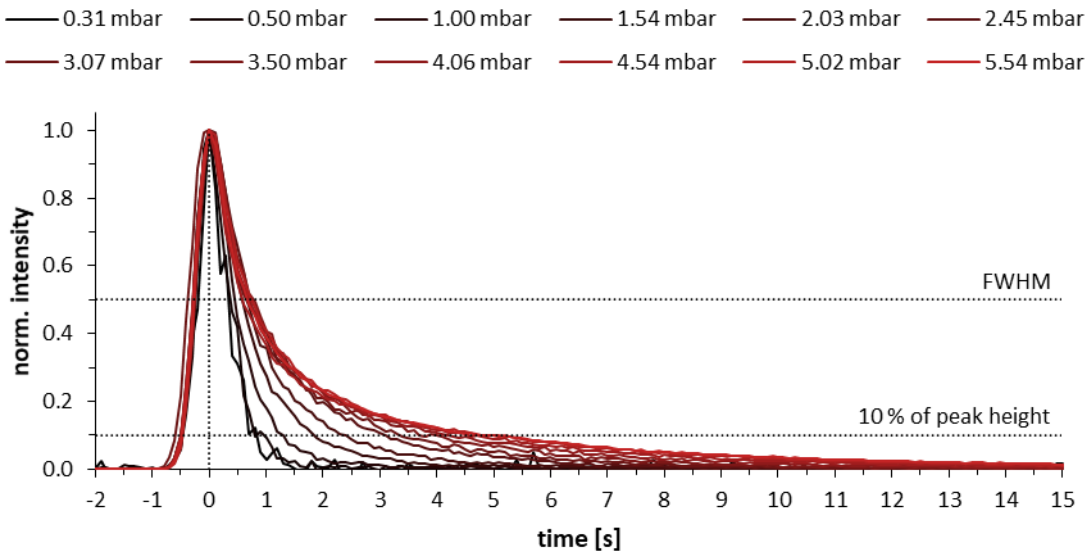

Figure 57: Normalized extracted ion chromatogram of α-pinene (mass trace 137, $[M+H]^+$-ion) for different ion source pressures.

neutral background gas, containing neutral analyte, is distributed throughout the entire SSQ chamber, before entering the next differentially pumped stage. On their way into the next stage, the neutral analyte has to pass the skimmer and crosses the focused ion beam where the large excess of protonated reagent gas can protonate the remaining neutral analyte. This causes a higher dwell time within this chamber compared to the direct ionized species, which are focused and transported due to electrical potential gradients and directly guided into the next stage.

In Figure 58 the calculated tailing factor at 10 % and 50 % height are plotted in dependence of the pressure. Interestingly, the *T*-values at 10 % height linearly correlate with the pressure, whereas at 50 % height the values are almost unaffected.

As mentioned before, at around 6 mbar source pressure the S/N ratio was at its optimum. However, to avoid this analyte accumulating effect in the SSQ chamber with the associated tailing and still obtain reasonable S/N ratios, the total ion source gas flow was increased at constant pressure. Care was taken to ensure that the mixing ratio of the plasma gas hydrogen and the reagent gas remained the same. A different gas composition would have altered the total viscosity and thus the gas flow rate through the skimmer. This could lead to a decreasing pumping efficiency and an excessive pressure increase in the next differentially pumped stage.

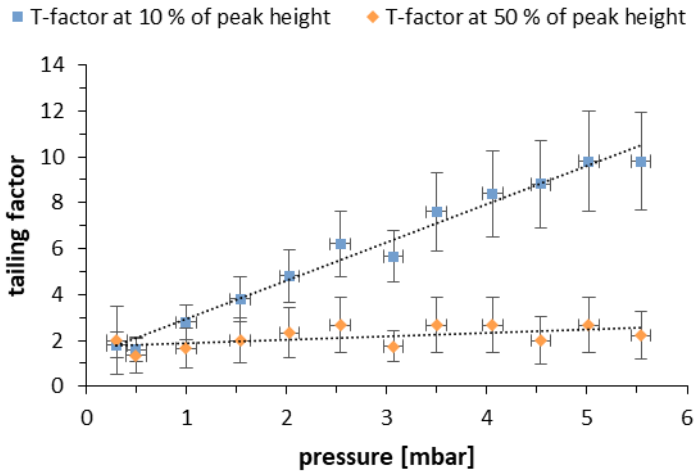

Figure 58: Calculated tailing factors at 10 % and 50 % peak height for α-pinene peaks at different ion source pressures.

Figure 59 shows the normalized extracted ion chromatograms of α-pinene (*m/z* 137; $[M+H]^+$) for four different total ion source gas flows at a constant pressure of 6.4 mbar. The positive trend on the peak symmetry with increasing gas flow is clearly seen.

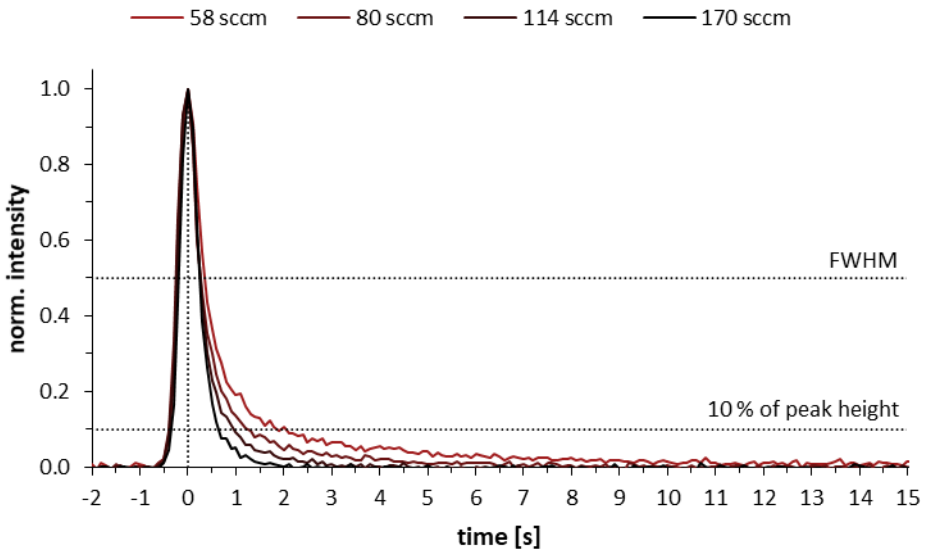

Figure 59: Normalized extracted ion chromatogram of α-pinene (mass trace 137, $[M+H]^+$-ion) for different total ion source gas flows at a constant pressure of 6.4 mbar ion source pressure.

To characterize these changes in the peak symmetry, the tailing factor at 10 % peak height is calculated and listed in Table 11. By nearly tripling the total gas flow, the tailing factor was reduced from 4.0 to 1.75, without altering the S/N ratio. Note that the FWHM is nearly unaffected. This leads to the conclusion that broadening by diffusion is negligible. In the case

Table 11: α-Pinene peak symmetry parameters for different total ion source gas flows at constant ion source pressure of 6 mbar.

Total ion source gas flow* **[sccm]**	**Tailing factor (at 10 % peak height)**	**FWHM [s]** (± 0.2)	**S/N**
58	4.0 ± 0.5	0.7	250
80	3.5 ± 0.6	0.6	290
114	2.5 ± 0.4	0.6	290
170	1.8 ± 0.4	0.6	250

* The GC carrier gas flow was kept constant, the plasma and reagent gas flow were varied, but at the same mixing ratio.

of peak broadening by diffusion within the ion source, a broadening of the peak for the entire height is to be expected. These results lead to the assumption that the peak tailing is mainly caused by the distribution of the neutral analyte in the whole SSQ chamber volume.
Therefore, the focus on the ion source Design 4 was to reduce the "dead volume" represented by the SSQ chamber to prevent a broad distribution of the neutral analyte in this part of the mass spectrometer. This should affect the peak shape and improve the chromatographic resolution. Consequently, the key difference between ion source Design 3 and Design 4 is the embedded SSQ. The entire gas - plasma, reagent and analyte – is guided directly in front of the skimmer, where the ions are extracted and the neutral gas is pumped away by the differential pumping stage (cf. chapter 3.9.4). This modification significantly improved the peak shape.
Figure 60 shows the normalized extracted peak chromatogram of α-pinene (mass trace 137, $[M+H]^+$-ion) obtained with this ion source version 4. The source parameter were previously optimized to obtain the best S/N ratio, leading to a pressure of 13 mbar. The peak parameters FWHM and the tailing factor at 10 % peak were determined to be 0.9 ± 0.2 s and 1.3, respectively.

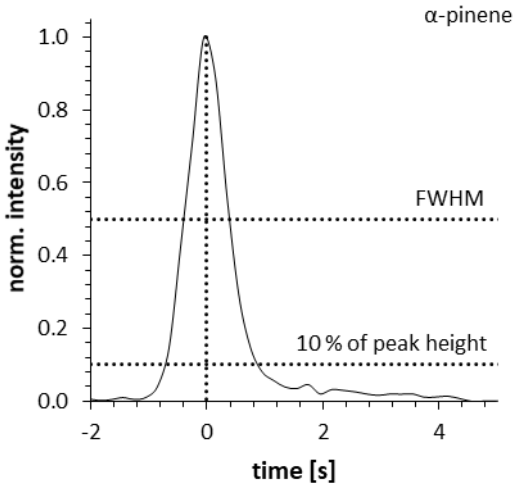

Figure 60: Normalized extracted ion chromatogram of α-pinene (mass trace 137, $[M+H]^+$-ion) obtained with the chemical ionization source Design 4. 100 sccm H_2 plasma gas flow, 200 sccm N_2 as reagent gas, 1 sccm He as GC carrier gas at 13 mbar. Ion source temperature 250 °C. GC settings cf. Table 19 #1 (appendix).

For benchmarking the chromatographic performance of Design 4 even for higher boiling point compounds, a standard FAME (fatty acid methyl ester) mixture was measured. The mixture contains C4 – C24 even carbon saturated FAMEs with boiling points up to 443 °C (cf. Table 17,

appendix). The extracted ion chromatograms of the protonated molecular ions for each compound are depicted in Figure 61.

The chromatograms show sharp peaks of nearly Gaussian shape without pronounced tailing effects even for the higher boiling point compounds. Close-ups for the two highest boiling point compounds methyl octadecanoate (443 °C) and the last eluting compound methyl lignocerate (419.5 °C) are shown in Figure 62. It is seen that the peak of methyl octadecanoate with a FWHM of 0.9 s and a tailing factor of 1.1 ± 0.1 at 10 % peak height is of almost perfect shape. The methyl lignocerate peak showed the same FWHM but a higher tailing factor with 1.7, indicating a lightly peak tailing. With a value < 2 this is still in an acceptable range for sufficient chromatographic resolution.

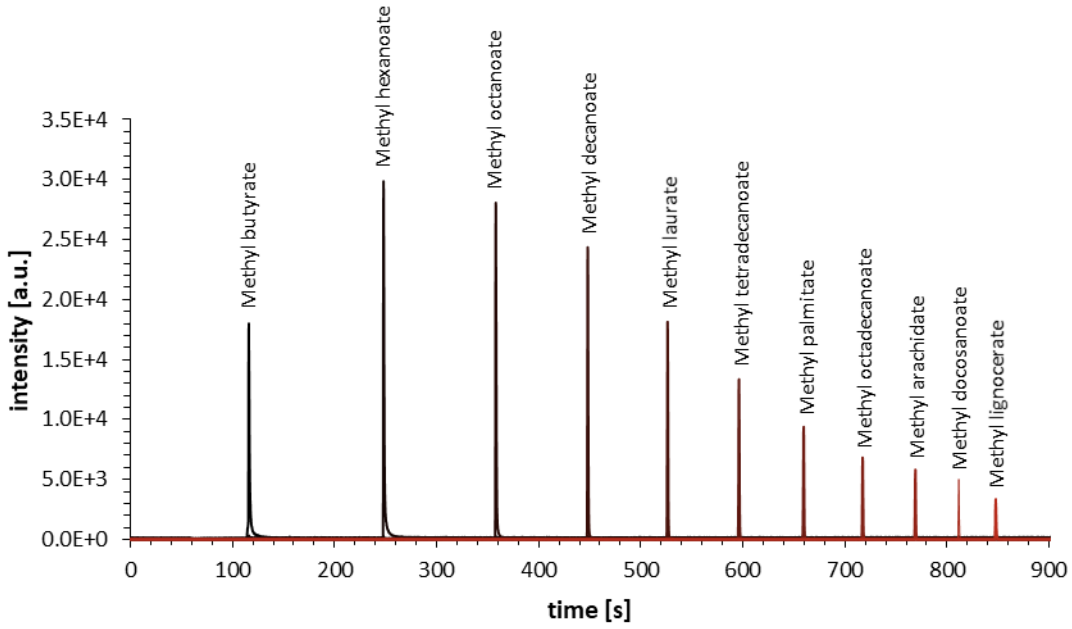

Figure 61: Extracted ion chromatogram of 1 ng C4 – C24 even carbon saturated FAMEs mixture (cf. Table 17, appendix) obtained with the chemical ionization source Design 4. 100 sccm H_2 plasma gas flow, 200 sccm N_2 as reagent gas, 1 sccm He as GC carrier gas at 13 mbar. Ion source temperature was set to 250 °C.

This benchmark measurement clearly illustrates that the previously marked peak tailing vanished with this new ion source geometry Design 4. Considering all compounds from the FAMEs mixture the FWHMs were in a range of 0.8 – 1 s and the tailing factors in a range of 1.1 – 1.7. This demonstrates that the ion source preserves chromatographic fidelity and enables further applications in the field of GC-MS.

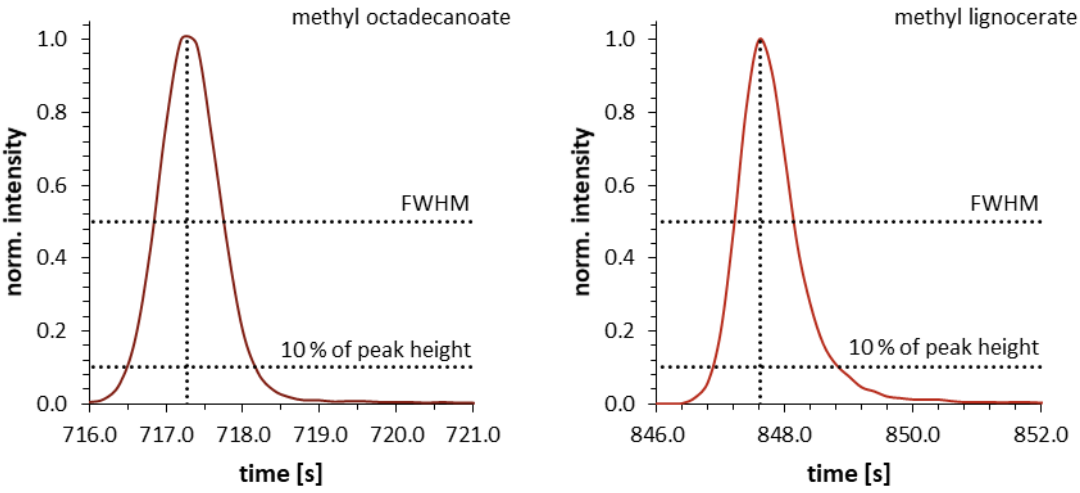

Figure 62: *Left*: Zoom-in extracted ion chromatogram of methyl octadecanoate. *Right*: Zoomed-in extracted ion chromatogram of methyl lignocerate.

4.7.3 Limit of Detection/ Dynamic Range

The ion source Design 3 was the first iteration, which enabled the hyphenation of a GC system. Since this setup still suffered from pronounced peak tailing effects, leading to poor chromatographic resolution, quantitative analytical parameters such as the limit of detection (LOD) and the linear range were determined only exemplary by measurements of *o*-xylene with nitrogen as reagent gas. A more detailed qualitative characterization of this ion source version in terms of fragmentation, adduct formation and selectivity by different reagent gases can be found in chapter 4.6.2.

Figure 63 shows the *o*-xylene calibration curve for a concentration range of 57.3 to 286.7 µg L^{-1} and an injection volume of 1 µL with a GC injector split of 100. By the calibration curve method according to DIN 32645 [117] a limit of detection of 209 fg on column is calculated. The linear range could be determined to 3 orders of magnitude.

As shown in the previous chapter, the pronounced peak tailing effects were completely eliminated in the ion source Design 4. Even high boiling point compounds showed sharp peaks of nearly Gaussian shape. With this setup, the LOD values for *o*-xylene were not re-determined by the calibration curve method. Due to the ion source's excellent chromatographic performance, which offers new capabilities, other aspects were of primary interest. However, S/N = 3 estimates for *o*-xylene and other substances showed similar LODs as with the previous ion source and the performance can be considered as equivalent to Design 3.

Instead, the limit of detection for benzophenone as an exemplary high-boiling point compound and for α-pinene as fragile analyte was determined with this setup. Both measurements were

carried out again using nitrogen as reagent gas. The obtained linear regressions of each measurement series are depicted in Figure 64. Using the calibration curve method according to DIN 32645 a limit of detection of 2.6 pg and 9.1 pg on column are calculated for benzophenone and α-pinene, respectively.

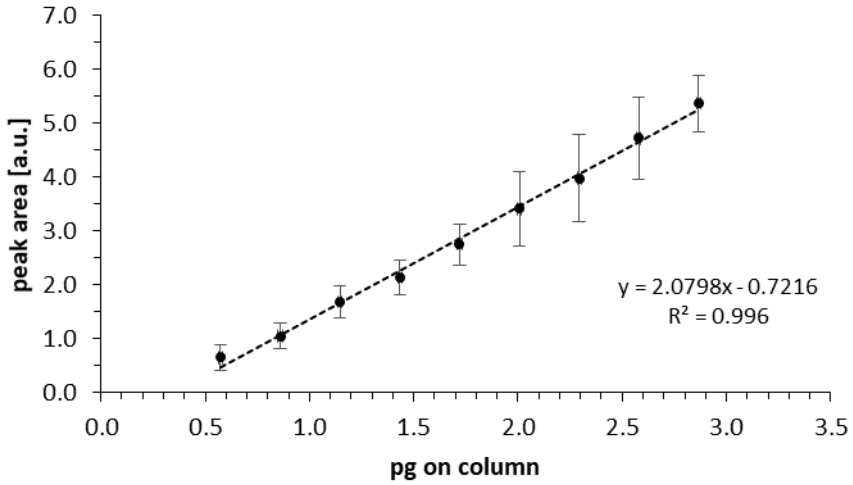

Figure 63: Determination of the limit of detection for Design 3 with *o*-xylene according to the calibration curve method DIN 32645.

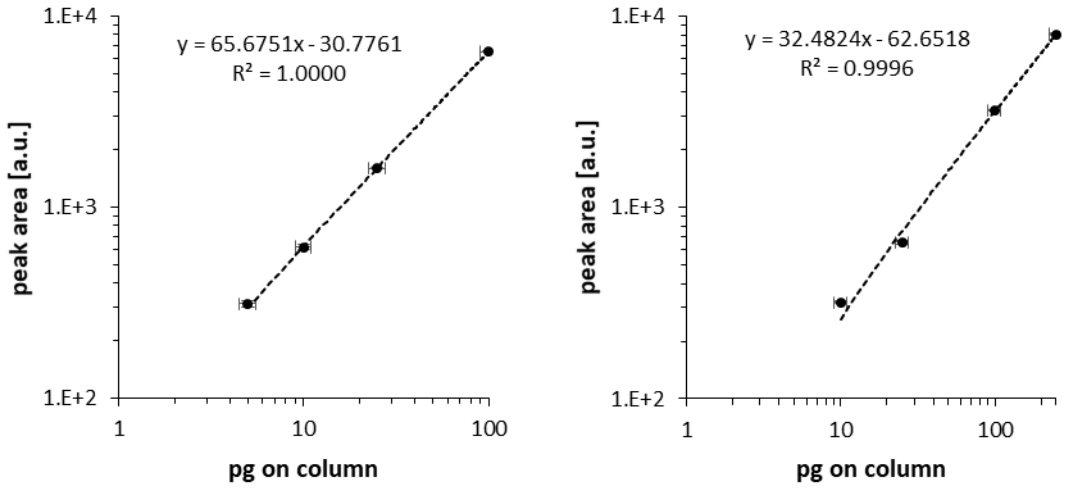

Figure 64: Determination of the limit of detection for Design 4 with benzophenone (*left*) and α-pinene (*right*) according to the calibration curve method DIN 32645.

4.7.4 Long-term Stability

The ion source Design 3 was also characterized in terms of its long-term stability. The plasma was operated 24/7 for several months without any significant performance losses. Figure 65 depicts the long-term stability over a period of 45 h.

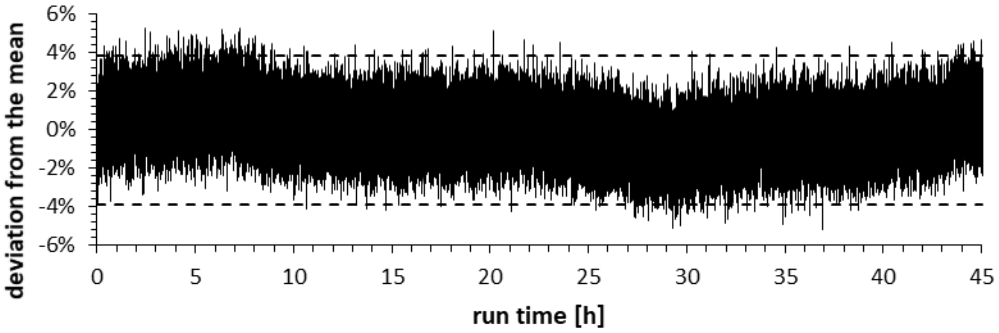

Figure 65: Total ion current long-term signal stability. *Dotted lines:* mean value +/- three times the standard deviation as upper/lower limit.

The total ion current standard deviation from the mean value is less than ± 4 %, whereby a conservative deviation of three times the standard deviation is considered in this analysis (dotted lines). The slight variance in the mean value is linked to room temperature fluctuations. Note that this measurement was done without any active heating of the ion source. For safety reasons the prototype source Design 3 was not heated unattended, since the heating wire and the thermocouple were not firmly installed at the ion source enclosure at this stage of development. During source operation in shorter daytime heating cycles, no significant fluctuations in the TIC by variations in the room temperature were observed.
A comparison for several GC runs for different analytes on various day-to-day injections shows an inter-run reproducibility of < 5 % derived by the relative standard deviation. This is within the error limits for manual GC sample injection and indicates a good reproducibility making the source suitable for analytical purposes.

To summarize, it was shown that the final version of the developed chemical ionization source fulfills all requirements for an analytical GC-MS application. The final setup demonstrated outstanding long-term stability with constant reagent gas ion current and high temperature stability (300 °C) along with maintenance of the chromatographic fidelity. Even high boiling compounds in a FAMEs mixture show chromatographic peaks of Gaussian shape with FWHMs of 0.8 – 1 s and tailing factors of 1.1 – 1.7. Preliminary results on the analytical performance

show four orders of magnitude linear range and low pg to upper fg on column LODs with inter-run reproducibilities of < 5 %.
A more detailed characterization in the context of analytical performance and application was not part of this work, but is in progress and will be published. In this publication, the selectivity and ionization efficiency of different reagent gases will be pictured using an EPA standard mixture containing 78 major environmental pollutants. The analyzed compounds included, e.g., polycyclic aromatic hydrocarbons (PAHs), nitro compounds, halogenated compounds, aromatic compounds with phenolic, acidic, alcohol, and amino groups, phthalate and adipatic esters, and aliphatic ethers.

4.8 Computational Investigations

It should be noted that the main focus of this work was not the development of quantitative computational models. The used computational programs should provide qualitative insights and support the ongoing development process of the chemical ionization source. They are intended to be used as starting points for further detailed investigations and further measurements to validate the obtained modelling results.
On the one hand, an understanding of the fluid dynamics of the system should be gained. This should enable to draw conclusions about important parameters such as the mixing of the primary plasma gas with the added reagent and analyte gas and the dwell times.
On the other hand, particle tracing simulations considering the electric fields should give an insight to the ion transfer efficiency of the used ion transfer optic elements and crucial parameters such as gained ion energy regarding analyte fragmentation.
All the parameters obtained by the simulations and modulations intend to serve as input parameters for a detailed kinetic analysis of the system, taking into account the fluid dynamic mixing of the neutral gases, as well as the ion temperature caused by the transfer optics, to further improve the ion source setup.

4.8.1 Fluid Dynamic

A three-dimensional stationary computational fluid dynamics (CFD) model was made for the ion source Design 3. To reduce the computing effort, simplified CAD versions were implemented in the CFD module from Autodesk. All surface details were neglected and approximated to simpler geometries (e.g., round quadrupole rods instead of separated, individual quadrupole segments). Otherwise, these details would drastically raise the complexity and costs of the modeling process. Preliminary modeling runs of small, more

detailed sections of the overall setup revealed, that under the considered conditions, only very subtle differences at the mean gas velocities occurred.
Once initialized, the results of the modeling can be used to determine a number of important parameters for further investigations. On the one hand, the dwell time of the neutral reagent gas and the analyte should be determined as a starting point for kinetic modelling of the reaction system. On the other hand, the spatially resolved three-dimensional calculated flow field and pressure array will be used for charged particle trajectory calculations. Further, the presumed back diffusion of the reagent gas into the plasma region will be investigated.
To get reliable results, the setup must be carefully classified in the right initial boundary conditions. Autodesk Simulation CFD provides a numerical solution to the Navier-Stokes equations. These equations assume that the fluid can be treated as a continuum. For certain flow conditions at reduced pressure, the continuum assumption may no longer hold true and individual fluid molecules must be considered. This is the case when the characteristic dimension of the flow path becomes less than 10 times the mean free path of the fluid.

To characterize the mean free path, χ, a non-dimensional value can be defined as [60]:

$$\chi = \frac{2\mu}{pL}\sqrt{RT} \tag{12}$$

With:

χ = non-dimensional vacuum number
μ = dynamic viscosity at STP
p = static pressure
L = characteristic length (diameter)
R = gas constant
T = temperature

The following ranges of χ define the validity of the Navier-Stokes equations [60]:

$\chi < 0.014$	The flow is a continuum and governed by the Navier-Stokes equations
$0.014 < \chi < 1.0$	The flow slips along surfaces (slip-flow), but can still be approximated by the Navier-Stokes equations.
$\chi > 1.0$	The flow is no longer a continuum and cannot be represented by the Navier-Stokes equations.

Furthermore, the flow characteristics are distinguished between "compressible" and "incompressible". When a fluid is compressible, its density varies with pressure. Compressible flows are usually high-speed flows with Mach numbers greater than 0.3. Within a continuous flow, further differentiation is made between laminar and turbulent flow. A laminar flow is characterized by smooth and steady fluid motion, with a hyperbolic velocity profile along the conducting cross section. A turbulent flow is a fluctuating and agitated motion. The main parameter that determines whether a flow is laminar or turbulent is the speed of the fluid. Laminar flows are typically much slower than turbulent flows. The dimensionless *Reynolds number* is used to classify a flow as either laminar or turbulent and is defined as [60]:

$$Re = \frac{\rho V L}{\mu} \tag{13}$$

where ρ is the density, V is the velocity, L the characteristic length of the geometry and μ is the dynamic viscosity. For Reynolds numbers greater than ~2500, the flow exhibits turbulent flow phenomena.

The CFD simulations shown in this chapter used compressible continuum flow conditions with χ = 2.4 10^{-3} for the skimmer and χ = 1.6 10^{-4} for the reaction tube, respectively. The walls were considered with friction leading to negligible local gas velocities ("no slip") conditions. The Reynolds number for the given geometry under investigation (880) is well below 2500 and therefore a laminar flow was assumed.
The pressure inside the SSQ chamber was initially set to 6 mbar. All these boundary conditions are based on parameters previously optimized by measurements with the ion source setup.
The simulation domain was meshed with an irregular tetrahedral mesh with slightly increased mesh resolution at crucial areas, e.g. at the outlet through the skimmer.
The results obtained with the given boundary conditions are discussed in the following section.

As mentioned before, the reaction time between the analyte and the reagent gas under the given conditions is a crucial parameter. Therefore, the gas flow characteristic in the reaction tube region, where the reagent gas and the analyte are mixed with the hydrogen plasma flow, was examined in detail.
Figure 66 depicts the axial gas velocity in the reaction tube in dependence of the radial distance. As expected from the Reynolds number, a parabolic velocity (laminar flow) profile is fully developed along the entire reaction tube length [118]. The simulated velocities are in a good agreement with the simple calculated values based on the total gas flow and the pressure.

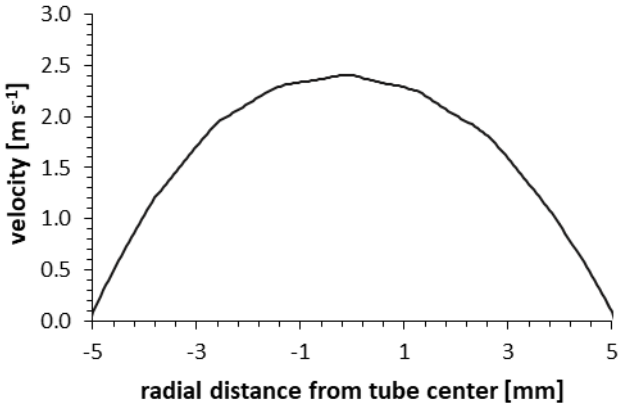

Figure 66: Simulated velocity profile of the background gas mixture within the reaction tube.

Ignoring diffusion, neutral analyte molecules are supposed to move along the axis of the reaction tube at the velocity of the background gas. With this assumption and the obtained velocity profile, the dwell time was calculated based on the distance between the point of reagent gas and analyte introduction, and the transition to the short segmented quadrupole. Since the ion acceptance into the SSQ depends on the radial ion position (cf. Figure 71), only the velocity profile values of $-2.2 < r < 2.2$ were used to calculate the dwell time. A dwell time of approximately 28 ± 4 ms is estimated.

Concerning the spatially resolved three-dimensional gas flow field, two regions are of particular interest. First of all, the transition from the reaction tube into the short segmented quadrupole, where the gas flow expands from the 10 mm inner diameter reaction tube into the 6 mbar background pressure of the large volume SSQ chamber. At this critical point, the ions also need additional guidance into the quadrupole with an inner diameter of only 4 mm.
Figure 67 shows the simulation results. As expected, the gas flow is significantly perturbed by the entrance lens of the SSQ. The electrode peels off the outer layer of the gas stream and the constriction between the entrance lens and the reaction tube causes the gas velocity to increase. The same phenomenon appears inside the SSQ. After a few millimeters passed the entrance lens, a slight gas velocity increase is noted. The gas velocity then decreases, as the flow is distributed in the large volume of the SSQ chamber.
The second part of special interest, is the region directly in front of the skimmer. Due to the small inner diameter of the skimmer (0.7 mm) and the pressure drop of about three orders of magnitude, a supersonic expansion into the next differentially pumped stage is expected. Since a supersonic expansion under the given pressure range is not trivial to calculate with

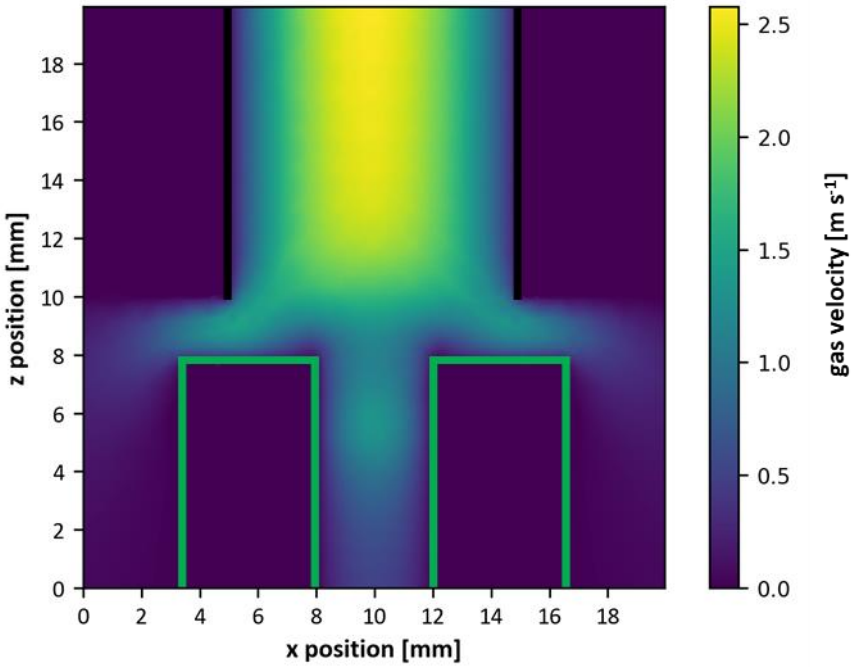

Figure 67: Cross section of the CFD simulation of the gas flow entering the SSQ chamber. *green*: Contour of the short segmented quadrupole electrode geometry including the entrance lens. *black*: Contour of the reaction tube.

numerical solutions of the Navier-Stokes equations, the gas expansion into the next differentially pumped stage was not considered in the CFD simulation. In supersonic flows, pressure effects are only transported downstream. The upstream flow is not affected by conditions and obstructions further downstream. To double check this assumption and the validity of the CFD simulations, the skimmer region and in particular the expanding supersonic jet downstream of the skimmer were also calculated in Stochastic PArallel Rarefied-gas Time-accurate Analyzer (SPARTA [119, 120]), a Direct Simulation Monte Carlo (DSMC) code. The results confirmed the CFD upstream gas velocities, indicating that the data received with the less costly CFD program are sufficiently reliable.

Figure 68 depicts the CFD simulation results of this second region. Most prominent is the strong increase of the gas velocity in front of the skimmer with up to 320 m s^{-1}. This zone forms a suction nozzle, which spreads and propagates between the skimmer lens and the last SSQ segments.

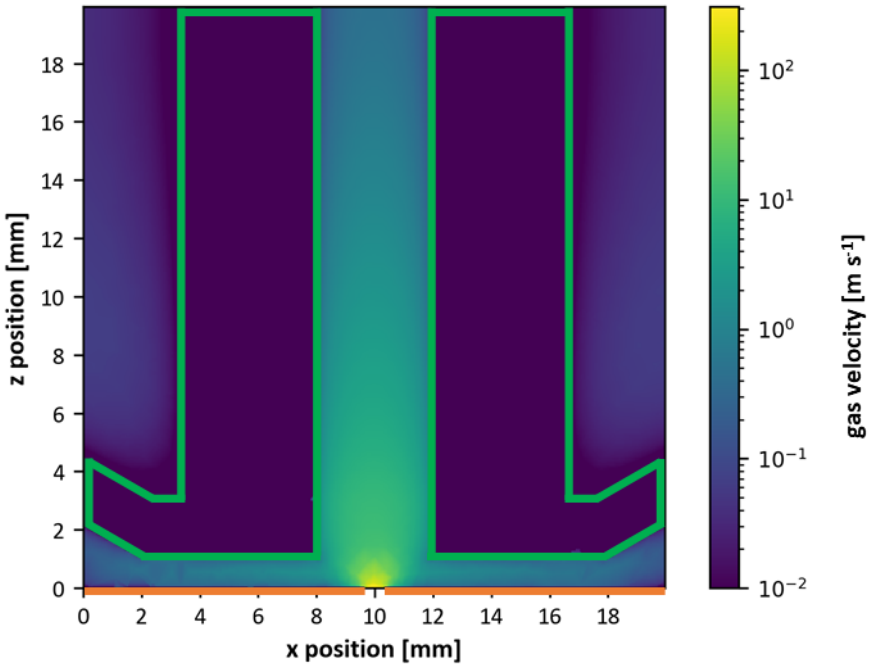

Figure 68: Cross section of the CFD simulation of the gas flow in front of the skimmer. *Green*: Contour of the short segmented quadrupole electrode geometry including the skimmer lens. *Orange*: Contour of the skimmer. The gas flow exits through the orifice, located at x = 10 and y = 0.

The CFD simulations provided further crucial insight with regard to the extent of diffusing reagent gas back into the plasma region. A quantitative estimate of this effect allows to evaluate the direct impact of the plasma zone on the reagent ion chemistry. Figure 69 shows the mole fraction of nitrogen along the center axis of the reaction and plasma tube. The nitrogen reagent gas is added at 0 mm with 6 sccm, the center of the hydrogen RF Plasma is located at -125 mm and the end of the reaction tube is at 46 mm with the total gas flow of 56 sccm in +x direction. Downstream of the reagent gas introduction, the results suggest homogenous mixing of the nitrogen with the hydrogen plasma gas after just 5 mm. Upstream, an exponential decrease in the mole fraction of nitrogen is observed. Considering the length of the helical resonator and the expansion of the plasma flare, an amount in the lower ppmV range of the reagent gas can be assumed to prevail in the plasma region. This is in the order of magnitude of the residual impurity of the used hydrogen gas (purity 5.0, < 5 ppmV N_2). Under the given conditions, no significant formation of NH_x^+ species could be detected in the mass spectra, nor resulting NH_x-adduct ions were identified in the mass spectra.

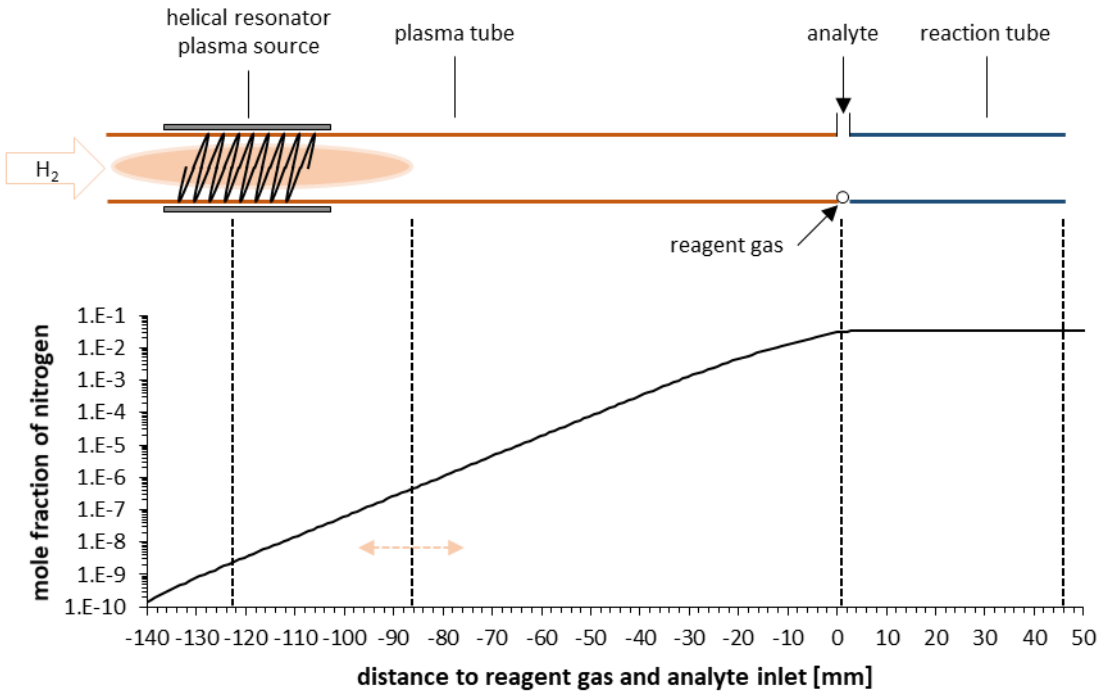

Figure 69: Mole fraction of nitrogen in relation to the distance of its addition at x = 0. The total gas flow is in +x direction.

4.8.2 Charged Particle

For charged particle tracing calculations of Design 3 (cf. Figure 9) the SIMION [55] program package was used. Due to the elevated pressure of around 6 mbar the charged particles experience strong interactions with the background gas (collisions). The random nature of the collision events leads to a partially randomization of the particle paths, which ultimately results in molecular diffusion. Subtle differences in the collision statistics in different spatial directions, generated by a directed flow of the background gas, lead to convectional transport of the ions. As a consequence, the detailed statistics of the collisions with the neutral particles governs the exact interaction with the background gas. Thus, the viscous drag and the molecular diffusion ultimately depend on ensemble parameters of the background gas (local temperature, pressure and flow velocity) as well as on molecular parameters of ion and background gas particles (size, mass). Therefore, the Collision Model HS1 user program was used, which implements a hard-sphere collision model to simulate these medium pressure conditions. The background gas flow input data (flow vectors, pressure scalar field) were taken from the Autodesk CFD model described in the previous section. Since SIMION uses the finite difference approach for the calculation of the electric fields, the calculation mesh is always regular, rectangle and equally spaced in all spatial directions (“potential array”). Consequently,

it is not readily possible to handle models with variable mesh resolution. As stated before, the fluid dynamic results in Autodesk CFD were obtained from an irregular tetrahedral mesh with the specific parameters (flow velocity vectors, pressure) at the nodes. A spatial interpolation was performed to convert the data into a potential array as an adequate input parameter file for SIMION (flow vectors, pressure scalar field).
The electric field distribution was solved for a detailed electrode geometry of the first ion optic elements (SSQ, skimmer). These elements were converted directly from the CAD file as a truly scaled SIMION potential array with a resolution of 0.05 mm per grid unit. Space charge was not considered in the simulations.
Ion trajectory simulations were carried out for masses *m/z* 3, 29 and 107 Da, corresponding to H_3^+, N_2H^+ and $[M+H]^+$ of *o*-xylene, respectively. At 6 mbar, the bulk gas pressure and thus the collision frequency is relatively high for an explicit hard sphere collision model like HS1. To handle the numerical effort on a regular personal computer, but still obtain reasonable statistical significance, simulations were performed with 10000 ions per mass. The ions started with a circular distribution of 5 mm radius at a distance of 3.85 mm from the SSQ entrance lens. The initial energy was assumed to be thermal and defined as 0.028 eV for all ions. The applied electrode potentials are listed in Table 18 #2 (appendix), which represent typical measurement settings. Ions striking the surface of the simulated geometry were treated as terminated events at that position. Typical ion trajectory simulation parameters are listed below.

Table 12: Parameters of particle tracing simulations.

Parameter	Value
Number of simulated ions per mass	10000
Bulk gas temperature	298.15 K
Bulk gas background pressure	6 mbar
Collision gas mass	4.8 Da*

* weighted average mass of a hydrogen/nitrogen-mixture (50:6)

Data were recorded after every 2 µs time step for each ion. To prevent time dependent effects of the oscillating RF voltages of the SSQ the "time of birth" of an ion was varied in a uniform distribution from 0 to 1 µs, which covers approximately 2.5 field oscillations.

A first overview of the particle tracing simulation results for each considered species is given in Figure 70. The obtained raw data were filtered and only the data of ions that passed the skimmer were considered in these plots. The 2D histograms of the ion trajectories represent

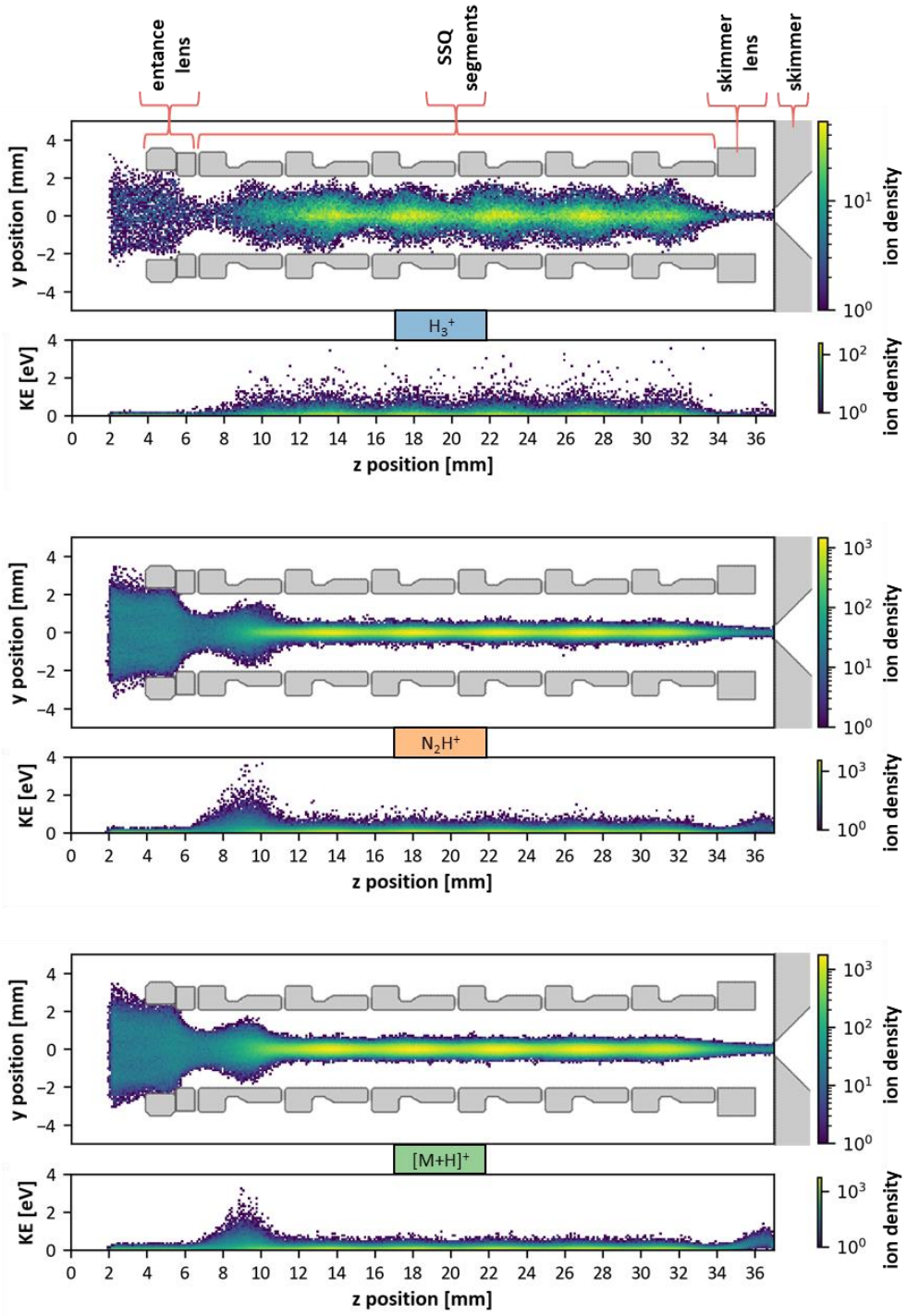

Figure 70: Visualization of SIMION simulation results. The 2D histograms represent ion densities and kinetic energies of non-terminating trajectories as a function of z-axis position. *Upper plots*: H_3^+. *Middle plots*: N_2H^+. *Lower plots*: $[M+H]^+$ of *o*-xylene. *Grey inset*: Cross-sectional view of the considered electrode geometry (SSQ, skimmer).

the ion density as a function of the y/z coordinates. A second 2D histogram shows the kinetic energy distribution for ions in a given z-axis interval.
Comparing the ion trajectories of H_3^+ with N_2H^+ and $[M+H]^+$, several qualitative differences are noticeable. Generally, H_3^+ is less focused along the SSQ, whereas the N_2H^+ and $[M+H]^+$ ions are strongly focused on the center axis by entering the 2nd quadrupole segment. These differences are also reflected by the kinetic energy distribution, which is noticeably broader for H_3^+ within the SSQ.
Considering the kinetic energy distributions for N_2H^+ and $[M+H]^+$, it is also striking that both species show a considerable broadening of their energy distribution in the first SSQ segment and an increase in the mean kinetic energy in front of the skimmer electrode. These two regions, and the region within the SSQ (3rd – 4th quadrupol segment) will be examined in more detail in the following sections. Beside the parameters of kinetic energy and radial distribution, the ion transfer efficiency of the entire ion optic geometry will be considered.

Entrance Lens

The results of the ion current measurements from chapter 4.2.2 give rise to the assumption that a considerable number of ions are lost during their transition from the reaction tube to the SSQ. This is also supported by the overview of the ion trajectory simulation results (see Figure 70).

Figure 71 shows the ion transmission efficiency through the entrance lens for each species as a function of their radial starting position. Clearly, this transmission is mass independent, as each ion shows exactly the same characteristic curve. At the given elevated pressure of 6 mbar, collisions with the background gas dominate the overall ion motion. Thus, despite a positive applied voltage to the entrance lens, the high collision rate prevents an effective ion focusing. Under the given background pressure and thermal kinetic energy, the static electric field is not mass selective.
Evidently, the initial position in the circular distribution strongly effects the probability of an ion to pass the entrance lens. Within a radius of 1.5 mm from the center axis, nearly all ions are transmitted. Between 1.5 and 3 mm the slope shows a steep decrease and levels off between 3 and 5 mm, an annulus in which virtually all ions are lost. The cumulative transmission line in Figure 71 indicates that 90 % of all transmitted ions initially started within a radial distance of about 2.2 mm from the center axis. This is only 0.2 mm wider than the entrance lens radius. This again marks the poor focusing capabilities of the entrance lens into the SSQ and the

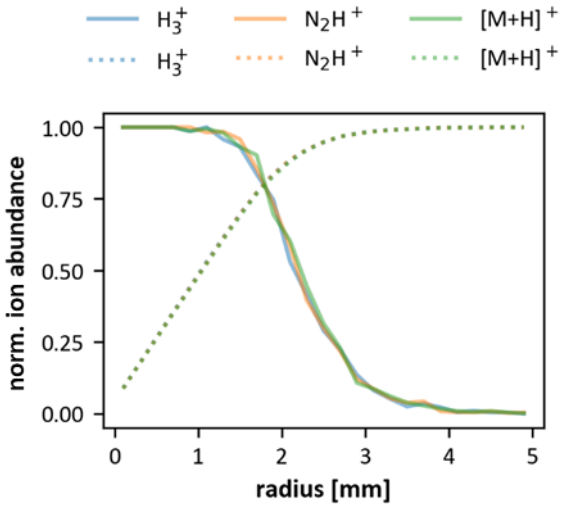

Figure 71: Ion transmission efficiency through the entrance lens as a function of the radial ion starting position for different ion masses. *Solid line:* Transmission. *Dashed line*: Cumulative transmission.

immense discrimination of ions with starting positions greater than 3 mm from the center axis away. The overall ion acceptance into the SSQ is about 22 %.

A closer look at the starting positions of transmitted ions reveals an additional dependence on their particular x/y coordinates. As seen in Figure 72, the maximum radius (distance to the quadrupole center axis) of transmitted ions into the SSQ shows a distinct dependence on their relative location to the quadrupole segments. This effect is similar for all three ion species.

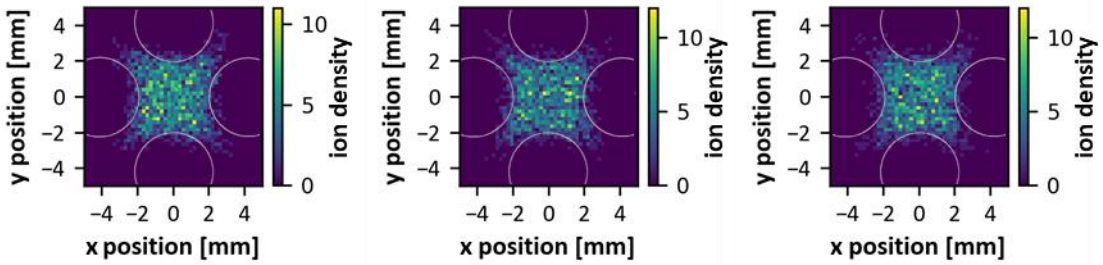

Figure 72: 2D histograms for the starting position of transmitted ions into the SSQ. *Left*: H_3^+ ions. *Middle*: N_2H^+ ions. *Right*: $[M+H]^+$ ions of *o*-xylene. *Grey*: Contour of quadrupole segments.

Since the resulting ion acceptance distribution showed essentially rotational symmetry with respect to the quadrupole geometry, the coordinates of the starting positions were transformed to the positive x/y coordinate quadrant, with the rotational axis at the origin (0/0). The center of the quadrupole segments are located at 0 ° and 90 °. In this way, a more quantitative picture of the ion acceptance angle distribution into the SSQ is obtained, as depicted in Figure 73. Clearly, the highest ion acceptance can be found exactly between two

adjacent rods at an angle of 45 °, and it decreases towards the quadrupole segments at 0 ° and 90 ° to approximately 30 – 40 %. This effect is readily explained by the quadrupolar RF field of the SSQ. In an ion optical multipole element, the time-averaged field can be described with the effective potential V^* [121]:

$$V^* = \frac{n^2}{4} \frac{q^2}{m\Omega^2} \frac{V_0^2}{r_0^2} \left(\frac{r}{r_0}\right)^{2n-2} \tag{14}$$

With the charge q, the number of electrodes n, the ion mass m, the angular frequency Ω, the amplitude V_0, the inner radius of the electrode arrangement r_0 and the radial distance of the ion r inside the multipole. In case of the SSQ, the number of electrodes is 2 and it can be seen that the effective potential varies with $\left(\frac{r}{r_0}\right)^2$. In general, V^* is high close to the rods and low near the center. This results in a local minimum of the effective field at an angle of 45 °, exactly in the middle of two adjacent quadrupole segments with alternating RF amplitudes applied. On the contrary, directly at the quadrupole segments, at 0 ° and 90 °, the effective potential has a local maximum and causes ions to be deflected. This is in good accordance with the simulation.

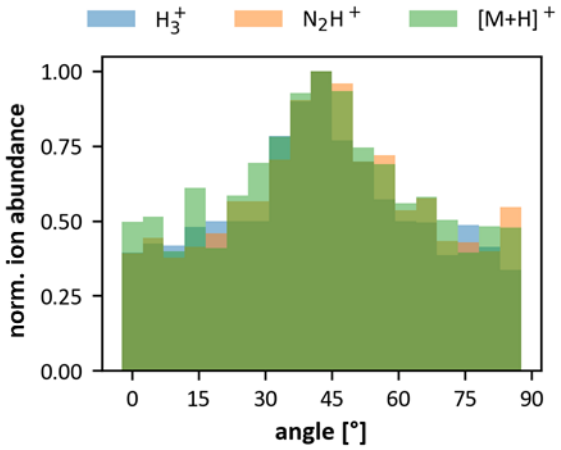

Figure 73: Ion acceptance angle distribution into the SSQ.

Kinetic energy distribution

Measurements with certain SSQ settings showed considerable declustering effects and also fragmentation of fragile analyte ions. The occurrence of such processes depends on the energy accumulated by an ion during its transmission to the mass analyzer. This energy gain is a function of the electric field and is thus defined by the applied voltages on the ion optical elements. The acceleration of an ion along the electrical force increases its kinetic energy. In

collisions with the bulk gas, some of this kinetic energy is converted into internal degrees of freedom. This energy is redistributed between the translational, rotational and vibrational modes. The stronger the electric field, the more energy is transferred and accumulated in the internal modes, eventually causing the ion to fragment.

SIMION simulations generally follow the hard-sphere collision model, which completely ignores internal degrees of freedom, and consequently cannot directly depict a fragmentation process. Nevertheless, the calculated kinetic energies can be regarded as lower fragmentation limits. Whenever the kinetic energy is near an ion dissociation limit, fragmentation becomes more likely. In the following, three sections of the transfer are exemplarily scrutinized with regard to the radial ion distribution and the kinetic energy distribution (cf. Figure 74).

The first section between 8.5 and 9.5 mm in Figure 70, shows a pronounced radial divergence of N_2H^+ and $[M+H]^+$ in the first SSQ segment, after the ions were actually slightly focused to the center axis by passing the entrance lens. The upper left plot in Figure 74 depicts the radial ion distribution in this section. Both species show a broad radial distribution, with a FWHM of about 1 mm and a base width up to 1.7 mm. Since the ion kinetic energy is a function of the effective field according to equation 14, it correlates with a quadratic dependence of the radial position. This means the larger the distance of an ion to the center axis, the higher the effective field and thus its gain in kinetic energy. The simulated ion energy distributions of this particular section are depicted in the upper right plot of Figure 74. Both energy distributions show a most frequent value slightly above thermal energy in the range of 0.02 - 0.04 eV with a decreasing high energy tail up to 1.5 eV.

After broadening of the ion cloud in the first segment, the N_2H^+ and $[M+H]^+$ ions are entirely collimated to their stable radial trajectories onto the center axis, when entering the second SSQ segment. In contrast, the H_3^+ ion cloud shows an alternating oscillation in its radial distribution along each SSQ segment. To illustrate the radial and kinetic energy distributions while crossing the SSQ, the summed distributions for the interval from the 3rd to the 4th segment (16 – 25 mm, cf. Figure 70) are shown in the two central plots from Figure 74. Clearly, N_2H^+ and $[M+H]^+$ are spatially very confined around the middle axis, with the most abundant values of 0.1 and 0.2 mm, respectively, and a base width of 0.6 mm. In contrast, the H_3^+ ions reveal a significantly broader radial distribution, with the most frequent radius at about 0.4 mm and a base width up to 2 mm. These two distinct differences are also reflected by the kinetic energy distributions. Even though the mean kinetic energy of all species ranges between 0.02 and 0.04 eV, the high energy tails of the distributions clearly differ. The H_3^+ ion kinetic energy distribution shows a base width of up to 1 eV, which is twice the base width of N_2H^+ and

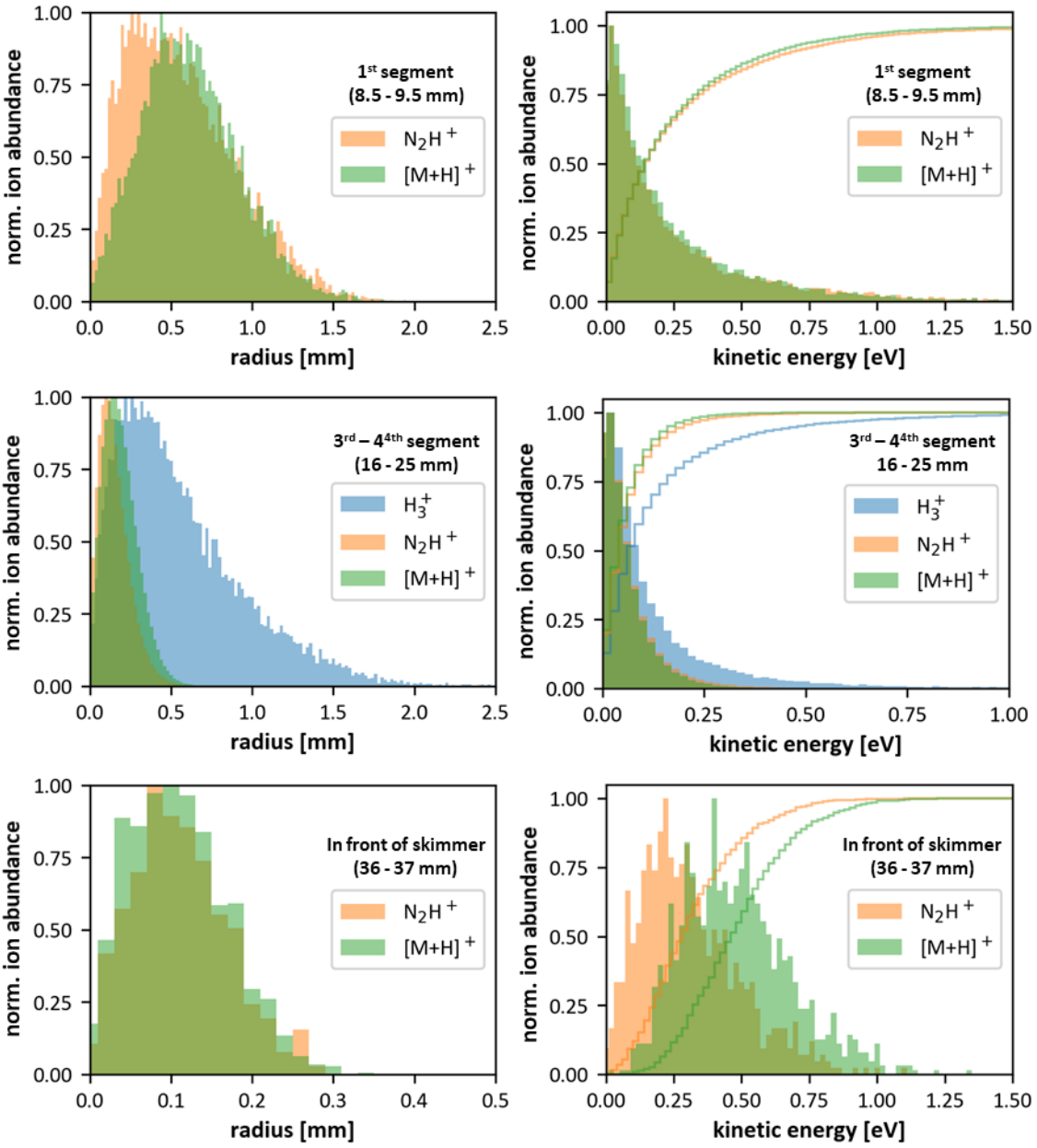

Figure 74: Histograms of the radial and kinetic energy distribution at three different sections along the z-axes of the SSQ. *Upper plots:* 1st quadrupole segment (z = 8.5 – 9.5 mm). *Middle plots:* 3rd to 4th quadrupole segment (z = 16 – 25 mm). *Lower plots:* Skimmer lens to skimmer (z = 16 – 25 mm). *Solid lines*: Cumulativ ion abundance.

$[M+H]^+$. The considerably lower focus of H_3^+ and the resulting broader kinetic energy distribution can be explained by RF heating effects, since the mean bulk gas mass is higher than the mass of the H_3^+ ion [122]. Contrary, this also explains the very good focusing capability of the SSQ for N_2H^+ and $[M+H]^+$. Since the ion mass is much higher than the mean bulk gas mass and the pressure is considerably high, this leads to pronounced collisional cooling effects and

a very small radial distribution. Also note, under the given voltage and frequency settings, the H_3^+ ion is not in the stable mass range of the quadrupole. The low mass cut-off can be calculated as *m/z* 12 [123]. However, the real cut-off may slightly differ, since this calculation does not consider any collisions, only the electric fields.

The last section of interest, with respect to ion energy considerations, is the transition from the skimmer lens to the skimmer. In Figure 70, an increase in the mean kinetic energy is observed for N_2H^+ and $[M+H]^+$. The H_3^+ ions are not considered in this section for the following reasons: (i) The low transmission efficiency does not provide enough H_3^+ ions at the end of the transfer for statistical reliability, (ii) from estimates in kinetic models, all H_3^+ ions should have reacted to other ionic species and (iii) H_3^+ ions were never observed in any mass spectra. The lower plots in Figure 74 show the radial and the kinetic ion energy distributions summed from 36 mm to 37 mm in z position (gap between skimmer lens and skimmer, cf. Figure 70). Despite the very narrow radial ion distribution (left plot), a very broad ion energy distribution (right plot) is noticeable. In this section, the ions leave the RF quadrupolar field and are further radially focused by the DC potential between the skimmer lens and skimmer. With 48.1 V, the applied DC gradient between these two electrodes is considerable high. This leads to a most frequent kinetic energy of 0.2 and 0.45 eV with base widths of 0.9 and 1.2 eV for N_2H^+ and $[M+H]^+$, respectively. Considering the cumulative distributions, it is seen that 20 % of the N_2H^+ ions get a kinetic energy > 0.4 eV and 20 % of the $[M+H]^+$ ions > 0.8 eV.
To put the obtained kinetic energies into perspective, the dissociation energy, e.g., for the second and third water clusters are 1.3 eV and 0.95 eV [124], respectively. Considering that in the simulation no energy conversion to internal modes and energy accumulation is taken into account, it may seem feasible that water clusters get fragmented due to the given skimmer lens and skimmer voltages. This has also been observed in different measurements. Comparing the two mass spectra in chapter 4.4.3, it becomes clear that the water cluster formation is strongly affected by the chosen transfer settings. With the same voltage settings used in the simulation (cf. Figure 29), only the H_3O^+ ion signal is observed. By using "soft" transfer settings (cf. Figure 30), also the second and third water cluster signals appear.
Effects of pronounced fragmentation due to the transfer settings were also observed with α-pinene. The dissociation channel leading to the $C_9H_{13}^+$ (*m/z* 121) fragment of α-pinene has a dissociation energy of only 0.76 eV [125]. By re-adjusting the SSQ transfer settings, the appearance of this fragment could be reduced.
This clearly shows, that in addition to the proper choice of the reagent gas in terms of dissociative protonation, also the transfer settings in the collision-dominated SSQ region must

be considered, when it comes to analyte fragmentation. From an analytical point of view, less fragmentation is desirable in most cases, since it leads to higher molecular ion peaks, less complex spectra and also increased sensitivity.

Transmission Efficiency

From the trajectory simulations also the probability for the successful transport through the ion optical stage for H_3^+, N_2H^+ and $[M+H]^+$ of *o*-xylene was derived. Simply, the number of ions at each characteristic spot – (i) entrance lens, (ii) skimmer lens and (iii) skimmer (cf. Figure 70) - were counted and the respective transfer efficiencies calculated. A glimpse at the data in Table 13 immediately reveals the considerable loss of ions at the entrance of the SSQ, due the poor focusing quality of the entrance lens. Each species shows a transfer efficiency through this ion optical element of approximately 22 %. Once an ion survived this first hurdle, its probability to be transmitted through the entire SSQ up to the skimmer lens is near unity, at least for the two higher masses N_2H^+ and $[M+H]^+$. As expected, H_3^+ is significantly less efficiently transmitted through the SSQ under the given transfer settings and only 8 % of its population survives. Generally, the efficient transmission of small and heavy ions in a multipole ion guide depends on the applied mass window of the multipole [126, 127]. With the settings under consideration, the mass of an H_3^+ ion is lower than the low mass cut-off of the given geometry. In addition, H_3^+ is partially lost due to RF heating effect, as discussed in the previous section.

Table 13: Calculated ion transfer efficiencies at different points in the SSQ for each simulated ion mass.

Ion transfer position	Total transfer efficiency [%]
Through entrance lens:	
H_3^+	22
N_2H^+	22
o-xylene $[M+H]^+$	23
To skimmer:	
H_3^+	4
N_2H^+	22
o-xylene $[M+H]^+$	23
Through skimmer:	
H_3^+	8
N_2H^+	10
o-xylene $[M+H]^+$	14

Another spot of tremendous ion loss is the skimmer. Approximately half of the incoming population does not find the way into the next stage of the MS.
Compared to the experimentally determined total transmission efficiencies, based on ion current measurements (cf. chapter 3.8.2), the simulations are in good agreement. Assuming that the ion current measured on the entrance lens corresponds to the sum of all ions reaching the entrance lens, independent of whether they will pass the lens or not. The ion current measured on the skimmer will only result from the ions that have previously passed the entrance lens and are transmitted through the SSQ. Thus, the transfer efficiency through the lens would be at least equal to the measured ion current on the skimmer and would be minimum 29 %. This is slightly above the simulated transmission of about 22 - 23 %. However, the simulation assumed a uniform ion distribution as the initial condition. However, in reality, the ions will may have a certain radial density distribution, since ions are lost on the reaction tube surface. This will increase the ion density on the center axis compared to the edges and the simulations indicated a significantly better transmission on the center axis.

4.8.3 Reaction Kinetics

The simulation of ion-neutral chemistry in a plasma is highly complex. It requires the knowledge of crucial plasma parameters, e.g., electron density and electron temperature, and detailed models of the gas phase chemistry (electron ionization, dissociation, and neutralization and ion-molecule reactions) and the surface chemistry (wall neutralization, heterogeneous reactions). Since these parameters are not adequately known for the given helical resonator plasma, the chemistry in the hydrogen plasma region is not considered. Instead, H_3^+ is assumed to be the main ionic species released from the plasma and serves as the starting point of all considered reaction cascades. This is in line with the results of previous experiments (cf. Figure 16 and Reference [128])
For a preliminary kinetic analysis of the chemical reaction system observed with ion source Design 3, the open-source software package Cantera (Version 2.2.1) [62] was used. It takes an initial system configuration (thermodynamic phase, chemical species and chemical reactions of these species) and simulates the time evolution of the chemical system. The chemical species and reactions defined in Table 14 served as input parameters. These reactions and rate coefficients are based on the work of D. Müller [64] and are extended to the given chemical system. Since the observed main ionic species are protonated, only proton transfer processes are considered.

Table 14: Reaction pathways and rate coefficients used for kinetic simulations. Rate coefficients are taken from [50].

Reaction	Rate coefficient
$H_3^+ + N_2 \rightarrow N_2H^+ + H_2$	$1.86 \cdot 10^{-9}$ [$cm^3\ s^{-1}$]
$H_3^+ + CO_2 \rightarrow CO_2H^+ + H_2$	$2.5 \cdot 10^{-9}$ [$cm^3\ s^{-1}$]
$H_3^+ + O_2 \rightarrow HO_2^+ + H_2$	$6.7 \cdot 10^{-10}$[$cm^3\ s^{-1}$]
$H_3^+ + H_2O \rightarrow H_3O^+ + H_2$	$5.3 \cdot 10^{-9}$ [$cm^3\ s^{-1}$]
$N_2H^+ + H_2O \rightarrow H_3O^+ N_2$	$2.6 \cdot 10^{-9}$ [$cm^3\ s^{-1}$]
$CO_2H^+ + H_2O \rightarrow H_3O^+ + CO_2$	$2.65 \cdot 10^{-9}$ [$cm^3\ s^{-1}$]
$HO_2^+ + N_2 \rightarrow N_2H^+ + O_2$	$8.0 \cdot 10^{-10}$ [$cm^3\ s^{-1}$]
$HO_2^+ + H_2 \rightarrow H_3^+ + O_2$	$3.3 \cdot 10^{-10}$ [$cm^3\ s^{-1}$]
$HO_2^+ + CO_2 \rightarrow CO_2H^+ + O_2$	$1.1 \cdot 10^{-9}$ [$cm^3\ s^{-1}$]
$H_3O^+ + H_2O + M \rightarrow [(H_2O)_2H]^+ + M$	$6.98 \cdot 10^{-29}$ [$cm^6\ s^{-1}$]
$[(H_2O)_2H]^+ + M \rightarrow H_3O^+ + H_2O + M$	$4.0 \cdot 10^{-27}$ [$cm^3\ s^{-1}$]
$[(H_2O)_2H]^+ + H_2O + M \rightarrow [(H_2O)_3H]^+ + M$	$6.98 \cdot 10^{-29}$ [$cm^6\ s^{-1}$]
$[(H_2O)_3H]^+ + M \rightarrow [(H_2O)_2H]^+ + H_2O + M$	$6.78 \cdot 10^{-19}$ [$cm^3\ s^{-1}$]
$[(H_2O)_3H]^+ + H_2O + M \rightarrow [(H_2O)_4H]^+ + M$	$6.98 \cdot 10^{-29}$ [$cm^6\ s^{-1}$]
$[(H_2O)_4H]^+ + M \rightarrow [(H_2O)_3H]^+ + H_2O + M$	$2.5 \cdot 10^{-16}$ [$cm^3\ s^{-1}$]
$H_3^+ + C_6H_6 \rightarrow C_6H_7^+ + H_2$	$3.3 \cdot 10^{-9}$ [$cm^3\ s^{-1}$]
$H_3^+ + C_6H_5CH_3 \rightarrow C_7H_9^+ + H_2$	$2.92 \cdot 10^{-9}$ [$cm^3\ s^{-1}$]
$\rightarrow C_7H_7^+ + 2\ H_2$	$0.78 \cdot 10^{-9}$ [$cm^3\ s^{-1}$]
$\rightarrow C_6H_5^+ + H_2 + CH_4$	$0.78 \cdot 10^{-9}$ [$cm^3\ s^{-1}$]
$H_3^+ + C_6H_4(CH_3)_2 \rightarrow C_8H_{11}^+ + H_2$	$4.1 \cdot 10^{-9}$ [$cm^3\ s^{-1}$]*
$N_2H^+ + C_6H_6 \rightarrow C_6H_7^+ + N_2$	$1.5 \cdot 10^{-9}$ [$cm^3\ s^{-1}$]
$N_2H^+ + C_6H_5CH_3 \rightarrow C_7H_9^+ + N_2$	$1.3 \cdot 10^{-9}$ [$cm^3\ s^{-1}$]
$N_2H^+ + C_6H_4(CH_3)_2 \rightarrow C_8H_{11}^+ + N_2$	$1.0 \cdot 10^{-9}$ [$cm^3\ s^{-1}$]*
$H_3O^+ + C_6H_6 \rightarrow C_6H_7^+ + H_2O$	$1.9 \cdot 10^{-9}$ [$cm^3\ s^{-1}$]
$H_3O^+ + C_6H_5CH_3 \rightarrow C_7H_9^+ + H_2O$	$2.2 \cdot 10^{-9}$ [$cm^3\ s^{-1}$]
$H_3O^+ + C_6H_4(CH_3)_2 \rightarrow C_8H_{11}^+ + H_2O$	$2.4 \cdot 10^{-9}$ [$cm^3\ s^{-1}$]
$C_6H_7^+ + C_6H_5CH_3 \rightarrow C_7H_9^+ + C_6H_6$	$1.0 \cdot 10^{-9}$ [$cm^3\ s^{-1}$]*
$C_6H_7^+ + C_6H_4(CH_3)_2 \rightarrow C_8H_{11}^+ + C_6H_6$	$1.0 \cdot 10^{-9}$ [$cm^3\ s^{-1}$]*
$C_7H_9^+ + C_6H_4(CH_3)_2 \rightarrow C_8H_{11}^+ + C_6H_5CH_3$	$1.0 \cdot 10^{-9}$ [$cm^3\ s^{-1}$]*

* estimated via collision limit
M = unspecified collision partner

The initial concentrations of the chemical species are defined as mole fractions. The given mole fractions are taken as relative values and are normalized by Cantera. The absolute concentrations are calculated from the thermodynamic state (temperature, pressure etc.) and the thermodynamic model of the phase in the reactor.

Figure 75 shows the result of a time dependent kinetics simulation of the reaction system defined in Table 14. The simulation was run with an isobar and adiabatic model of an ideally stirred reactor at a pressure of 5.8 mbar. The initial concentrations are determined from the following mixing ratios: 50 sccm H_2 (grade 7.0), 5 sccm N_2 (grade 5.0), 1 sccm BTX-mixture in N_2 (8.7 ppmV benzene, 6 ppmV toluene, 5.1 ppmV *o*-xylene; cf. Table 16 #3, appendix). The trace contaminants O_2, CO_2 and H_2O were assessed by the purity of the used gases and the base pressure of the ion source ($5 \cdot 10^{-4}$ mbar, 25 % humidity). The initial H_3^+ concentration was calculated via the TIC ($7.7 \cdot 10^6$ cps) of a mass spectrum multiplied with an estimated ion loss factor of 100.

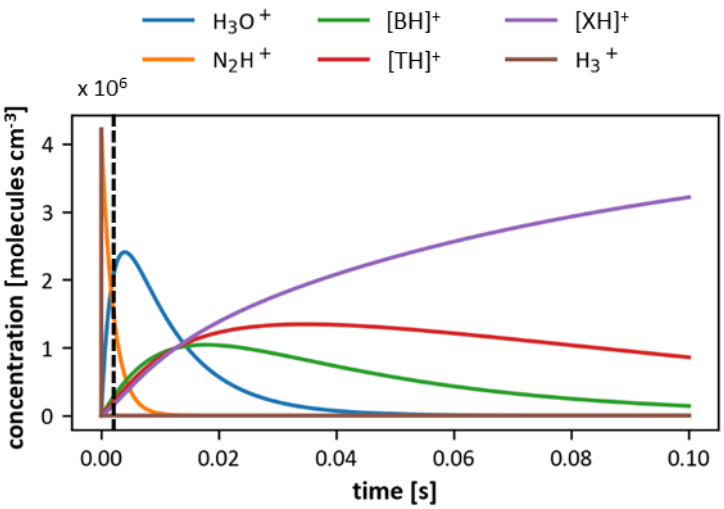

Figure 75: Time dependent concentration profile of the formed main ion species from the kinetic simulation. *Dotted line*: Time marker (1.8 ms).

The results show the expected temporal development. According to the reaction rate coefficient and the respective mole fractions of the compounds, the initial H_3^+ is almost completely converted into N_2H^+ and then reacts with the trace impurity H_2O to form H_3O^+, with simultaneous protonation of the analytes. As the reaction time progresses, the protonated analytes benzene, toluene and *o*-xylene subsequently react with each other until protonated *o*-xylene dominates.

Figure 76 compares the relative ion distribution from a measured mass spectrum with the simulation results. It is apparent that the relative ion distribution matches very well the observed mass spectrum. The matched distribution is already established after only 1.8 ms and is thus significantly shorter (~ factor 15) than the estimated dwell time of the bulk gas in the

CFD simulation (cf. chapter 4.8.1). This is most likely due to the applied model, which assumes an ideally stirred reactor and does not include any fluid dynamics i.e. laminar flow conditons. Further, the weak NH_4^+ signal (*m/z* 18) in the mass spectrum indicates that not all reaction channels were included. As described in chapter 4.5, the formation of NH_4^+ requires the dissociation of the precursor molecules N_2 and H_2. This reaction can only occur in the plasma glow.

However, a number of additional aspects were not considered ,e.g., (i) back diffusion (ii) ion loss on the reaction tube surface (iii) mass discrimination effects of the quadrupole or iv) any potential gradients due to charging effects or the plasma potential. Nevertheless, even though not all observed ionic species could be brought into agreement with the proposed chemical reaction system and the simulation is idealized, the main ion species, their distribution and the temporal development of the signals show similar trends as observed in measurements of

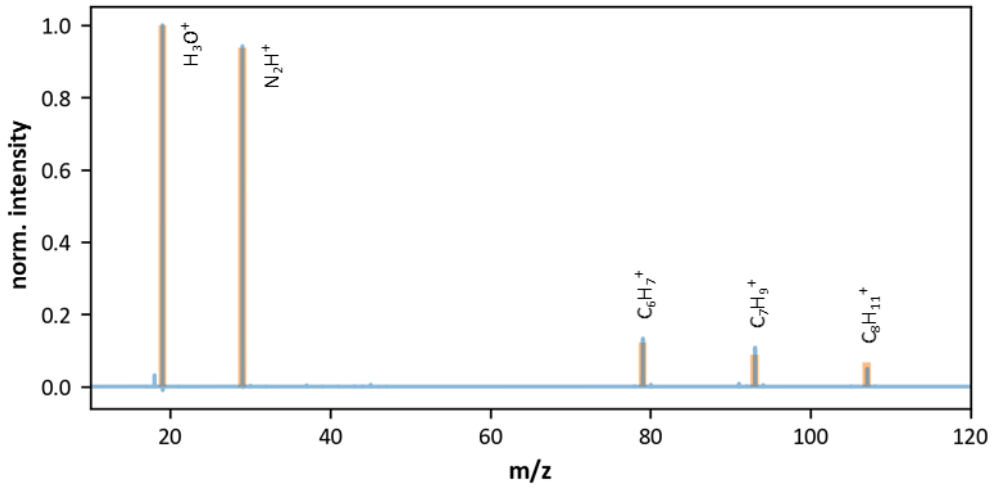

Figure 76: *Orange*: Bar plot of the ion distribution from the kinetic simulation at 1.8 ms. *Blue line*: Mass spectrum obtained with the chemical ionization source Design 3. 50 sccm H_2 plasma gas flow, 1 sccm BTX-mixture in N_2 (cf. Table 16, #3, appendix) and 5 sccm N_2 as reagent gas at 5.8 mbar. Ion transfer settings cf. Table 18 #2 (appendix).

pressure and reaction time variations. This allows the assumption that at least the main reaction pathways of the system are accurately described and implies that there is still room for improvement regarding the ionization degree of the analyte. It should be possible to further increase the degree of analyte ionization by extending the reaction time. If the mixture of analytes is fed via a gas chromatograph, each compound peak is baseline-separated in an ideal case and passes temporally resolved into the ionization source. Therefore, the interaction of analytes with each other becomes virtually irrelevant. Only self-CI and transformation processes could be eligible. Fragment ions from the analyte neutral molecule itself could

undergo ion-molecule reactions or the occurrence of hydrogen-bonded clusters of the molecular ion might become an issue. This will be the subject of further investigations in the future.

However, the results also show that the amount of water as a trace contaminant has to be considerably reduced, if N_2H^+ is intended to be used as the primary protonation reagent ion for analayte ionization.

Conclusion

Qualitatively, the simulation results agree well with measurements and observations. It seemed that a considerable number of ions is lost due to the weak focusing into the SSQ and through the skimmer. This is also reflected by the kinetic energy distributions of the ions. To provide sufficient ion focusing, large potential gradients are applied, which lead to induced fragmentation and declustering effects. This raised the question whether the ion source setup combined with the SSQ is the optimum solution. Normally, the SSQ is used in combination with an orifice based supersonic expansion, where the aperture diameter is at least two orders of magnitude smaller than the SSQ entrance lens. However, the iterative development of the ion source has resulted in the current design, with similar sizes of the reaction and plasma tube diameter. Any effort to focus the reaction tube gas flow into the SSQ by either restricting the reaction tube inner diameter with a nozzle end or the use of metal orifices, has shown significant ion losses on the surfaces. Focusing ions into the SSQ by means of electrostatic lenses is also very difficult at the given pressures, as suggested by respective simulations. The high rate of collisions inhibits effective focusing with static lens stacks. Consequently, the transmission issue from ions into the next differentially pumped stage of the mass spectrometer should be thoroughly revised in the future development. Due to the given pressure range, RF focusing is required. As shown in the simulations, the ion acceptance angle of the quadrupole is relatively small. However, once entered the SSQ, they were very efficiently focused and transmitted by the applied RF field and DC gradient. A higher order multipole, like a hexapole, would have a more appropriate acceptance angle and could be a feasible alternative. Furthermore, as seen from equation 14, the effective potential of a hexapole depends on $(r/r_0)^4$. A hexapole has a much lower impact on the radial energy due to a larger field free region, as the effective potential is flatter close to the center. This means, a broad radial entrance distribution of the ions, as expected by the diameter of the reaction tube, will cause less kinetic energy gain as compared to the quadrupole. However, a drawback of using a hexapole could be the lower focusing efficiency, which might be a problem in combination with

the skimmer orifice. The relatively small inner diameter of this orifice is substantial to maintain the pressure in the next differentially pumped stage.
Another conceivable and maybe more suitable RF focusing device for better ion transmission efficiencies could be an ion funnel system. Their working pressure regimes are in a suitable range of 0.1 to 30 mbar [129] and they have a large ion acceptance angle. They aim to efficiently capture ions with a broad distribution and radially focus them for efficient transfer through a conductance limiting orifice.

5. Summary and Outlook

5.1 Summary

Most classical chemical ionization sources utilizing electron emitting filaments suffer from reduced operation lifetime and decrease in ion intensity over time. The aim of this work was the development of a concept and prototype for an alternative chemical ionization source for GC-MS applications, providing long-term stability and low maintenance.

The developed chemical ionization method is based on a RF hydrogen plasma, driven at medium pressure and leading to H_3^+ as the primary reagent ion population. Since the proton affinity of H_2 is much lower than that of almost all atoms and molecules, H_3^+ can act as a universal proton donor via proton transfer reactions. A conventional, low cost ballast for photoionization detector lamps was successfully adopted for use as a plasma source. This helical resonator is distinguished by its compactness and robustness, allowing the operation of a RF plasma without complex matching network.

In a first step, the helical resonator was further customized and a fundamental knowledge of the parameters affecting the primary ion current were obtained. It was shown, that the primary ion current is strongly affected by the operating frequency. Since this plasma type is operated in an electrical resonant state, resembling a coaxial quarter-wave resonator, the highest ion current is obtained matching its resonance frequency. The structure becomes resonant when the coil is designed with an electrical length of one fourth of the excitation frequency. Utilizing a custom coil directly wound on the plasma tube, carefully designed to match these parameters and slight modifications on the RF power supply, the primary ion current could be increased by a factor of 6, providing sufficiently high primary ion densities. In addition, the operating pressure maximum could be increased from 4 mbar to approximately 15 mbar.

Based on the modified helical resonator plasma source, four iterative chemical ionization source setups were designed. The μ-plici 2.2 source design served as the starting point for the development process. The first modification of this source suffered from low gas velocities, which caused tremendous long dwell and reaction times. However, its unique stacked chamber concept offered flexible design capabilities and allowed a careful adaption to the observed complex gas and reaction dynamics. Promising results were obtained, e.g., mass spectra with low background signals, showing only the expected protonated nitrogen reagent gas and residual water species in high abundance. Simultaneously, a high degree of protonation was

readily obtained for the studied analytes. Nevertheless, these various modifications on this ion source also revealed that a considerable part of the primary ions is lost through the restriction between the plasma chamber and the SSQ chamber, e.g. due to charge loss on the surfaces. With this knowledge, the second ion source was designed without any restrictions between the plasma and the reaction tube. Furthermore, the approach of maximizing the overlap of the successively formed reagent gas ions with the neutral analyte by utilizing an embedded quadrupole were pursued. Mass spectra obtained with this setup showed comparable reagent ion distributions and protonation degrees. However, charging effects occurred with this ion source setup and the ion signals were nearly unaffected by the embedded quadrupole, still leading to significant charge loss on the reaction tube surface. This was also supported by ion current measurements. Thus the embedded quadrupole was rejected in the next design and the SSQ was reinstalled.

The third ion source explicitly focused on a GC-MS application. It was the first ion source design that allowed the hyphenation with a gas chromatograph. With this ion source setup the sensitivity was further increased, resulting in low limits of detection, e.g. 209 fg on column for *o*-xylene with nitrogen as reagent gas. Preliminary results on the analytical performance showed four orders of magnitude linear dynamic range with inter-run reproducibilities of < 5 %. However, pronounced peak tailing effects and a high increase in background signals in the heated state occurred, which renders this source unsuitable for analytical GC-MS applications. Nevertheless, the reaction systems of three potential reagent gases nitrogen, methane and isobutane and their usage for final analyte ionization were studied. The nitrogen system was straight forward, as mainly N_2H^+ was observed. Isobutane formed mainly *t*-$C_4H_9^+$ and only minor other ionic hydrocarbon species. Whereas the methane system, starting with initial CH_5^+ and $C_2H_5^+$ ion, could be driven to several higher homologous ions up to $C_3H_5^+$ and $C_4H_9^+$. The selectivity of the different reaction systems were shown using *n*-decane. Since its proton affinity is much higher than the proton affinity of the main isobutane reagent ion, *n*-decane was only ionized using nitrogen and methane as reagent gases. The yields of fragmentation for each reaction system was shown using α-pinene. The different excess energies of the respective reagent ions in the protonation reaction lead to different fragmentation degrees. Due to the subsequent quantitative transformation of the primary H_3^+ into other reagent ions allowed less exothermic protonation of the analyte and reduced the ion fragmentation.

The last ion source design finally combined all the desired properties for GC-MS applications. The final setup demonstrated excellent long-term stability with constant reagent gas ion current and high temperature stability (300 °C) along maintaining the chromatographic fidelity. Even high boiling compounds in a FAMEs mixture showed chromatographic peaks of

Gaussian shape with FWHMs of 0.8 – 1 s and tailing factors of 1.05 – 1.7. Limit of detections were found to be in the low pg to upper fg range on column.
Preliminary fluid dynamic and charged particle simulation results obtained with the ion source Design 3 indicated that the current ion source geometry combined with the short segmented quadrupole as ion focusing device might need further optimization. It seemed that a considerable amount of ions is lost due to the weak focusing capabilitiy into the SSQ and through the skimmer. However, this requires further investigation.

In summary, a sensitive and selective alternative chemical ionization method based on H_3^+ as the primary charge carrying species formed in a hydrogen plasma and subsequent quantitative transformation into other reagent ions has been developed. Based on this method a chemical ionization source for GC-MS applications was investigated, which provides excellent long-term stability and low maintenance. The three studied reagent gas systems offered a selective analyte ionization and could reduce fragmentation. Beside these standard CI reagent gases, the field of suitable reagent gas systems has to be further investigated. The developed method differs considerably from the classical CI methods using electron emitting filaments and enables a whole spectrum of alternative reagent ion reaction cascades.

5.2 Outlook

Based on all the observations, results and gained knowledge within the frame of this work, an outlook on possible future improvement of the existing ion source setup is given, regardless of any limitations in the implementation (e.g., costs of additional technical equipment or development efforts).

Preliminary experiments allowed the helical resonator power supply to be operated remotely, with the circuit board decoupled from the coil and the grounded shield. This offers more flexibility for integration in future ion source designs, with regard to simpler geometry adaption, better sealing capabilities and uniform temperature control. Along this line, replacing the coil material with ceramic wire or polyimide coated wire, wounded directly around the plasma tube, should permit considerable higher temperatures to be applied even to the entire plasma region. Furthermore, the ion source housing could be extended to fully replace the grounded plasma coil shield and integrate the entire plasma and reaction region into one, metal covered and heated case. This also eliminates sealing issues of the plasma glass tube. Instead, the tube can be completely embedded in the ion source enclosure and attached with a standard

metal fitting. With the coil wire adjacently wounded around the glass tube and a wire length matched to the resonance frequency, first experiments also revealed an increased ion current by a factor of two, as compared to the plasma source used in the last ion source version.

The separation of the plasma region from the reagent gas and analyte addition should, however, be maintained to minimize plasma afterglow effects. In this work, the helical resonator plasma has shown to generate tremendous charge densities of > $1 \cdot 10^{12}$ cm^{-3}. At these high charge fluxes, ion loss due to ambipolar diffusion and electron-ion recombination will become an important factor [65, 66]. To handle this, the charge density must be controlled, preferably in favor of H_3^+ as the primarily charge carrying species. The addition of an electron attaching gas (e.g. SF_6) could increase ion signals by reducing the rate of ion-electron recombination, which is about two orders of magnitude higher than for negative and positive ions [130]. A reduction in free electrons should also reduce the positive ion loss by ambipolar diffusion. Another approach worth to be investigated in more detail, is the use of electrostatic lenses. Several experiments with electrodes in the plasma region were made, but showed no consistent results yet. Some experiments indicated a considerable impact on the analyte ion signal (increase by a factor of ~200), but these results were not reproduced with other ion source setups and the underlying mechanisms are still not clarified. However, electrostatic lenses between the plasma region and the reaction region could be used to sample only positive ions from the plasma, while preventing electrons and negative ions from entering the reaction region. In addition, an orifice could reduce back diffusion into the plasma region. Though all the apertures in this work showed substantial ion losses, they were only used for the physical separation of the individual sections, voltages could not be applied. This feature might considerably improve their transmission characteristics. In an upcoming ion source version, also an electrostatic lens in combination with a design based on a venturi inlet, similar to the SIFT technique [131], should be evaluated. This system would allow to operate the plasma region at a slightly lower pressure, which in turn promotes an electrostatic focusing of ions from the plasma effluent. The reagent gas could be directly added within the venturi inlet and the reaction region could be operated at elevated pressure.

Experiments with the slightly higher viscous and heavier deuterium permitted operational pressures of up to 10 mbar in the ion source, without overstraining the subsequent pressure stage. In contrast, hydrogen allowed 6 mbar. It was observed, that in this range the analyte signal still scaled linearly with the pressure, as a consequence of an increased total number of

collisions and partially reduced charge loss due to less diffusion to the tube surface. This leaves room for sensitivity optimization in a future development with more tailored pressure stages.

To further increase the ionization degree of the analyte, the overlap of the reagent ions with the laminar flow of neutrals should be adjusted more precisely, e.g. by actively guiding the ions in an RF multipolar field. Instead of the used quadrupole, a tripole [132] or helix tripole [133] could be used. These tripole electrode configurations provide no axial electric field to the ions. The reaction time is only determined by the flow velocity of the bulk gas in axial direction. In addition, the applied RF field deflects the ions from the center axis, which imposes a helical trajectory along the bulk gas flow direction. This off-axis deflection and helical motion leads to a maximized overlap of the reagent gas ions with the neutral analyte gas flow.

The next point concerns the ion transfer efficiency. For improved ion focusing into the next differentially pumped stage of the MS, an ion funnel is recommended. These systems efficiently capture ions with a broad mass distribution and radially focus them for efficient transfer through a conductance limiting orifice. Typically, funnels operate in a suitable pressure range of 0.1 to 30 mbar [129] and feature large ion acceptance angles. This allows to increase the reaction region tube diameter (minimizing ion wall losses). Experiments and ion trajectory simulations clearly demonstrated that the quadrupole with its small inner diameter in combination with the relatively large reaction tube inner diameter was far from ideal and left plenty of room for improvement.

All the suggestions made in this section may involve some complex changes to the existing setup and will require additional research and development. However, I am convinced that it is worth to further improve the sensitivity and the overall performance of this ion source type, since it has the potential to meet analytically demanding MS applications.

Appendix

Table 15: Ion source settings.

Settings	Ion source parameter	
#1:		
	RF supply:	
	Distance to reaction tube	125 mm
	Voltage and Current	15 V; 0.22 A
	Plasma gas flow:	
	hydrogen (7.0)	50 sccm
	Reagent gas flow:	
	nitrogen (5.0)	6 sccm

Table 16: Benzene, toluene and *o*-xylene mixtures in N_2, quantified by calibrated GC-MS.

Mixture	Benzene [ppmV]	Toluene [ppmV]	*o*-Xylene [ppmV]
#1	3.9 ± 0.6	11 ± 1	12 ± 2
#2	11 ± 2	7 ± 3	8.9 ± 0.7
#3	8.7 ± 0.8	6 ± 1	5.1 ± 0.9
#4	1.1 ± 0.1	0.90 ± 0.08	0.70 ± 0.05

Table 17: C4 – C24 even carbon saturated FAMEs mixture in Hexane (Supelco Inc., Bellefonte, PA, USA). Equal amounts of each substance.

Substance	**Nominal mass**	**Boiling point[a] [°C]**
Methyl butyrate	102	102.8
Methyl hexanoate	130	149.5
Methyl octanoate	158	192.9
Methyl decanoate	186	224.0
Methyl laurate	214	267
Methyl tetradecanoate	242	323
Methyl palmitate	270	417
Methyl octadecanoate	298	443
Methyl arachidate	326	375
Methyl docosanoate	355	393
Methyl lignocerate	383	419.5

[a] Ref. [73]

Table 18: TPS settings SSQ region.

Settings	TPS parameter	[V]
#1		
	entrance lens	3
	front segment	3
	back segment	3
	lens skimmer	2
	skimmer	1
	SSQ frequency	2.62 MHz
	SSQ amplitude	200 Vpp
#2		
	entrance lens	95.9
	front segment	81.7
	back segment	73.9
	lens skimmer	80.3
	skimmer	32.2
	SSQ frequency	2.62 MHz
	SSQ amplitude	200 Vpp
#3		
	entrance lens	9
	front segment	9.2
	back segment	2.2
	lens skimmer	4.49
	skimmer	1
	SSQ frequency	2.62 MHz
	SSQ amplitude	200 Vpp

Table 19: Gas chromatographic settings.

Settings	GC parameter	
#1:		
	Front inlet:	
	Injector	250 °C
	Split ratio	100
	Oven:	
	Temperature	40 °C
	Initial time	1 min
	Rate 1	50 °C min^{-1}
	Final temperature 1	100°C
	Final time 1	0 min
	Rate 2	100°C min^{-1}
	Final temperature 1	250 °C
	Final time 1	2 min
	Column:	
	Dimensions	30 m; 250 µm
	Carrier gas	helium
	Flow	2 sccm
	mode	constant flow
#2:		
	Front inlet:	
	Injector	250 °C
	Split ratio	100
	Oven:	
	Temperature	42 °C
	Initial time	2 min
	Rate 1	20 °C min^{-1}
	Final temperature 1	250°C
	Final time 1	0 min
	Rate 2	30°C min^{-1}
	Final temperature 1	300 °C
	Final time 1	5 min
	Column:	
	Dimensions	30 m; 250 µm
	Carrier gas	helium
	Flow	1.2 sccm
	mode	constant flow

Table 20: Fractional abundances of the major ions in the mass spectra for different reagent gas mixtures.

Ionic species	*m/z*	Fractional abundance
Reagent gas:	*Nitrogen*	
H_3O^+	19	0.35
N_2H^+	29	0.05
$[(H_2O)_2H]^+$	37	0.47
$[(H_2O)_3H]^+$	55	0.08
N_4H^+	57	0.05
Reagent gas:	*Isobutane*	
$C_4H_9^+$	57	0.38
$[C_3H_5+H_2O]^+$	59	0.05
$[C_4H_7+H_2O]^+$	73	0.16
$[C_3H_5+(H_2O)_2]^+$	77	0.10
$[(C_4H_8)_2H]^+$	113	0.06
* $C_7H_{15}O^+$	115	0.03
* $C_6H_{13}O_2^+$	117	0.13
* $C_8H_{18}O_2^+$	146	0.09
Reagent gas:	*Nitrogen/Isobutane (5.6/0.4)*	
$C_3H_3^+$	39	0.10
$C_4H_8^+$	56	0.10
$C_4H_9^+$	57	0.80
Reagent gas:	*Argon/Isobutane (3/1)*	
$C_3H_3^+$	39	0.03
$C_4H_8^+$	56	0.06
$C_4H_9^+$	57	0.92
Reagent gas:	*Methane*	
H_3O^+	19	0.03
$[(H_2O)_2H]^+$	37	0.09
$C_3H_3^+$	39	0.10
$C_3H_5^+$	41	0.19
$C_3H_7^+$	43	0.10
$C_4H_5^+$	53	0.02
$C_4H_7^+$	55	0.12
$C_4H_9^+$	57	0.22
$[C_3H_5+H_2O]^+$	59	0.02
$C_5H_9^+$	69	0.05
$C_5H_{11}^+$	71	0.01
$[C_3H_5+(H_2O)_2]^+$	77	0.03
$[C_3H_7+(H_2O)_2]^+$	79	0.02
$[C_3H_5+(H_2O)_3]^+$	95	0.01
$[C_3H_7+(H_2O)_3]^+$	97	0.01

Ionic species	***m/z***	**Fractional abundance**
Reagent gas:	*Argon/Methane (4/0.4)*	
H_3O^+	19	0.05
$C_2H_5^+$	29	0.03
$[(H_2O)_2H]^+$	37	0.04
$C_3H_3^+$	39	0.24
$C_3H_5^+$	41	0.32
$C_3H_7^+$	43	0.12
$C_4H_5^+$	53	0.01
$C_4H_7^+$	55	0.14
$C_4H_9^+$	57	0.02
$[C_3H_5+H_2O]^+$	59	0.01

List of Abbreviations

$[M]^+$	molecular ion
$[M+H]^+$	protonated molecular ion
$[M-H]^+$	deprotonated molecular ion
APCI	atmospheric pressure chemical ionization
BSQ	big segmented quadrupole
BTX	a mixture of benzene, toluene and xylene
CFD	computational fluid dynamics
CI	chemical ionization
CIMS	chemical ionization mass spectrometry
cps	counts per second
DA-APPI	dopant assisted atmospheric pressure photoionization
EI	electron ionization
eq.	equation
ESI	electrospray ionization
FAB	fast atom bombardment
FAME	fatty acid methyl ester
FWHM	full width at half maximum
GC	gas chromatograph
GC/CIMS	gas chromatography/chemical ionization mass spectrometry
GC-MS	gas chromatography/mass spectrometry
HIA	hydride ion affinity
HS	hard sphere
IE	ionization energy
LOD	limit of detection
m/z	mass-to-charge ratio
MALDI	matrix-assisted laser desorption ionization
MS	mass spectrometry
norm.	normalized
PA	proton affinity
PCB	printed circuit board
PICI	positive-ion chemical ionization

PID	proportional integral derivative
PID	photoionization detector
PTFE	polytetrafluoroethene
PVC	polyvinyl chloride
RE	recombination energy
ref.	reference
RF	radio frequency
S/N	signal-to-noise
sccm	standard cubic centimeter per minute
SSQ	short segmented quadrupole
STP	Standard Temperature and Pressure
TIC	total ion current
TOF MS	time-of-flight mass spectrometer
UV	ultraviolet
VIS	visible

List of Figures

List of Tables

References

[1] J. J. Thomson. Rays of Positive Electricity, *London Edinburgh Philos. Mag. J. Sci.* **1911**, *21*, 225–249.

[2] J. J. Thomson. *Rays of Positive Electricity and Their Application to Chemical Analyses,* 1st ed. Longmans, Green and Co., London.

[3] J. J. Thomson. *Rays of Positive Electricity and Their Application to Chemical Analyses,* 2nd ed. Longmans, Green and Co., London.

[4] A. J. Dempster. The ionization and dissociation of hydrogen molecules and the formation of H_3, *London Edinburgh Philos. Mag. J. Sci.* **1916**, *31*, 438–443.

[5] T. R. Hogness, E. G. Lunn. The Ionization of Hydrogen by Electron Impact as Interpreted by Positive Ray Analysis, *Phys. Rev.* **1925**, *26*, 44–55.

[6] A. G. Harrison. *Chemical Ionization Mass Spectrometry,* 2nd ed. Routledge, Boca Raton.

[7] V. L. Tal'roze, A. K. Ljubimova. Secondary processes in the ion source of a mass spectrometer (presented by academician N.N. Semenov 27 viii 1952)—reprinted from report of the Soviet Academy of Sciences,Volume LXXXVI, -n5 (1952), *J. Mass Spectrom.* **1998**, *33*, 502–504.

[8] D. P. Stevenson, D. O. Schissler. Rate of the Gaseous Reactions, $X^+ + YH = XH^+ + Y$, *J. Chem. Phys.* **1955**, *23*, 1353–1354.

[9] F. H. Field, J. L. Franklin, F. W. Lampe. Reactions of Gaseous Ions. I. Methane and Ethylene, *J. Am. Chem. Soc.* **1957**, *79*, 2419–2429.

[10] F. H. Field, M. S. B. Munson. Reactions of Gaseous Ions. XIV. Mass Spectrometric Studies of Methane at Pressures to 2 Torr, *J. Am. Chem. Soc.* **1965**, *87*, 3289–3294.

[11] M. S. B. Munson, F. H. Field. Reactions of Gaseous Ions. XV. Methane + 1% Ethane and Methane + 1% Propane, *J. Am. Chem. Soc.* **1965**, *87*, 3294–3299.

[12] M. S. B. Munson. Proton Affinities and the Methyl Inductive Effect, *J. Am. Chem. Soc.* **1965**, *87*, 2332–2336.

[13] M. S. B. Munson, F. H. Field. Chemical Ionization Mass Spectrometry. I. General Introduction, *J. Am. Chem. Soc.* **1966**, *88*, 2621–2630.

[14] B. Munson. Development of chemical ionization mass spectrometry, *Int. J. Mass Spectrom.* **2000**, *200*, 243–251.

[15] G. P. Arsenault, J. J. Dolhun, K. Biemann. Gas chromatography–chemical ionization mass spectrometry, *J. Chem. Soc. D*. **1970**, *0*, 1542b-1543.

[16] D. M. Schoengold, M. S. B. Munson. Combination of gas chromatography and chemical ionization mass spectrometry, *Anal. Chem.* **1970**, *42*, 1811–1813.

[17] W. J. Richter, H. Schwarz. Chemische Ionisation—ein stark Bedeutung gewinnendes massenspektrometrisches Analysenverfahren, *Angew. Chem.* **1978**, *90*, 449–469.

[18] J. H. Gross. *Mass Spectrometry*. *A Textbook,* 1st ed. Springer-Verlag, Berlin, Heidelberg.

[19] M. Vairamani, U. A. Mirza, R. Srinivas. Unusual positive ion reagents in chemical ionization mass spectrometry, *Mass Spectrom. Rev.* **1990**, *9*, 235–258.

[20] M. A. Lieberman, A. J. Lichtenberg. *Principles of Plasma Discharges and Materials Processing,* 2nd ed. John Wiley & Sons, Hoboken, New Jersey.

[21] I. Langmuir. Positive Ion Currents from the Postive Column of Mercury Arcs, *Science*. **1923**, *58*, 290–291.

[22] T. Lafleur, P. Chabert, J. P. Booth. Electron heating in capacitively coupled plasmas revisited, *Plasma Sources Sci. Technol.* **2014**, *23*, 35010.

[23] M. A. Razzak, K. Kondo, Y. Uesugi, N. Ohno, S. Takamura. Transition from electrostatic-to-electromagnetic mode in a radio-frequency Ar inductively coupled plasma in atmospheric pressure, *J. Appl. Phys.* **2004**, *95*, 427–433.

[24] W. Macalpine, R. Schildknecht. Coaxial Resonators with Helical Inner Conductor, *Proc. IRE*. **1959**, *47*, 2099–2105.

[25] J. Yang, Y. Zhang, X. Li, L. Li. An Improved Helical Resonator Design for Rubidium Atomic Frequency Standards, *IEEE Trans. Instrum. Meas.* **2010**, *59*, 1678–1685.

[26] R. J. Deri. Dielectric measurements with helical resonators, *Rev. Sci. Instrum.* **1986**, *57*, 82–86.

[27] J. Slevin, W. Stirling. Radio frequency atomic hydrogen beam source, *Rev. Sci. Instrum.* **1981**, *52*, 1780–1782.

[28] K. Niazi, A. J. Lichtenberg, M. A. Lieberman, D. L. Flamm. Operation of a helical resonator plasma source, *Plasma Sources Sci. Technol.* **1994**, *3*, 482–495.

[29] P. Bletzinger. Dual mode operation of a helical resonator discharge, *Rev. Sci. Instrum.* **1994**, *65*, 2975–2979.

[30] G. Clausnitzer et al. The polarized beam of the Erlangen-tandem accelerator, *Nucl. Instrum. Methods*. **1970**, *80*, 245–263.

[31] J. P. Toennies, W. Welz, G. Wolf. Molecular beam scattering studies of orbiting resonances and the determination of van der Waals potentials for H–Ne, Ar, Kr, and Xe and for H_2 –Ar, Kr, and Xe, *J. Chem. Phys.* **1979**, *71*, 614–642.

[32] J. E. Pollard. Radio-frequency discharge source for beams of atomic nitrogen and oxygen, *Rev. Sci. Instrum.* **1992**, *63*, 1771–1776.

[33] J. M. Cook, D. E. Ibbotson, P. D. Foo, D. L. Flamm. Etching results and comparison of low pressure electron cyclotron resonance and radio frequency discharge sources, *J. Vac. Sci. Technol., A*. **1990**, *8*, 1820–1824.

[34] J. M. Cook. Application of a low-pressure radio frequency discharge source to polysilicon gate etching, *J. Vac. Sci. Technol. B*. **1990**, *8*, 1.

[35] M. A. Lieberman, A. J. Lichtenberg, D. L. Flamm. *Theory of a Helical Resonator Plasma Source*, University of California, Berkeley, **1990**.

[36] J. Hopwood. Review of inductively coupled plasmas for plasma processing, *J. Vac. Sci. Technol., A*. **1992**, *1*, 109–116.

[37] K. Niazi, A. J. Lichtenberg, M. A. Lieberman. The dispersion and matching characteristics of the helical resonator plasma source, *IEEE Trans. Plasma Sci.* **1995**, *23*, 833–843.

[38] J. W. Denneman. Determination of electromagnetic properties of low-pressure electrodeless inductive discharges, *J. Phys. D: Appl. Phys.* **1990**, *23*, 293–298.

[39] J. Amorim. High-density plasma mode of an inductively coupled radio frequency discharge, *J. Vac. Sci. Technol. B*. **1991**, *9*, 362.

[40] K. Chandrakar. The transition from the first to the second stage of the ring discharge, *J. Appl. Phys.* **1978**, *11*, 1809–1813.

[41] O. A. Popov (Ed.). *High Density Plasma Sources,* 1st ed. Noyes Publications, New Jersey.

[42] P. Bletzinger, in *International Conference on Plasma Sciences (ICOPS)*. IEEE, **1993**, p. 163.

[43] J.-C. Park, B. Kang. Impedance model of helical resonator discharge, *IEEE Trans. Plasma Sci.* **1997**, *25*, 1398–1405.

[44] G. A. Newsome, F. L. Steinkamp, B. C. Giordano. Isobutane Made Practical as a Reagent Gas for Chemical Ionization Mass Spectrometry, *J. Am. Soc. Mass Spectrom.* **2016**, *27*, 1789–1795.

[45] R. Ekman, J. Silberring, A. Westman-Brinkmalm, A. Kraj. *Mass spectrometry: Instrumentation, Interpretation, and Applications,* 1st ed. John Wiley & Sons, Hoboken, New Jersey.

[46] B. Schneider, M. Breuer, H. Hartmann, H. Budzikiewicz. Chemical ionization with aggressive gases—a simple glow discharge source for sector field instruments, *J. Mass Spectrom.* **1989**, *24*, 216–218.

[47] D. F. Hunt, C. N. McEwen, T. M. Harvey. Positive and negative chemical ionization mass spectrometry using a Townsend discharge ion source, *Anal. Chem.* **1975**, *47*, 1730–1734.

[48] T. Oka. Interstellar H_3^+, *Proc. Natl. Acad. Sci. U. S. A.* **2006**, *103*, 12235–12242.

[49] E. P. L. Hunter, S. G. Lias. Evaluated Gas Phase Basicities and Proton Affinities of Molecules: An Update, *J. Phys. Chem. Ref. Data*. **1998**, *27*, 413–656.

[50] V. G. Anicich. Evaluated Bimolecular Ion-Molecule Gas Phase Kinetics of Positive Ions for Use in Modeling Planetary Atmospheres, Cometary Comae, and Interstellar Clouds, *J. Phys. Chem. Ref. Data*. **2009**, *22*, 1469–1569.

[51] H. Kersten, K. Kroll, K. Haberer, K. J. Brockmann, T. Benter, A. Peterson, A. Makarov. Design Study of an Atmospheric Pressure Photoionization Interface for GC-MS, *J. Am. Soc. Mass Spectrom.* **2016**, *27*, 607–614.

[52] F. H. Field. Chemical ionization mass spectrometry. IX. Temperature and pressure studies with benzyl acetate and tert-amyl acetate, *J. Am. Chem. Soc.* **1969**, *91*, 2827–2839.
[53] Python. Python Software Foundation.
[54] Microsoft Excel. Microsoft Corporation, Redmond, WA, USA.
[55] SIMION. Scientific Instrument Services Inc., Ringoes, NJ, USA.
[56] D. Manura, D. Dahl. *SIMION (R) 8.0 User Manual*. Scientific Instrument Services Inc., Ringoes, NJ, USA.
[57] L. Ding, M. Sudakov, S. Kumashiro. A simulation study of the digital ion trap mass spectrometer, *Int. J. Mass Spectrom.* **2002**, *221*, 117–138.
[58] C. M. Lock, E. W. Dyer. Simulation of ion trajectories through a high pressure radio frequency only quadrupole collision cell by SIMION 6.0, *Rapid Commun. Mass Spectrom.* **1999**, *13*, 422–431.
[59] Autodesk CFD 2019. Autodesk Inc., San Rafael, CA, USA.
[60] Autodesk Inc. Autodesk CFD 2019 User's Guide, https://knowledge.autodesk.com/support/cfd/learn-explore/caas/CloudHelp/cloudhelp/2019/ENU/SimCFD-UsersGuide/files/GUID-B3B67A19-0CF3-424B-9C77-F474453C7C1B-htm.html. **31.07.2021**.
[61] N. H. Chen, D. F. Othmer. New Generalized Equation for Gas Diffusion Coefficient, *J. Chem. Eng. Data*. **1962**, *7*, 37–41.
[62] D. G. Goodwin, R. L. Speth, H. K. Moffat, B. W. Weber. Cantera: An Object-oriented Software Toolkit for Chemical Kinetics, Thermodynamics, and Transport Processes.
[63] Schott AG. Glas 8252: Datenblatt, https://www.schott.com/d/tubing/66c1b95d-4113-4bd4-a45b-f6e663bd7f2f/1.1/schott-tubing-datasheet-glass-8252-german.pdf. **30.07.2021**.
[64] D. B. Müller. *Development of a kinetically controlled plasma induced chemical ionisation source*, Bergische Universität Wuppertal, Wuppertal, **2020**.
[65] R. N. Bhave, R. Cooper. Two- and Three-body Ion-Electron Recombination Rate Coefficients in Neon, *Aust. J. Phys.* **1995**, *48*, 503–514.
[66] M. Numano, J. R. Cussenot, M. Fabry, M. Felden. A theoretical study of the influence of ambipolar diffusion on the population distribution of excited states in a plasma, *J. Quant. Spectrosc. Radiat. Transfer*. **1975**, *15*, 1007–1016.
[67] R. C. Bolden, R. S. Hemsworth, M. J. Shaw, N. D. Twiddy. Measurements of thermal-energy ion-neutral reaction rate coefficients for rare-gas ions, *J. Phys. B: At. Mol. Opt. Phys.* **1970**, *3*, 45–60.
[68] N. G. Adams, M. J. Church, D. Smith. An experimental and theoretical investigation of the dynamics of a flowing afterglow plasma, *J. Phys. D: Appl. Phys.* **1975**, *8*, 1409–1422.

[69] R. Johnson, S. L. Guberman in *Advances In Atomic, Molecular, and Optical Physics*, *Vol. 59* (Eds.: E. Arimondo, P. R. Berman, C. C. Lin). Academic Press, Amsterdam, Boston, Heidelberg, London, New York, Oxford, Paris, San Diego, San Francisco, Singapore, Sydney, Tokio, **2010**.

[70] G. E. Streit, T. W. Newton. The effects of chemical reaction on diffusive ion loss processes in a flowing afterglow, *Int. J. Mass Spectrom. Ion Phys.* **1981**, *38*, 105–126.

[71] C. J. Howard, F. C. Fehsenfeld, M. McFarland. Negative ion-molecule reactions with atomic hydrogen in the gas phase at 296 °K, *J. Chem. Phys.* **1974**, *60*, 5086–5089.

[72] J. S. Townsend. The Theory of Ionisation of Gases by Collision, *Nature*. **1911**, *85*, 400–401.

[73] David R. Lide (Ed.). *CRC Handbook of Chemistry and Physics,* 84th ed. CRC Press, Boca Raton, London, New York, Washington, D.C.

[74] T. Lyman. The Spectrum of Hydrogen in the Region of Extremely Short Wave-Lengths, *ApJ*. **1906**, *23*, 181.

[75] B. P. Lavrov, A. S. Melnikov, M. Käning, J. Röpcke. UV continuum emission and diagnostics of hydrogen-containing nonequilibrium plasmas, *Phys. Rev. E*. **1999**, *59*, 3526–3543.

[76] A. Fridman, L. A. Kennedy. *Plasma Physics and Engineering,* 2nd ed. CRC Press, Hoboken.

[77] J. D. Cobine. *Gaseous conductors*. *Theory and engineering applications*. Dover, New York.

[78] D. Xiao (Ed.). *Gas Discharge and Gas Insulation*. Springer Verlag, Berlin, Heidelberg.

[79] Y. P. Raizer, J. E. Allen. *Gas discharge physics*. Springer, Berlin.

[80] A. Kramida, Y. Ralchenko. *NIST Atomic Spectra Database, NIST Standard Reference Database 78*. National Institute of Standards and Technology.

[81] W. Finkelnburg, R. Mecke. Die Bandensysteme im Moleklspektrum des Wasserstoffs, *Z. Physik*. **1929**, *54*, 198–214.

[82] W. Finkelnburg, R. Mecke. Die Bandensysteme im Moleklspektrum des Wasserstoffs, *Z. Physik*. **1929**, *54*, 597–631.

[83] W. Finkelnburg. Über das Moleklspektrum des Wasserstoffs mit Wellenlngenmessungen von 3667 Linien zwischen λ 4861 (H_β) und 3314 A.-E, *Z. Physik*. **1929**, *52*, 27–118.

[84] M. Bacal, A. M. Bruneteau, W. G. Graham, G. W. Hamilton, M. Nachman. Pressure and electron temperature dependence of H− density in a hydrogen plasma, *J. Appl. Phys.* **1981**, *52*, 1247–1254.

[85] A. A. Azooz, S. Cakir, D. A. Bleej. Plasma parameters in 40 MHz Argon discharge, *Results Phys.* **2015**, *5*, 85–91.

[86] K. Hiraoka, P. P. S. Saluja, P. Kebarle. Stabilities of complexes $(N_2)_nH^+$, $(CO)_nH^+$ and , $(O_2)_nH^+$ for n = 1 to 7 based on gas phase ion-equilibria measurements, *Can. J. Chem.* **1979**, *57*, 2159–2166.

[87] H. Uyama, O. Matsumoto. Synthesis of ammonia in high-frequency discharges, *Plasma Chem. Plasma Process.* **1989**, *9*, 13–24.

[88] O. Matsumoto. Plasma catalytic reaction in ammonia synthesis in the microwave discharge, *J. Phys. IV France*. **1998**, *8*, 411-420.

[89] S. Tanaka, H. Uyama, O. Matsumoto. Synergistic effects of catalysts and plasmas on the synthesis of ammonia and hydrazine, *Plasma Chem. Plasma Process.* **1994**, *14*, 491–504.

[90] H. Uyama, T. Nakamura, S. Tanaka, O. Matsumoto. Catalytic effect of iron wires on the syntheses of ammonia and hydrazine in a radio-frequency discharge, *Plasma Chem. Plasma Process.* **1993**, *13*, 117–131.

[91] E. Carrasco, I. Tanarro, V. J. Herrero, J. Cernicharo. Proton transfer chains in cold plasmas of H_2 with small amounts of N_2. The prevalence of NH_4^+, *Phys. Chem. Chem. Phys.* **2013**, *15*, 1699–1706.

[92] J. Shah, W. Wang, A. Bogaerts, M. L. Carreon. Ammonia Synthesis by Radio Frequency Plasma Catalysis: Revealing the Underlying Mechanisms, *ACS Appl. Energy Mater.* **2018**, *1*, 4824–4839.

[93] E. Carrasco, M. Jiménez-Redondo, I. Tanarro, V. J. Herrero. Neutral and ion chemistry in low pressure dc plasmas of H2/N2 mixtures: routes for the efficient production of NH3 and NH4(+), *Phys. Chem. Chem. Phys.* **2011**, *13*, 19561–19572.

[94] D. B. Milligan, P. F. Wilson, C. G. Freeman, M. Meot-Ner, M. J. McEwan. Dissociative Proton Transfer Reactions of H_3^+, N_2H^+ , and H_3O^+ with Acyclic, Cyclic, and Aromatic Hydrocarbons and Nitrogen Compounds, and Astrochemical Implications, *J. Phys. Chem. A*. **2002**, *106*, 9745–9755.

[95] Z. Zhou, M. Xie, Z. Wang, F. Qi. Determination of absolute photoionization cross-sections of aromatics and aromatic derivatives, *Rapid Commun. Mass Spectrom.* **2009**, *23*, 3994–4002.

[96] J. A. Burt, J. L. Dunn, M. J. McEwan, M. M. Sutton, A. E. Roche, H. I. Schiff. Some Ion–Molecule Reactions of H_3^+ and the Proton Affinity of H_2, *J. Chem. Phys.* **1970**, *52*, 6062–6075.

[97] R. S. Blake, P. S. Monks, A. M. Ellis. Proton-transfer reaction mass spectrometry, *Chem. Rev.* **2009**, *109*, 861–896.

[98] W. Lindinger, A. Hansel, A. Jordan. On-line monitoring of volatile organic compounds at pptv levels by means of proton-transfer-reaction mass spectrometry (PTR-MS) medical applications, food control and environmental research, *Int. J. Mass Spectrom. Ion Processes*. **1998**, *173*, 191–241.

[99] S. G. Lias, J. F. Liebman, R. D. Levin. Evaluated Gas Phase Basicities and Proton Affinities of Molecules; Heats of Formation of Protonated Molecules, *J. Phys. Chem. Ref. Data*. **1984**, *13*, 695–808.

[100] T. Solouki, J. E. Szulejko. Bimolecular and unimolecular contributions to the disparate self-chemical ionizations of alpha-pinene and camphene isomers, *J. Am. Soc. Mass Spectrom.* **2007**, *18*, 2026–2039.

[101] K. C. Hunter, A. L. L. East. Properties of C−C Bonds in n -Alkanes: Relevance to Cracking Mechanisms, *J. Phys. Chem. A*. **2002**, *106*, 1346–1356.

[102] D. J. Goebbert, P. G. Wentold. Water dimer proton affinity from the kinetic method: Dissociation energy of the water dimer, *Eur. J. Mass Spectrom.* **2004**, *10*, 837–846.

[103] T. F. Magnera, D. E. David, J. Michl. The first twenty-eight gas-phase proton hydration energies, *Chem. Phys. Lett.* **1991**, *182*, 363–370.

[104] P. Linstrom. *NIST Chemistry WebBook, NIST Standard Reference Database 69*. National Institute of Standards and Technology.

[105] B. Munson in *Encyclopedia of Analytical Chemistry.* 1st ed. (Ed.: R. A. Meyers). John Wiley & Sons, Chichester, **2006**.

[106] V. Aquilanti, G. G. Volpi. Ion—Molecule Reactions between H 3+ and Saturated Hydrocarbons, *J. Chem. Phys.* **1966**, *44*, 2307–2313.

[107] G. Smolinsky, M. J. Vasile. Ionic and neutral products of an RF discharge in methane, *Int. J. Mass Spectrom. Ion Phys.* **1975**, *16*, 137–149.

[108] A. A. Herod, A. G. Harrison. Bimolecular reactions of ions trapped in an electron space charge, *Int. J. Mass Spectrom. Ion Phys.* **1970**, *4*, 415–431.

[109] J. G. Dillard, K. Draxl, J. L. Franklin, F. H. Field, J. T. Herron, H. H. Rosenstock in *Pure and Applied Physics*, *Vol. 1* (Eds.: F. H. Field, J. L. Franklin). Elsevier, Amsterdam, **1957**.

[110] G. W. Milne, H. M. Fales, T. Axenrod. Identification of dangerous drugs by isobutane chemical ionization mass spectrometry, *Anal. Chem.* **1971**, *43*, 1815–1820.

[111] J.-M. Chao, R. Saferstein, J. Manura. Identification of heroin and its diluents by chemical ionization mass spectroscopy, *Anal. Chem.* **1974**, *46*, 296–298.

[112] S. G. Lias, P. Ausloos. Gas-Phase Photolysis and Radiolysis of Isobutane, *J. Chem. Phys.* **1968**, *48*, 392–400.

[113] G. D. Flesch, H. J. Svec. Fragmentation reactions in the mass spectrometer for C_2-C_5 alkanes, *J. Chem. Soc., Faraday Trans. 2*. **1973**, *69*, 1187–1199.

[114] V. V. Afrosimov, A. A. Basalaev, E. A. Berezovskaya, M. N. Panov, O. V. Smirnov, A. V. Tulub. Fragmentation of polyatomic ions produced by electron-loss collisions of butane and isobutane molecules with ions of kiloelectronvolt energy, *Tech. Phys.* **2006**, *51*, 1553–1562.

[115] W. Jennings, E. Mittlefehldt, P. P. Stremple. *Analytical gas chromatography,* 2nd ed. Academic Press, San Diego.

[116] S. Kromidas, H.-J. Kuss. *Chromatogramme richtig integrieren und bewerten*. *Ein Praxishandbuch für die HPLC und GC*. Wiley-VCH Verlag GmbH & Co. KGaA, Weinheim.

[117] *DIN 32645:2008-11, Chemische Analytik_- Nachweis-, Erfassungs- und Bestimmungsgrenze unter Wiederholbedingungen_- Begriffe, Verfahren, Auswertung*. Beuth Verlag GmbH, Berlin.

[118] D. R. Bates, I. Estermann (Eds.). *Advances in Atomic and Molecular Physics,* 1st ed. Academic Press, New York, London.

[119] S. J. Plimpton, S. G. Moore, A. Borner, A. K. Stagg, T. P. Koehler, J. R. Torczynski, M. A. Gallis. Direct simulation Monte Carlo on petaflop supercomputers and beyond, *Phys. Fluids*. **2019**, *31*, 086101; 1-18.

[120] SPARTA Direct Simulation Monte Carlo (DSMC) Simulator. Sandia National Laboratories.

[121] D. Gerlich in *Advances in Chemical Physics*, *Vol. 82* (Eds.: C.-Y. Ng, M. Baer). John Wiley & Sons, New York, Chichester, Brisbane, Toronto, Singapore, **1992**.

[122] F. G. Major, H. G. Dehmelt. Exchange-Collision Technique for the rf Spectroscopy of Stored Ions, *Phys. Rev.* **1968**, *170*, 91–107.

[123] R. E. March. An Introduction to Quadrupole Ion Trap Mass Spectrometry, *J. Mass Spectrom.* **1997**, *32*, 351–369.

[124] T. Wróblewski, L. Ziemczonek, E. Gazda, G. P. Karwasz. Dissociation energies of protonated water clusters, *Radiat. Phys. Chem.* **2003**, *68*, 313–318.

[125] LIU Xian-yun, XIA Li, WANG Zhen-ya, ZHANG Wei-jun. Photoionization and Photodissociation Study of α-pinene Using Synchrotron Radiation, *Acta Photonica Sin.* **2018**, *47*, 630002-1-6.

[126] M. Heinritzi, M. Simon, G. Steiner, A. C. Wagner, A. Kürten, A. Hansel, J. Curtius. Characterization of the mass-dependent transmission efficiency of a CIMS, *Atmos. Meas. Tech.* **2016**, *9*, 1449–1460.

[127] D. Gerlich. Applications of rf fields and collision dynamics in atomic mass spectrometry, *J. Anal. At. Spectrom.* **2004**, *19*, 581–590.

[128] T. Kutsch. *Ionenextraktion aus einem Wasserstoffplasma in einem helikalen Resonator. Konzipierung, Charakterisierung und Validierung einer Ionenquelle*, Bergische Universität Wuppertal, **2017**.

[129] R. T. Kelly, A. V. Tolmachev, J. S. Page, K. Tang, R. D. Smith. The ion funnel: theory, implementations, and applications, *Mass Spectrom. Rev.* **2010**, *29*, 294–312.

[130] S. T. Graul, R. R. Squires. Advances in flow reactor techniques for the study of gas-phase ion chemistry, *Mass Spectrom. Rev.* **1988**, *7*, 263–358.

[131] D. B. Milligan, D. A. Fairley, C. G. Freeman, M. J. McEwan. A flowing afterglow selected ion flow tube (FA/SIFT) comparison of SIFT injector flanges and H_3^+ + N revisited, *Int. J. Mass Spectrom.* **2000**, *202*, 351–361.

[132] M. Breitenlechner, L. Fischer, M. Hainer, M. Heinritzi, J. Curtius, A. Hansel. PTR3: An Instrument for Studying the Lifecycle of Reactive Organic Carbon in the Atmosphere, *Anal. Chem.* **2017**, *89*, 5824–5831.

[133] A. Zaytsev, M. Breitenlechner, A. R. Koss, C. Y. Lim, J. C. Rowe, J. H. Kroll, F. N. Keutsch. Using collision-induced dissociation to constrain sensitivity of ammonia chemical ionization mass spectrometry (NH_4^+ CIMS) to oxygenated volatile organic compounds, *Atmos. Meas. Tech.* **2019**, *12*, 1861–1870.